Hyperpolarized Nuclei for NMR Imaging and Spectroscopy

Methodology and model studies of lung and vascular function

Sven Månsson

Dept. of Electrical Measurements
Lund Institute of Technology
Lund University

Dept. of Experimental Research
Malmö University Hospital
Lund University

Hyperpolarized Nuclei for NMR Imaging and Spectroscopy

Methodology and model studies of lung and vascular function

Sven Månsson

Tekn. lic.

Akademisk avhandling som, för avläggande av teknologie doktorsexamen vid tekniska fakulteten vid Lunds Universitet, kommer att offentligen försvaras fredagen den 13 december 2002, kl 10.15, i hörsal E:1406, E-huset, Lunds Tekniska Högskola, Lund.

Fakultetsopponent: Professor Axel Haase, Institute of Physics, University of Würzburg, Germany.

DOKUMENTDATABLAD enl SIS 61 41 21

Organization
LUND UNIVERSITY

Department of Electrical Measurements
Lund Institute of Technology
Box 118
SE–221 00 Lund, Sweden

Author(s)
Sven Månsson

Document name
DOCTORAL DISSERTATION

Date of issue
2002–12–13

Sponsoring organization

Title and subtitle
Hyperpolarized Nuclei for NMR Imaging and Spectroscopy —
Methodology and model studies of lung and vascular function

Abstract

Based on the principle of nuclear magnetic resonance (NMR), magnetic resonance imaging (MRI) and magnetic resonance spectroscopy (MRS) are widely used methods in medical diagnostic imaging and biological research. Clinical MRI has been restricted to imaging of protons, for reasons of sensitivity. In recent years, hyperpolarization techniques have emerged that can increase the NMR signal by 5–6 orders of magnitude. The increased signal from hyperpolarized substances enables investigation of non-proton nuclei, and thus makes novel kinds of examinations possible, e.g., imaging of the lungs and respiratory airways after inhalation of hyperpolarized gas.

In this work, applications related to vascular imaging and lung function were investigated, using three hyperpolarized nuclei: ^{129}Xe, ^{13}C, and ^{3}He. In addition, practical aspects regarding the handling and utilization of hyperpolarized substances were evaluated.

The potential of angiography using echo-planar imaging (EPI) was investigated using dissolved ^{129}Xe in a phantom model. Long relaxation times were achieved in the *in vitro* experiments, allowing images of reasonable quality to be acquired within a scan time of 44 ms. Under *in vivo* conditions, severe limitations are expected, which are mainly due to short transverse relaxation times.

A novel ^{13}C substance with favorable properties for angiography was investigated using an optimized true fast imaging with steady-state precession (trueFISP) pulse sequence. Long relaxation times were obtained also under *in vivo* conditions ($T_1 \approx$ 40 s, $T_2 \approx 2$ s), which permitted the acquisition of angiograms in live rats with a signal-to-noise ratio (SNR) as high as ~500.

To investigate regional pulmonary ventilation, a technique was developed in an initial study, that was based on inhalation of ^{3}He gas. A quantitative measurement of gas replacement was calculated from the signal buildup after repeated inspirations of ^{3}He. The relative replacement of gas was close to 1 in the trachea and the major airways, and decreased to ~0.15 in the most peripheral parts of the lung. In a second study, regional ventilation was found to be increased in the inferior parts of the lung as compared with the superior parts, with the subject in supine position, whereas a uniform ventilation was measured in prone position.

From measurements of the dynamic uptake of ^{129}Xe from the alveolar gas spaces to the pulmonary blood vessels, several physiological parameters could be derived, including the thickness of the respiratory membrane and the pulmonary perfusion. The method was employed to compare healthy control animals with animals with inflammatory lung injury. A significantly increased membrane thickness (10.0 μm vs. 8.6 μm) was measured in the latter group, whereas the pulmonary perfusion remained unaltered.

By using hyperpolarized substances, novel possibilities of gaining physiological information arise, which may complement existing MRI and MRS techniques.

Key words:
Magnetic resonance; hyperpolarized; lung function; 3He; 13C; 129Xe

Classification system and/or index terms (if any):

Supplementary bibliographical information:

Language
English

ISSN and key title:
0346–6221, Report 1/02

ISBN
91–628–5434–8

Recipient's notes

Number of pages
172

Price

Security classification

Distribution by (name and address) Sven Månsson, Dept. of Experimental Research, Malmö University Hospital, SE–205 02 Malmö, Sweden.

I, the undersigned, being the copyright owner of the abstract of the above-mentioned dissertation, hereby grant to all reference sources permission to publish and disseminate the abstract of the above-mentioned dissertation.

Signature Sven Månsson Date 2002–11–19

Hyperpolarized Nuclei for NMR Imaging and Spectroscopy

Methodology and model studies of
lung and vascular function

Sven Månsson

Department of Experimental Research
Malmö University Hospital
Lund University

LUND UNIVERSITY

2002

Doctoral Dissertation

Department of Experimental Research
Malmö University Hospital

and

Department of Electrical Measurements
Lund Institute of Technology

Lund University
Sweden

Cover illustration:

^{3}He magnetic resonance image of rat lungs
(solid modeling of an image from Paper IV)

Copyright © 2002 Sven Månsson (pp. 1–66)
ISBN 91–628–5434–8
Report 1/02
ISSN 0346–6221
ISRN LUTEDX/TEEM--1074--SE
Printed in Sweden by Holmbergs AB, Malmö 2002

To Maria

To Alexander

To my parents

"The function of the expert is not to be more right than other people, but to be wrong for more sophisticated reasons."

– Dr. David Butler, 1969.

Abstract

Based on the principle of nuclear magnetic resonance (NMR), magnetic resonance imaging (MRI) and magnetic resonance spectroscopy (MRS) are widely used methods in medical diagnostic imaging and biological research. Clinical MRI has been restricted to imaging of protons for reasons of sensitivity. In recent years, hyperpolarization techniques have emerged that can increase the NMR signal by 5–6 orders of magnitude. The increased signal from hyperpolarized nuclei enables investigation of non-proton nuclei, and thus makes novel kinds of examinations possible, e.g., imaging of the lungs and respiratory airways after inhalation of hyperpolarized gas.

In this work, applications related to vascular imaging and lung function were investigated using three hyperpolarized nuclei: ^{129}Xe, ^{13}C, and ^{3}He. In addition, practical aspects regarding the handling and utilization of hyperpolarized substances were evaluated.

The potential of angiography using echo-planar imaging (EPI) was investigated using dissolved ^{129}Xe in a phantom model. Long relaxation times were achieved in the *in vitro* experiments, allowing images of reasonable quality to be acquired within a scan time of 44 ms. Under *in vivo* conditions, severe limitations are expected, which are mainly due to short transverse relaxation times.

A novel ^{13}C substance with favorable properties for angiography was investigated using an optimized true fast imaging with steady-state precession (trueFISP) pulse sequence. Long relaxation times were obtained also under *in vivo* conditions ($T_1 \approx 40$ s, $T_2 \approx 2$ s), which permitted the acquisition of angiograms in live rats with a signal-to-noise ratio (SNR) as high as ~500.

To investigate regional pulmonary ventilation, a technique was developed in an initial study that was based on inhalation of ^{3}He gas. A quantitative measurement of gas replacement was calculated from the signal buildup after repeated inspirations of ^{3}He. The relative replacement of gas was close to 1 in the trachea and the major airways, and decreased to ~0.15 in the most peripheral parts of the lung. In a second study, regional ventilation was found to be increased in the inferior parts of the lung as compared with the superior parts, with the subject in supine position, whereas a uniform ventilation was measured in prone position.

By measuring the dynamic uptake of ^{129}Xe from the alveolar gas spaces to the pulmonary blood vessels, several physiological parameters could be de-

rived, including the thickness of the respiratory membrane and pulmonary perfusion. The method was employed to compare healthy control animals with animals with inflammatory lung injury. A significantly increased membrane thickness (10.0 μm vs. 8.6 μm) was measured in the latter group, whereas the pulmonary perfusion remained unaltered.

By using hyperpolarized substances, novel possibilities of gaining physiological information arise, which may complement existing MRI and MRS techniques.

Original papers

This thesis is based on the following papers, which will be referred to in the text by their Roman numerals.

Papers I and III are reprinted with kind permission from the copyright owners: *Acta Radiologica* (Paper I) and Wiley-Liss, Inc. (Paper III).

I **Echo-planar MR Imaging of Dissolved Hyperpolarized ^{129}Xe: Potential for MR Angiography**
Månsson S, Johansson E, Svensson J, Olsson LE, Ståhlberg F, Petersson JS, Golman K
Acta Radiol 2002; 43:455–460.

II **Hyperpolarized ^{13}C MR Angiography Using TrueFISP**
Svensson J, Månsson S, Johansson E, Petersson JS, Olsson LE
Submitted to *Magn Reson Med*.

III **Quantitative Measurement of Regional Lung Ventilation Using ^{3}He MRI**
Deninger AJ, Månsson S, Petersson JS, Pettersson G, Magnusson P, Svensson J, Fridlund B, Hansson G, Erjefeldt I, Wollmer P, Golman K
Magn Reson Med 2002; 48:223–232.

IV **^{3}He MRI-based Measurement of Positional Dependence of Regional Pulmonary Ventilation in Rats**
Månsson S, Deninger AJ, Magnusson P, Pettersson G, Wollmer P, Golman K
Manuscript.

V **Characterization of Diffusing Capacity and Perfusion of the Rat Lung in a Lipopolysaccaride Disease Model Using Hyperpolarized ^{129}Xe**
Månsson S, Wolber J, Driehuys B, Wollmer P, Golman K
Submitted to *Magn Reson Med*.

Abbreviations and Symbols

2D	Two-dimensional
3D	Three-dimensional
ADC	Apparent diffusion coefficient [$cm^2\ s^{-1}$]
B_0	Main magnetic field [T]
B_1	Magnetic field created by the RF transmit coil ($B_1 \perp B_0$) [T]
CPMG	Carr-Purcell-Meiboom-Gill
CSI	Chemical shift imaging
CT	Computerized tomography
D	Diffusion constant [$cm^2\ s^{-1}$]
DNP	Dynamic nuclear polarization
EPI	Echo-planar imaging
FID	Free induction decay
FLASH	Fast low-angle shot
γ	Gyromagnetic ratio [$s^{-1}\ T^{-1}$]
LPS	Lipopolysaccaride
MRA	Magnetic resonance angiography
MRI	Magnetic resonance imaging
MRS	Magnetic resonance spectroscopy
NMR	Nuclear magnetic resonance
ω	Angular resonance frequency [s^{-1}]
P	Nuclear polarization
p_{O2}, pO_2	Partial oxygen pressure [mbar]
PSF	Point-spread function
RARE	Rapid acquisition with relaxation enhancement
RBC	Red blood cells
RF	Radio frequency
ROI	Region of interest
SD	Standard deviation
SE	Spin echo
SNR	Signal-to-noise ratio
T_1	Longitudinal (spin-lattice) relaxation time [s]
T_2	Transverse (spin-spin) relaxation time [s]
T_2^*	Transverse relaxation time including static magnetic inhomogeneities [s]
TE	Echo time
TR	Repetition time
trueFISP	True fast imaging with steady-state precession
$\dot{V}_A/\dot{Q}$	Ventilation-perfusion ratio
VI	Ventilation index

Table of Contents

1 Introduction 1
1.1 Aim 3

2 Background 4
2.1 NMR physics 4
2.1.1 The nuclear spin 4
2.1.2 Nuclear polarization 5
2.2 Hyperpolarization 6
2.2.1 The "brute-force" approach 6
2.2.2 Optical pumping methods 8
2.2.3 The DNP method 10
2.3 Properties of hyperpolarized ^{3}He, ^{129}Xe, and ^{13}C 10
2.3.1 Properties of the noble gases 10
2.3.2 Properties of potential ^{13}C imaging agents 11
2.4 Transportation and handling of hyperpolarized substances 11
2.4.1 T_1 relaxation mechanisms for hyperpolarized gases 12
2.4.2 T_1 relaxation of ^{13}C and ^{129}Xe in liquids 14
2.5 SNR considerations 15
2.5.1 Calculations of signal and noise 15
2.5.2 NMR sensitivity of various nuclei 19
2.6 Medical applications of hyperpolarized nuclei — a brief overview 19
2.6.1 Lung imaging 19
2.6.2 Hyperpolarized gases in other organs 21
2.6.3 Vascular imaging with hyperpolarized ^{13}C 23

3 Methods 24
3.1 Hyperpolarization equipment 24
3.1.1 Polarization and handling of ^{3}He and ^{129}Xe 24
3.1.2 Polarization and handling of ^{13}C 25
3.2 Mechanical ventilator for hyperpolarized gas 26
3.3 MR equipment 27
3.3.1 Pulse sequences 27
3.4 Animals 30
3.5 Investigation of dissolved ^{129}Xe for MRA applications 30
3.5.1 Properties of hyperpolarized ^{129}Xe dissolved in ethanol 30
3.5.2 Imaging of flowing ^{129}Xe and image analysis 30

3.6 Vascular imaging of a ^{13}C-based imaging agent 31
3.6.1 In vitro investigations — sequence optimization 31
3.6.2 In vivo trueFISP imaging 32
3.7 Measurements of regional pulmonary ventilation 32
3.7.1 The ventilation model and measurement procedure 32
3.7.2 Detection of vertical ventilation gradients 33
3.8 Diffusion capacity and perfusion of the rat lung 33
3.8.1 The alveolar diffusion model 34
3.8.2 Measurement procedure 35

4 Results 36
4.1 Investigation of dissolved ^{129}Xe for MRA applications (Paper I) 36
4.2 Vascular imaging of a ^{13}C-based imaging agent (Paper II) 37
4.3 Measurements of regional pulmonary ventilation (Paper III) 38
4.4 Vertical gradients of pulmonary ventilation (Paper IV) 40
4.5 Diffusion capacity and perfusion of the rat lung (Paper V) 41

5 Discussion 43
5.1 Echo-planar imaging of hyperpolarized imaging agents 43
5.2 Properties of the trueFISP sequence 44
5.3 Hyperpolarized ^{3}He ventilation imaging in animals 47
5.3.1 Aspects on T_1 relaxation 47
5.3.2 Pulse sequence considerations 49
5.4 Measurement of the uptake of ^{129}Xe in the lung 51

6 Conclusions 53

7 Acknowledgements 54

8 References 55

1 Introduction

The phenomenon of nuclear magnetic resonance (NMR) was first detected in 1945 independently by Felix Bloch and Edward Purcell (Bloch *et al.* 1946, Purcell *et al.* 1946), who in 1952 were awarded the Nobel Prize for their achievements. The principle is based on the interaction of atomic nuclei with an external magnetic field. From its first applications within physics research, NMR spectroscopy rapidly evolved into an important tool within chemistry and biochemistry. After the introduction of NMR imaging (Lauterbur 1973), NMR techniques have gained widespread diagnostic use in medicine, where they are commonly referred to as magnetic resonance imaging (MRI) and magnetic resonance spectroscopy (MRS).

Many atomic nuclei possess a magnetic moment and can hence be investigated by NMR, but the clinical use of MRI has to date been restricted to the proton (^{1}H) for reasons of sensitivity. Not only does ^{1}H have a higher sensitivity than any other nucleus (with the hypothetical exception of ^{3}H), it is also abundant in a very high concentration (about 80 M) in biological tissues.

At any given magnetic field strength, the amplitude of the NMR signal is governed by the thermal equilibrium polarization of the nuclei. The amplitude of the NMR signal, and thus the achievable signal-to-noise ratio (SNR) in the corresponding image, increases with the strength of the magnetic field in which the experiment is performed. A different means to increase the NMR signal consists of enhancing the polarization by creating an artificial, non-equilibrium distribution of the nuclei: the "hyperpolarized" state. This state can be created *in vivo* employing dynamic nuclear polarization (DNP) techniques, such as the Overhauser effect (Overhauser 1953), in combination with a suitable contrast agent. Using this approach, signal enhancements of about 60 times the thermal equilibrium value have been reported at a low magnetic field of 0.01 T (Golman *et al.* 2000). Alternatively, the hyperpolarized state of a contrast agent can be created by an external device, followed by rapid administration of the agent to the subject to be imaged. Examples of the latter approach include hyperpolarization of the noble gases ^{129}Xe (Albert *et al.* 1994) and ^{3}He (Middleton *et al.* 1995) using optical pumping, and hyperpolarization of ^{13}C, by either parahydrogen-induced hyperpolarization (Golman *et al.* 2001) or DNP hyperpolarization (Golman *et al.* 2002).

The hyperpolarization techniques increase the nuclear polarization by 5 to 6 orders of magnitude as compared with the thermal polarization, with a corresponding rise in signal. Owing to the increased polarization, MRI can be extended to nuclei other than ^{1}H, thereby permitting the visualization of, e.g., metabolic processes, which were previously inaccessible. However, the signal increase is counteracted by the much lower concentration of the hyperpolarized nuclei — 10^3 to 10^6 times lower than the ^{1}H concentration, depending on the specific application. Therefore, each application involving hyperpolarized nuclei needs to be evaluated with respect to the anticipated SNR level.

The density of protons (^{1}H) is fairly homogeneous within the body and provides little clinically useful information. The ability of conventional MRI to differentiate between various soft tissues and detect pathology is based instead on the inherently different relaxation times (T_1, T_2, and T_2^*) of different tissues. Even so, the achievable dynamic range is below 10 (Albert and Balamore 1998). With the administration of contrast agents containing paramagnetic atoms (e.g., Gd^{3+}, Mn^{2+}), the relaxation rates ($1/T_1$, $1/T_2$) will increase proportionally with the concentration of the agent. Depending on the imaging sequence used, the reduced relaxation time can result in either an increased or a decreased signal where the agent accumulates, thereby increasing the image contrast. For a detailed description of MR contrast agents, see, e.g., Merbach and Tóth 2001.

The mechanism is fundamentally different for hyperpolarized agents: the hyperpolarized nuclei generate the signal themselves rather than moderating the signal from adjacent protons. A better designation for these agents would therefore be "imaging agent" rather than "contrast agent." Consequently, hyperpolarized MRI (or MRS) has the advantage of completely lacking background signal, either because the nuclei are not naturally present in the body (noble gases) or because the natural abundance signal is negligible (^{13}C).

The signal evolution of hyperpolarized nuclei differs from that of thermally polarized nuclei: once the hyperpolarization has vanished, either by T_1 relaxation or by radiofrequency-(RF) induced depolarization, the enhanced signal cannot be regained. This calls for rapid performance of the experiments and a careful design of the imaging sequences. Sequences traditionally used in MRI may perform suboptimally — or may even be useless — and new strategies will be necessary (Zhao and Albert 1998, Durand *et al.* 2002, Wild *et al.* 2002a).

By using hyperpolarized imaging agents, MRI and MRS can be employed for the investigation of physiological parameters, which until now have been studied using other modalities, e.g., radioisotope imaging, positron emission tomography, computerized tomography (CT), or ultrasonography. Compared with the traditional modalities, MRI may provide increased spatial and temporal resolution without exposure of a subject to ionizing radiation. As examples of possible applications, quantification of physiological parameters of the lung, e.g., ventilation and perfusion, may be mentioned (Cremillieux *et al.* 1999).

1.1 Aim

The aims of this thesis were to investigate the feasibility of using hyperpolarized agents for MRI and MRS applications, to explore adequate pulse sequences and technical procedures, and to demonstrate new methods for the investigation of lung and vascular function based on hyperpolarized MRI/MRS. More specifically, the aims were:

- to investigate the possibility of rapid angiography using a hyperpolarized imaging agent and a fast echo planar imaging (EPI) sequence with respect to scan time, spatial resolution, and SNR.
- to develop and investigate an optimized pulse sequence — true fast imaging with steady-state precession (trueFISP) — for angiographic imaging using a hyperpolarized imaging agent, and to demonstrate high-SNR angiograms in live rats by applying the trueFISP sequence to imaging of hyperpolarized ^{13}C.
- to demonstrate a new strategy for a quantitative measurement of regional pulmonary ventilation based on inhalation of hyperpolarized ^{3}He gas.
- to use the ^{3}He-based method to study gravity-induced ventilation gradients in the rat lung at different postures, and to compare the results with those obtained from established techniques.
- to show how the uptake dynamics of hyperpolarized ^{129}Xe gas, as measured by an MRS-based technique, can be used to calculate the diffusing capacity and pulmonary perfusion in live rats.

2 Background

2.1 NMR physics

2.1.1 The nuclear spin

A fundamental property of the atomic nucleus is the nuclear spin, described by the spin quantum number I. Strictly speaking, the nuclear spin is a purely quantum mechanical quantity, but in terms of classical physics it may be pictured as an angular momentum — the nucleus rotates around its axis. Many atomic nuclei (mainly those with an odd mass number) have a non-zero spin quantum number and can be studied with NMR, e.g., ^{1}H, ^{3}He, and ^{13}C. Nuclei having the spin quantum number $I = 0$ "do not rotate" and cannot be studied with NMR. Most nuclei with an even mass number, e.g., ^{4}He and ^{12}C belong to this latter group.

Due to its positive charge, a rotating nucleus constitutes a microscopic ring current, giving rise to a microscopic magnetic moment $\boldsymbol{\mu}$, which can be pictured as a microscopic compass needle.[†] When placed in an external magnetic field $\boldsymbol{B}_0$, the magnetic moments orient themselves along the magnetic field; but as opposed to compass needles, only discrete orientations are allowed. The number of allowed orientations is given by $2I+1$, and each orientation is associated with a distinct quantum energy E_m:

$$E_m = -\boldsymbol{\mu} \cdot \boldsymbol{B}_0 = m\gamma\hbar B_0 \qquad [1]$$

where $m = -I, -I+1, \ldots, +I$ is the magnetic quantum number, and the constant γ is called the "gyromagnetic ratio," characteristic of each atomic nucleus. The magnetic moment $\boldsymbol{\mu}$ cannot be oriented parallel to $\boldsymbol{B}_0$, and will thus experience a torque trying to align $\boldsymbol{\mu}$ with $\boldsymbol{B}_0$. In analogy with a top rotating in the earth's gravity field, this torque will cause $\boldsymbol{\mu}$ to revolve around $\boldsymbol{B}_0$ with an angular frequency ω, denoted the Larmor frequency:

$$\omega = \gamma B_0. \qquad [2]$$

The nuclei investigated in this thesis (^{3}He, ^{13}C, and ^{129}Xe) all have the spin quantum number $I = \frac{1}{2}$, and thus two orientations are possible: namely, parallel to $\boldsymbol{B}_0$ ("spin up") and anti-parallel to $\boldsymbol{B}_0$ ("spin down"). By

[†] Bold typeface denotes vectors.

vector addition of all the magnetic moments, oriented in either the "up" or the "down" direction, a macroscopic magnetization vector parallel to $\boldsymbol{B}_0$ is obtained:

$$\boldsymbol{M} = \sum \boldsymbol{\mu}_{up} + \sum \boldsymbol{\mu}_{down} . \qquad [3]$$

However, this magnetization cannot be observed unless a rotating, transverse component is created. Such a component is created by tilting, or "flipping," $\boldsymbol{M}$ sideways, which in turn is accomplished by applying a second magnetic field, $\boldsymbol{B}_1$, perpendicular to $\boldsymbol{B}_0$, and oscillating with the Larmor frequency. The angle at which the $\boldsymbol{B}_1$ field tilts $\boldsymbol{M}$ is called the "flip angle." When a sample is placed near or inside a receiver coil in the magnetic field, the transverse magnetization component (rotating with Larmor frequency) will induce a voltage across the terminals of the receiver coil with an amplitude proportional to the magnitude of $\boldsymbol{M}$.

2.1.2 Nuclear polarization

The number of nuclei populating each energy state may be denoted N_{up} and N_{down}, respectively. If the two populations are equal, their magnetic moments cancel, resulting in zero macroscopic magnetization, and thus no NMR signal. Due to the slightly higher energy associated with the "down" direction, the number of nuclei pointing "down" will, however, be slightly fewer than the number of nuclei pointing "up" ($N_{down} < N_{up}$) under thermal equilibrium conditions (see Figure 1).

The nuclear polarization P (for nuclei with the spin quantum number $I = \frac{1}{2}$) is defined by

$$P \equiv \frac{N_{up} - N_{down}}{N_{up} + N_{down}}. \qquad [4]$$

The magnetization $\boldsymbol{M}$, and thus the NMR signal, S, will be proportional to the polarization and the total number of nuclei within the sample ($N_0 = N_{up} + N_{down}$):

$$S \propto N_0 P . \qquad [5]$$

The populations of the energy levels are, under thermal equilibrium conditions, governed by the Boltzmann distribution

$$N_m = \frac{\exp\left(E_m / k_B T\right)}{\sum_{i=-I}^{+I} \exp\left(E_i / k_B T\right)} \qquad [6]$$

where N_m is the number of nuclei in the state m, E_m is given by Eq. [1], and T is the temperature. By combining Eqs. [4] and [6], it follows that P can be expressed as

$$P = \tanh\left(\frac{\gamma \hbar B_0}{2kT}\right). \qquad [7]$$

2.2 Hyperpolarization

2.2.1 The "brute-force" approach

From Eq. [7], it follows that the thermal polarization increases with increasing magnetic field strength and decreasing temperature. A straightforward, "brute-force" approach to increase the polarization in a sample consists of subjecting it to a very strong magnetic field at a temperature close to absolute zero. The polarizations of selected nuclei at 1.5 T and 310 K, and at 20 T and 4 K (the temperature of liquid helium), are shown in Table 1.

Table 1. The polarization of selected nuclei at 1.5 T and body temperature, and at 20 T and 4 K.

Nucleus	Polarization P_1 at 1.5 T, 310 K	Polarization P_2 at 20 T, 4 K	Ratio P_2/P_1
^{1}H	$4.9 \cdot 10^{-6}$	$5.1 \cdot 10^{-3}$	1033
^{3}He	$3.8 \cdot 10^{-6}$	$3.9 \cdot 10^{-3}$	1033
^{13}C	$1.2 \cdot 10^{-6}$	$1.3 \cdot 10^{-3}$	1033
^{129}Xe	$1.4 \cdot 10^{-6}$	$1.4 \cdot 10^{-3}$	1033

The polarization, which is in the ppm range at 1.5 T and body temperature, can hence be increased by a factor of 1000 by cooling down the sample to liquid helium temperature at a field strength of 20 T. If the sample could be brought from 20 T, 4 K to 1.5 T, 310 K instantaneously and without loss of polarization, it could thus be regarded as "hyperpolarized." Figure 1

illustrates the difference between thermal equilibrium and the hyperpolarized state.

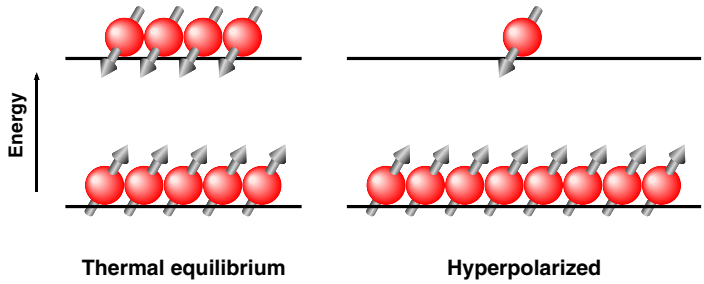

Figure 1. Pictorial description of the orientation of the nuclei at thermal equilibrium and in the hyperpolarized state. In the figure, the magnetic field (B_0) is directed vertically upwards.

Eventually, the polarization level of the hyperpolarized imaging agent returns to its thermal equilibrium value at a rate governed by the longitudinal relaxation rate T_1:

$$P(t) = \exp(-t/T_1)\left(P(0) - P_{thermal}\right) + P_{thermal}. \qquad [8]$$

Here, $P(0)$ and $P_{thermal}$ denote the initial and equilibrium polarization values, respectively. The relaxation rate T_1 depends on the chemical and physical environment of the hyperpolarized nucleus, and can range from less than one second to minutes, or even days, for some nuclei. The relaxation rate may differ significantly between *in vitro* and *in vivo* conditions. In general, ^{1}H has relaxation rates below 5 s *in vivo*, whereas the relaxation rates of the other nuclei in Table 1 can be more than one minute (see sections 2.4.1, 2.4.2, and 2.6.2).

Whenever the hyperpolarization is created outside the body, the available signal will depend on the concentration of the imaging agent after administration. Because only a limited amount of the hyperpolarized imaging agent can be administered, its anticipated concentration is 3 to 6 orders of magnitude lower than the natural ^{1}H concentration in the body. The polarization increase of about 1000 in Table 1 will thus not be sufficient to compen-

sate for the low concentration. To obtain polarization levels where the hyperpolarized signal equals, or even outperforms, the ^{1}H signal, the "brute-force" method would require temperatures in the mK range. Large-scale production of hyperpolarized noble gases (^{3}He and ^{129}Xe) has been proposed using this approach (Frossati 1998); but due to the great technical challenges and costs associated with the extremely low temperatures, this method has not yet been used for *in vivo* applications.

However, other techniques exist which sufficiently increase the polarization level of certain nuclei, including ^{3}He, ^{13}C, and ^{129}Xe.

2.2.2 Optical pumping methods

In 1960, Bouchiat *et al*. showed that angular momentum could be transferred from the electron spins of optically pumped Rb atoms (Kastler 1950) to the nuclear spins of ^{3}He by spin-exchange collisions (Bouchiat *et al.* 1960). The method could be extended to efficiently polarize ^{129}Xe as well (Grover 1978). Rb atoms are pumped via the electronic transitions $S_{1/2} - P_{1/2}$ (795.0 nm) and $S_{1/2} - P_{3/2}$ (780.2 nm). In a magnetic field, the former transition can be driven by circularly polarized laser light (795 nm) to selectively pump the ground-state Rb electrons entirely to the $+\frac{1}{2}$ (or $-\frac{1}{2}$) state. The electronic polarization of the optically pumped Rb atoms is transferred to the nuclei of the noble gas atoms via formation of loosely bound van der Waals molecules or via binary collisions (Figure 2). The former mechanism takes place at low pressure (below ~13 mbar), whereas the latter mechanism dominates above ~500 mbar, or at strong magnetic fields (Bifone 1999). Viewed macroscopically, the process creates a non-equilibrium polarization of the noble gas nuclei. A classic review of optical pumping methods has been given by Happer 1972.

Hyperpolarization of ^{3}He can also be achieved by the method of metastability exchange, first reported in 1958 (Franken and Colegrove 1958). In a low-pressure ^{3}He gas (about 1–2 mbar), $^{3}S_{1}$ metastable atoms are formed by a weak electrical discharge. By using circularly polarized light, transitions $^{3}S_{1} \rightarrow {}^{3}P_{0}$ (1083.0 nm) are induced. Due to strong hyperfine coupling, the nuclei of metastable atoms become polarized. When a polarized metastable atom collides with an unpolarized ground-state atom, a high probability for exchange of metastability exists: the metastable and the ground-state atom exchange their electron shells, while the nuclear polarization remains unaffected. Thus, the collision yields a polarized ground-state atom and an non-polarized metastable atom. The latter can once more undergo the optical

pumping process (Colegrove and Franken 1960, Colegrove *et al.* 1963, Gamblin and Carver 1965).

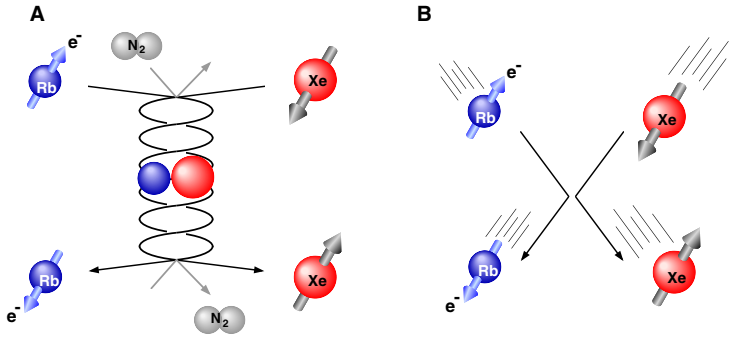

Figure 2. Spin exchange between the electronic spin of a Rb-atom and the nuclear spin of a Xe-atom via a van der Waals molecule (A) or via a binary collision (B).

Although the theory of hyperpolarizing noble gases by optical pumping was known in the early 1960s, large-scale production has only recently been possible, owing to the development of high-power lasers (Daniels *et al.* 1987, Driehuys *et al.* 1996). The spin-exchange method has the advantage of being able to polarize the gas at high pressures (~10 bar), allowing direct dispensing of the gas from the polarizer, whereas the metastable method only works at low pressure, subsequently requiring cumbersome compression of the gas. On the other hand, the metastable method is faster and can polarize a ^{3}He quantity of 2.5 l (at 1 bar) to ~50% within one hour, whereas the spin-exchange method needs polarization times of around 10 hours for polarizing a quantity of 1 l to ~40%.

The spin exchange from Rb to ^{129}Xe (at high temperatures) is more efficient than to ^{3}He. Hence, the spin-exchange technique allows faster polarization of ^{129}Xe: typically, quantities of ~0.5 l (at 1 bar) polarized to ~15% in 30 min were obtained in our laboratory. An overview of the methods for hyperpolarization of noble gases was recently published by Goodson 2002.

2.2.3 The DNP method

Dynamic nuclear polarization (DNP) (Abragam and Goldman 1978) can be used to transfer polarization from electronic spins to coupled nuclear spins. Under optimal conditions, the polarization of the nuclear spins can be increased by the ratio between the electronic and nuclear resonance frequencies. For ^{13}C nuclear spins, this ratio is ~2600. The DNP method has been used, e.g., to increase the sensitivity of ^{13}C and ^{15}N NMR spectroscopy (Wind *et al.* 1985, Hall *et al.* 1997).

As an initial step, the material containing the nuclei to be hyperpolarized is doped with a free radical. When exposed to a high magnetic field (~3 T) and low temperature (~1 K), the unpaired electrons of the free radical are highly polarized (> 90%), whereas the ^{13}C nuclei are polarized to only < 0.1%. Microwave irradiation near the electron paramagnetic resonance frequency transfers polarization from the unpaired electrons to the nuclei, whereby the nuclear polarization in the solid material can be increased to 20%–40%. By rapid melting and dissolving, the solid can be transformed into an injectable liquid, with small to negligible polarization losses (Golman *et al.* 2002).

2.3 Properties of hyperpolarized ^{3}He, ^{129}Xe, and ^{13}C

2.3.1 Properties of the noble gases

^{3}He is an inert noble gas that can be inhaled in large quantities (80% He, 20% O_2) without severe adverse effects (Brauer *et al.* 1982). The solubility of He in blood is negligible (Weathersbee and Homer 1980). Thus no systemic adverse effects of He itself have been observed. The risk of breathing pure He is hypoxia, since the body is deprived of oxygen. Due to this potential hazard during sustained noble gas breathing, careful monitoring of the individual during examination is required (Ramirez *et al.* 2000). ^{3}He is obtained from the decay of tritium (^{3}H), mainly as a by-product in the manufacturing of nuclear weapons, and the total amount on earth is only ~200 kg (Kauczor *et al.* 1998). As a matter of curiosity, large quantities of ^{3}He are available on the moon (Wittenberg *et al.* 1986), resulting from the nuclear fusion process within the sun.

^{129}Xe is an inert noble gas as well, but its solubility in biological tissues is substantial (Ostwald solubility coefficient 0.13 in blood and 1.8 in fat, (Ladefoged and Andersen 1967)). Xe is known to have euphoric and anes-

thetic effects, and has been used as an inhalant anesthetic in mixtures up to 80% (Burov *et al.* 1993, Aziz 2001). Inhaled Xe has also been used as a CT contrast agent for measuring cerebral blood flow (Gur *et al.* 1989) and lung ventilation (Tajik *et al.* 2002). Hence, the biodistribution of inhaled Xe is well known. Pharmacokinetic models for *in vivo* dynamics of hyperpolarized Xe, which in addition take into account the relaxation rate, have been presented (Peled *et al.* 1996, Martin *et al.* 1997)†. The supply of Xe is virtually unlimited (atmospheric constituent ~0.01 ppm by volume); however, the abundance of the isotope ^{129}Xe is only 26.4%. Because the gyromagnetic ratio γ of ^{129}Xe is 2.75 times lower than of ^{3}He, the SNR for Xe imaging is expected to be ~10 times lower (at equal concentration and polarization) than for He imaging (see section 2.5.1). Isotopic enrichment of ^{129}Xe to 70%–80% is possible, but discouragingly expensive. The resonance frequency of ^{129}Xe is highly dependent on the chemical environment, owing to its highly polarizable electron cloud, and can vary over a range of ~200 ppm (Miller *et al.* 1981) (see also section 2.6.2).

2.3.2 Properties of potential ^{13}C imaging agents

Virtually any small organic molecule containing ^{13}C can be hyperpolarized with the DNP technique, including many endogenous substances (Golman *et al.* 2002). The main limitations are imposed by water solubility, and toxicological and relaxation time considerations (see section 2.4.2). Suitable candidate molecules include, e.g., amino acids, citric acid, acetate, and urea. The NMR sensitivity of natural abundant ^{13}C in the body is low due to a low γ (25% of the γ_H and roughly equal to the γ_{Xe}) and low isotopic abundance (1.1%). Isotopic enrichment of ^{13}C to > 99% is possible and can be used to increase the signal of a hyperpolarized imaging agent.

2.4 Transportation and handling of hyperpolarized substances

As earlier stated, the polarization level of the imaging agent decreases towards thermal equilibrium with the time constant T_1 (Eq. [8]). It is therefore essential that the delay between the creation of the hyperpolarized state and the administration of the hyperpolarized substance is short compared with T_1.

† An interactive model for the distribution of hyperpolarized ^{129}Xe can be found at *http://ric.uthscsa.edu/staff/homepages/martin/xenon_main.html.*

2.4.1 T_1 *relaxation mechanisms for hyperpolarized gases*

Several mechanisms contribute to the relaxation rate ($1/T_1$) of hyperpolarized noble gases *in vitro* (e.g., in a transport container) and *in vivo*, including surface relaxation, oxygen-induced relaxation, gradient-induced relaxation, and dipolar relaxation.

The surface relaxation mechanisms of ^{3}He and ^{129}Xe are complex (Fitzsimmons *et al.* 1969, Driehuys *et al.* 1995), but can be outlined as

$$\frac{1}{T_{1,surface}} = \frac{1}{\eta}\frac{S}{V} \qquad [9]$$

where S/V is the surface-to-volume ratio of the gas container and η is a coefficient dependent on the surface material, the temperature, and the magnetic field strength. In iron-free glass cells, the T_1 of hyperpolarized ^{3}He can be ~100 h, and several 100 h with additional coating of cesium or rubidium (Heil *et al.* 1995, Wolf 2000, Gentile *et al.* 2001). In Pyrex cells coated with sol-gel, T_1 as long as 340 h has been measured (Hsu *et al.* 2000). In the porcine lung, the $T_{1,surface}$ for ^{3}He has been measured to be > 4 h, corresponding to a value of η of > 22 h cm^{-1} (Deninger *et al.* 1999), which is better than many uncoated and coated glass surfaces. For ^{129}Xe, a T_1 value of 3 h has been reported for gas contained in a 7.5 cm diameter quartz cell (Chann *et al.* 2002), corresponding to $\eta \approx 3.8$ h cm^{-1}.

Paramagnetic molecular oxygen is a very potent source of relaxation. The oxygen-induced relaxation rate has been empirically determined for ^{129}Xe (Jameson *et al.* 1988) and ^{3}He (Saam *et al.* 1995) according to

$$\begin{aligned} \frac{1}{T_{1,O2}} &= 0.388\frac{p_{O2}}{1.013}\frac{273}{T}\left(\frac{300}{T}\right)^{0.03} \text{ s}^{-1} \qquad (^{129}\text{Xe}) \\ \frac{1}{T_{1,O2}} &= 0.45\frac{p_{O2}}{1.013}\frac{273}{T}\left(\frac{299}{T}\right)^{0.42} \text{ s}^{-1} \qquad (^{3}\text{He}) \end{aligned} \qquad [10]$$

where T is the temperature [K] and p_{O2} is the oxygen partial pressure [bar]. Eq. [10] is valid in the temperature range from 200 K to 400 K. At room temperature (293 K), the relaxation rates can thus be expressed as

$$\frac{1}{T_{1,O2}} = \frac{p_{O2}}{\xi} \qquad [11]$$

where $\xi_{Xe} = 2.80$ bar s and $\xi_{He} = 2.40$ bar s. Accordingly, the p_{O2} in room air results in T_1 relaxation times of 13 s and 11 s, respectively.

Magnetic field gradients are another source of T_1 relaxation of hyperpolarized gases (Gamblin and Carver 1965, Schearer and Walters 1965, Cates *et al.* 1988), according to the simplified expression

$$\frac{1}{T_{1,grad}} = D\frac{\left|\nabla B_x\right|^2 + \left|\nabla B_y\right|^2}{B_0^2}. \qquad [12]$$

Here, B_x and B_y are the transverse components of the main magnetic field B_0, and ∇B_x and ∇B_y are their spatial gradients. The diffusion constant, D, of the gas is inversely proportional to the gas pressure. Eq. [12] is valid only when the magnetic field and the gas pressure are sufficiently large that

$$\frac{\omega_0 r^2}{D} >> 1 \qquad [13]$$

holds, where $\omega_0 = \gamma B_0$ is the resonance frequency and r is the radius of the gas container (Cates *et al.* 1988). The values of the diffusion constants for pure gas at atmospheric pressure have been measured at $D_{He} = 1.8$ cm^2 s^{-1} (Bock 1997) and $D_{Xe} = 0.05$ cm^2 s^{-1} (Patyal *et al.* 1997). ^{3}He is accordingly over 30 times more sensitive to inhomogeneous fields than ^{129}Xe. Although the magnetic field of the earth is extremely homogeneous and strong enough to maintain the hyperpolarized state, local magnetic fields along the transportation path, caused, e.g., by electrical installations or large ferromagnetic objects, may counteract the earth field and result in spots with virtually zero field. Problems can be avoided by designing magnetically shielded boxes providing a homogeneous magnetic field of a few mT (Grossmann 2000). However, the gradients of the magnetic fringe field near imaging or spectroscopy magnets may be very large and can reduce T_1 to a few minutes (see section 5.3).

Dipolar relaxation is caused by atomic collisions (^{3}He–^{3}He or ^{129}Xe–^{129}Xe), during which nuclear spins couple via magnetic dipole interaction, transferring their energy into a relative angular momentum. As a result, the nuclear polarization is lost (Newbury *et al.* 1993). The resulting relaxa-

tion rates at room temperature have been derived for ^{3}He (Newbury *et al.* 1993) and ^{129}Xe (Hunt and Carr 1963, Torrey 1963):

$$\frac{1}{T_{1,dipolar}} = \frac{p}{809}\ \mathrm{h}^{-1} \qquad (^{3}\mathrm{He})$$
$$\frac{1}{T_{1,dipolar}} = \frac{p}{61}\ \mathrm{h}^{-1} \qquad (^{129}\mathrm{Xe}) \qquad [14]$$

where p is the gas pressure [bar]. Dipolar relaxation in gas is thus insignificant except at very high pressures, where it imposes a fundamental limit on attainable storage times.

In addition to the mentioned relaxation mechanisms, a new relaxation mechanism for ^{129}Xe, caused by spin-rotation coupling in bound Xe–Xe van der Waals molecules, has recently been identified (Chann *et al.* 2002). The relaxation time of this mechanism is constant under most circumstances:†

$$\frac{1}{T_{1,vdW}} = 0.24\ \mathrm{h}^{-1}. \qquad [15]$$

All the relaxation mechanisms add together to a total relaxation time according to

$$\frac{1}{T_{1,total}} = \sum_{X} \frac{1}{T_{1,X}} \qquad [16]$$

where "X" denotes surface relaxation, oxygen-induced relaxation, etc.

2.4.2 T_1 relaxation of ^{13}C and ^{129}Xe in liquids

The major T_1 relaxation mechanism for ^{13}C in diamagnetic molecules is dipole-dipole interaction with protons (Harris 1983, Sanders and Hunter 1987). The relaxation rate depends on the distance between the ^{13}C and ^{1}H atoms, r, the respective gyromagnetic ratios, γ, and the correlation time τ_c (the inverse of the tumbling rate of the relevant part of the molecule), according to

† The relaxation time increases at extremely high field strengths (tens of teslas) and at very low pressures.

$$\frac{1}{T_1} \propto \gamma_C^2 \gamma_H^2 r^{-6} \tau_c . \qquad [17]$$

An effective strategy to achieve long T_1 is therefore to design a molecule with long distances between the ^{13}C atom and the neighboring atoms, and to replace hydrogen atoms near the ^{13}C with deuterium (^2H), which has a 6.5 times lower γ than ^1H. The T_1 of ^{13}C in biological molecules can be short, e.g., ~60 ms in glycogen (Zang *et al.* 1990), but by using tailored molecules, values of ~80 s *in vitro*, and of ~40 s *in vivo* have been obtained (Svensson 2002).

The T_1 of dissolved ^{129}Xe is highly dependent on the composition of the solvent. In deuterated solvents, T_1 can be long, e.g., ~5 min in deuterated urea (Rubin *et al.* 2000) and ~17 min in D_2O (Bifone *et al.* 1996). The oxygenation level of the solvent is an important parameter, since interactions with paramagnetic substances decrease the T_1 of ^{129}Xe. Several investigations have shown that T_1 is reduced drastically when ^{129}Xe comes into contact with myoglobin (Rubin *et al.* 2000) and proteins in blood (Albert *et al.* 1999, Wolber *et al.* 1999a, Albert *et al.* 2000), indicating that relaxation is caused by both non-specific and specific bindings to proteins. In particular, T_1 is shorter in deoxygenated than in oxygenated blood, partly due to the paramagnetism of deoxyhemoglobin (Tilton and Kuntz 1982), but oxygenation-dependent conformational changes of the hemoglobin molecule may also contribute (Wolber *et al.* 2000b).

Solutions of hyperpolarized ^{13}C and ^{129}Xe thus need to be prepared immediately (less than minutes) before the MR examination as opposed to gaseous ^3He and ^{129}Xe, which can be transported over long distances after the polarization to an imaging site (Wild *et al.* 2002b), owing to their much longer relaxation times *in vitro*. Under optimal conditions, the T_1 relaxation times of ^3He gas (Gentile *et al.* 2002) and frozen ^{129}Xe (Gatzke *et al.* 1993) can be as long as ~800 h and ~500 h, respectively.

2.5 SNR considerations

2.5.1 Calculations of signal and noise

The theoretical basis for estimations of SNR in magnetic resonance was presented by Hoult and co-workers in the 1970s (Hoult and Richards 1976, Hoult and Lauterbur 1979), and later by Edelstein *et al.* 1986 and, e.g., Ocali and Atalar 1998. The attainable SNR depends on the γ of the nucleus

of interest, the applied magnetic field strength B_0, and the volumes of the RF coil and the subject, but the results will differ depending on whether hyperpolarized or non-hyperpolarized substances are used.

By using the principle of reciprocity (Hoult and Richards 1976, Insko *et al.* 1998), the NMR signal voltage, S, across the terminals of the RF coil can be calculated as:

$$S \propto \gamma^2 B_0 P \hat{B}_1 V_S . \qquad [18]$$

Here, $\hat{B}_1$ is the B_1 field at unit current through the RF coil and V_S is the sample volume. The noise voltage, N, across the terminals of the RF coil originates both from the coil itself and from inductive losses in the sample (Hoult and Lauterbur 1979), and can be expressed as

$$N = \sqrt{4 k_B T b \left(R_C + R_S \right)} \qquad [19]$$

where b is the receiver bandwidth, R_C the coil resistance, and R_S is an "equivalent sample resistance" (Hoult and Lauterbur 1979, Macovski 1996), modeling the inductive sample losses. For a spherical body and a solenoidal coil, R_S is given by

$$R_S = \frac{\pi \omega^2 \mu_0^2 n^2 r_S^5}{30 \rho \left(r_C^2 + l_C^2 / 4 \right)} . \qquad [20]$$

Here, r_C, l_C, and n are the radius, the length, and the number of turns of the coil, respectively, r_S the sample radius, and ρ the resistivity of the sphere. For the solenoidal coil, the resistance (taking into account the frequency-dependent skin depth δ) and $\hat{B}_1$ are given by (Hoult and Lauterbur 1979)

$$\begin{aligned} R_C &= \frac{3 \sigma \rho_C n^2 r_C}{\delta l_C}, \qquad \delta = \sqrt{\frac{2 \rho_C}{\mu \mu_0 \omega}} \\ \hat{B}_1 &= \frac{n \mu_0}{2 \sqrt{r_C^2 + l_C^2 / 4}} \end{aligned} \qquad [21]$$

where σ is a proximity effect factor (typically 3–6 (Austin 1934)), and ρ_C and μ are the resistivity and relative permeability of the coil material. The calculation of R_C is valid as long as δ is smaller than the radius of the coil wire,

and thus breaks down at very low frequencies (very low B_0). The calculations can readily be performed for other simple geometries of the sample, e.g., a cylinder, (Macovski 1996) and other types of RF coils, e.g., a saddle coil (Hoult and Richards 1976). In the latter reference, it was found that saddle coils generated 2–3 times more noise than solenoidal coils. The solenoid was thus considered to be the "optimal" coil design for NMR.

Two situations can be distinguished: the "coil noise regime" ($R_S << R_C$) and the "sample noise regime" ($R_C << R_S$) (Edelstein *et al.* 1986). In order to analyze both regimes, the signal (Eq. [18]) is divided by the noise (Eqs. [19] –[21]) for each regime, and the resulting SNR is given per sample volume (Table 2).† It is assumed that $l_C/2 = r_C = r_S$, i.e., the coil size is always adapted to the sample size. For non-hyperpolarized substances, the expression for polarization according to Eq. [7] is used.

Table 2. SNR per sample volume for hyperpolarized and non-hyperpolarized substances. The calculations are valid for a spherical sample and a solenoidal RF coil.

Regime	SNR/V_S for non-hyperpolarized substances	SNR/V_S for hyperpolarized substances
Coil noise	$\frac{\mathrm{SNR}}{V_S} \propto \gamma^{11/4} B_0^{7/4} V_S^{-1/3}$	$\frac{\mathrm{SNR}}{V_S} \propto P\gamma^{7/4} B_0^{3/4} V_S^{-1/3}$
Sample noise	$\frac{\mathrm{SNR}}{V_S} \propto \gamma^2 B_0 V_S^{-5/6}$	$\frac{\mathrm{SNR}}{V_S} \propto P\gamma V_S^{-5/6}$

For non-hyperpolarized substances, the usual $B_0^{7/4}$ and B_0 dependencies are obtained (e.g., (Edelstein *et al.* 1986)), whereas for hyperpolarized substances, the SNR is independent of B_0 in the sample noise regime.

From the ω dependence of R_S and R_C (Eqs. [20] and [21]), it can be seen that the noise originating from the sample increases linearly with B_0, whereas the noise originating from the coil increases only with $B_0^{1/4}$. Therefore, an increase in B_0 will eventually cause a transition to the sample noise regime. The field strength $B_{0,trans}$ at which this transition occurs can be estimated by

† Noise contributions from other sources (manly the preamplifier) than the coil and the sample are neglected.

calculating the field strength at which $R_S = \beta R_C$, where β is an arbitrary constant:

$$B_{0,trans} = \kappa \frac{1}{\left(V_S/\beta\right)^{2/3}\gamma} \qquad [22]$$

with a proportionality constant $\kappa = 1.8 \cdot 10^5$ m^2 s^{-1} and V_S given in m^3. The value of κ is based on $\sigma = 5$, $\mu = 1$, $\rho_C = 1.678 \cdot 10^{-8}$ Ω m,[†] and a typical tissue resistivity of $\rho = 2$ Ω m.[‡] From Table 2, it follows that the SNR of hyperpolarized substances will increase proportionally to $B_0^{3/4}$ until the sample noise regime is reached, and thereafter remain constant. This has important implications for low-field imaging of polarized gases and liquids, which will be discussed in the next section.

When $R_S > 10R_C$, i.e., by setting $\beta = 10$ in Eq. [22], the noise contribution from the coil will be negligible as compared with the sample noise. Table 3 lists corresponding values of $B_{0,trans}$ for spheres with 40-, 20-, and 7-cm diameters, i.e., "body," "head," and "rat" dimensions, giving an estimate how far the field strength may be reduced before the SNR of hyperpolarized imaging agents begin to drop.

Table 3. Lower B_0 field limit for the regime where the SNR is independent of the field strength. The calculations are valid for a solenoidal RF coil with length and diameter equal to the sample diameter (∅).

Nucleus	$B_{0,trans}$ for a sphere with 40-cm ∅ (mT)	$B_{0,trans}$ for a sphere with 20-cm ∅ (mT)	$B_{0,trans}$ for a sphere with 7-cm ∅ (mT)
^{3}He	40	160	1000
^{13}C	120	480	4000
^{129}Xe	110	440	3600

Hyperpolarized imaging can thus be performed at very low fields (mT range) without loss of SNR. To date, several research groups have demonstrated hyperpolarized gas imaging at field strengths between 2 mT and

[†] Resistivity of copper at 20°C (*CRC Handbook of Chemistry and Physics*, 83 ed. CRC Press, Boca Raton, 2002).

[‡] Many human tissues have a resistivity of ~2-4 Ω m, e.g., muscle 1.71 Ω m, lung 1.57 Ω m; however, fat has a value of 38.5 Ω m (Faes *et al.* 1999).

230 mT, e.g., Tseng *et al.* 1998, Durand *et al.* 2002, Olsson *et al.* 2002. Contrary to conventional MRI, arguments exist that the SNR in noble-gas imaging actually *increases* at lower fields, as the weaker susceptibility gradients at lower fields cause less diffusion-induced attenuation of the signal (Wong *et al.* 1999).

2.5.2 NMR sensitivity of various nuclei

Based on the expressions given in Table 2, the relative SNR of different nuclei can be compared. In addition to the dependence on γ and polarization, P, the SNR increases linearly with the concentration, c, of the nuclei in question and the fraction, F, of the initial longitudinal magnetization, which can be utilized for signal generation. The hyperpolarized nuclei investigated in this thesis are compared with ^{1}H in Table 4.

Table 4. Relative SNR for different nuclei. The presented values assume equal imaging parameters with respect to voxel size, matrix size, and receiver bandwidth for all the nuclei.

	^{1}H [1]	^{3}He [2]	^{129}Xe [3]	^{13}C [4]
γ [s^{-1}]	$2.68 \cdot 10^{8}$	$2.04 \cdot 10^{8}$	$7.40 \cdot 10^{7}$	$6.73 \cdot 10^{7}$
P	$4.9 \cdot 10^{-6}$ (1.5 T)	0.4	0.2	0.15
c	80 M	40 mM	10 mM	200 mM
F	0.3 [1]	0.08 [5]	0.08 [5]	1 [5]
Rel. SNR	1	8	0.4	64

1) contrast enhanced MRI with repetition time (TR) = 5 ms and T_1 *= 30 ms (Maki* et al. *1996).*
2) MRI with 100% ^{3}*He in the lung.*
3) MRI with 26% ^{129}*Xe (nat. abundance) in the lung*
4) vascular MRI with ^{13}*C.*
5) see sections 5.2 and 5.3.2.

2.6 Medical applications of hyperpolarized nuclei — a brief overview

2.6.1 Lung imaging

With the advent of the hyperpolarized noble gases ^{3}He and ^{129}Xe, a natural tool was provided for imaging of the lung, which is a difficult area for ^{1}H MRI because of the low density of protons in the lung parenchyma and the strong susceptibility gradients at the gas-tissue interface (Bergin *et al.* 1991,

Bergin *et al.* 1993). In 1994, the first MR images using hyperpolarized gas were demonstrated, showing excised mouse lungs filled with ^{129}Xe (Albert *et al.* 1994). The first ^{3}He images depicting the lungs of a dead guinea pig were presented in 1995 (Middleton *et al.* 1995). These initial works were followed by the first human images using ^{3}He (Bachert *et al.* 1996, Ebert *et al.* 1996, MacFall *et al.* 1996) and ^{129}Xe (Albert *et al.* 1996, Mugler *et al.* 1997). For a review of the historical background of hyperpolarized lung imaging, see, e.g., Albert and Balamore 1998. In Figure 3, examples of lung images acquired with ^{1}H, ^{3}He, and ^{129}Xe are shown.

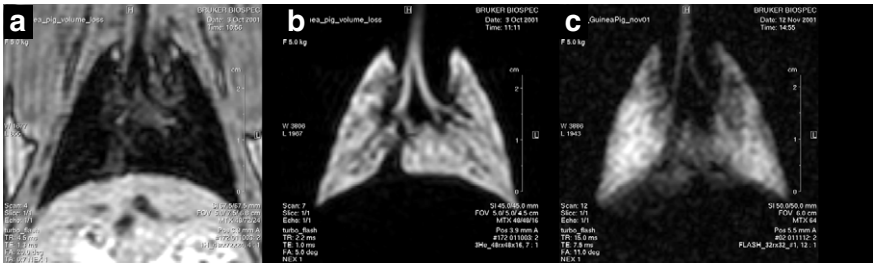

Figure 3. Lung MR images: 3D ^{1}H (a) and ^{3}He (b) images of a guinea pig, acquired at identical positions, and a 2D ^{129}Xe image of another guinea pig. (Images from our laboratory.)

The diagnostic potential of hyperpolarized gas imaging was first demonstrated in studies revealing various ventilation defects in patients, where nonventilated regions were depicted as signal voids (Kauczor *et al.* 1996). Rapid dynamic imaging has also demonstrated the potential to detect abnormal breathing patterns caused by lung disease (Johnson *et al.* 1997, Gierada *et al.* 2000, Salerno *et al.* 2001a). Owing to the large diffusion coefficient of gases (especially ^{3}He), the image intensity will decrease in regions with elevated mobility of the gas (Chen *et al.* 1999a, Yablonskiy *et al.* 2002). By measuring the apparent diffusion coefficient (ADC), it is thus possible to gain information of pathological lung structure, e.g., in emphysematous lungs (Saam *et al.* 2000). From measurements of the T_1 relaxation time, it has further been possible to calculate the regional oxygen partial pressure pO_2 in the lungs based on the depolarizing effect of O_2 (see section 2.4.1) (Deninger *et al.* 1999, Möller *et al.* 2001, Deninger *et al.* 2002). The venti-

lation-perfusion ratio ($\dot{V}_A/\dot{Q}$) is highly relevant for the diagnosis of abnormal lung function (Guyton 1986). By combining ^{3}He ventilation imaging with ^{1}H perfusion imaging, initial attempts have been made to assess the $\dot{V}_A/\dot{Q}$ parameter in rats (Cremillieux *et al.* 1999) and in humans (Lipson *et al.* 2002). It has also been suggested to assess $\dot{V}_A/\dot{Q}$ indirectly via measurements of pO_2 using ^{3}He (Eberle 2002). Reviews of the potential clinical applications of ^{3}He lung imaging can be found, among others in papers by Salerno *et al.* 2001b, Kauczor *et al.* 2002.

After the initial demonstration of human lung imaging with ^{129}Xe (Mugler *et al.* 1997), almost all work on humans has used ^{3}He, due to its higher sensitivity (see sections 2.3.1 and 2.5.1) and the current difficulties to polarize ^{129}Xe to as high levels as ^{3}He (~20% vs. ~40%, (Möller *et al.* 2002)). Efforts to quantify parameters of the lung (e.g., ADC and transverse relaxation time T_2^*) with ^{129}Xe have to date been made in animal experiments (Chen *et al.* 1999a, Chen *et al.* 1999b). Many aspects of the use of hyperpolarized gases in the lungs are discussed in a review article by Möller *et al.* 2002.

2.6.2 Hyperpolarized gases in other organs

Owing to its solubility in blood and tissues, inhaled ^{129}Xe is distributed throughout the body, and can thus be used for applications other than lung imaging (Mugler *et al.* 1997). The resonance frequency of ^{129}Xe dissolved in liquids is ~200 ppm higher than in the gas phase (Miller *et al.* 1981), and varies over a ~20 ppm range in tissues *in vivo* (Sakai *et al.* 1996, Wagshul *et al.* 1996). An example of a hyperpolarized ^{129}Xe spectrum is shown in Figure 4.

Because the resonance frequency of ^{129}Xe is sensitive to its local environment, numerous experiments involving spectroscopy or chemical shift imaging (CSI) have been presented, e.g., CSI of the chest and the brain (Swanson *et al.* 1997, Swanson *et al.* 1999), spectroscopy of tumors (Wolber *et al.* 2001), and probing of the pO_2 in blood (Wolber *et al.* 2000a). Using the large frequency shift between the gas-phase and the dissolved-phase ^{129}Xe, methods have been proposed to monitor the dynamics of ^{129}Xe when transported from the alveoli to the pulmonary blood (Ruppert *et al.* 2000a, Ruppert *et al.* 2000b), from which information about the diffusing capacity of the lung can be obtained.

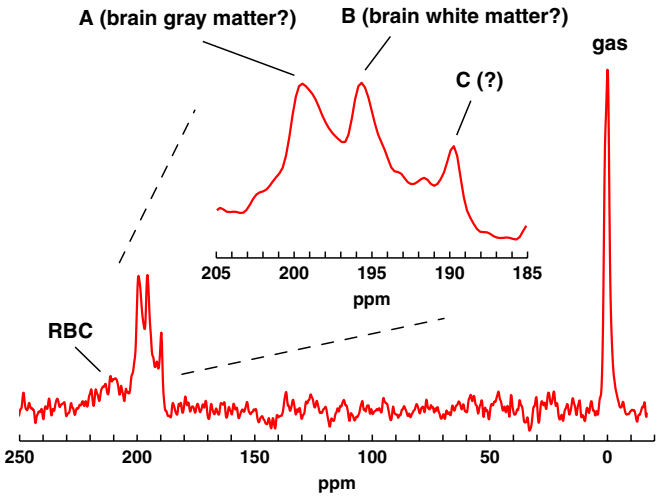

Figure 4. Spectrum of hyperpolarized ^{129}Xe in the rat brain, acquired in our laboratory. The gas peak originates from signal picked up from the oral cavity. RBC = red blood cells. The assignment of peaks **A**, **B**, and **C** is still a matter of discussion (Ruppert *et al*. 2000a, Duhamel *et al*. 2001, Kilian 2001).

Besides the aforementioned spectroscopy-based methods, attempts have been made to employ hyperpolarized noble gases in vascular applications. With respect to ^{3}He, this can only be accomplished by means of encapsulation, due to the insolubility of ^{3}He in blood and other fluids (see section 2.3.1). ^{3}He MR angiography (MRA) has been demonstrated in rats using microbubbles (Chawla *et al.* 1998, Callot *et al.* 2001) and microspheres (Chawla *et al.* 2000). When compared with microbubbles, microspheres are smaller and have a more uniform size distribution, which reduce the risk of pulmonary embolism. In both studies, ^{3}He concentrations of up to 7% per volume and T_1 of ~1 min were achieved. The use of ^{129}Xe for vascular applications is hampered by low concentrations (~1 mM when equilibrated with blood at atmospheric pressure) and the relatively short lifetime of the hyperpolarization in blood (T_1 ~5 s (Wolber *et al.* 1999a)). Using a theoretical uptake model (Martin *et al.* 1997), it has been estimated that the SNR in brain gray matter could constitute ~2% of the proton SNR under ideal conditions (50% Xe polarization, no signal loss during imaging) after inhalation of 80% Xe, and that the arterial SNR would be ~10 times higher than the brain signal. Another model has estimated that the available signal after injection of dissolved Xe would not significantly exceed the signal attainable

after gas inhalation, due to the wash-out of Xe when the bolus passes the lungs (Lavini *et al.* 2000). To improve the efficacy of injected ^{129}Xe, it has been suggested to inject "carrier agents," in which ^{129}Xe has higher solubility and longer T_1 than in blood or saline (Wolber *et al.* 1999b, Venkatesh *et al.* 2000). Using a lipid emulsion (Intralipid™, T_1 ~25 s, T_2^* ~37 ms and Ostwald solubility coefficient ~0.6, i.e., four times higher than in blood) as the carrier, angiograms of moderate quality (SNR ~28) have been demonstrated in rats (Möller *et al.* 1999). A review of the possibilities to inject hyperpolarized noble gases has been presented by e.g., Goodson 1999.

2.6.3 Vascular imaging with hyperpolarized ^{13}C

Hyperpolarized ^{13}C has only recently been available at polarization levels sufficient for MRI (Golman *et al.* 2001, Golman *et al.* 2002). At present, the polarization and T_1 *in vivo* are comparable to those of ^{129}Xe in lipid emulsion (Möller *et al.* 1999). However, ^{13}C has the potential of being superior to the noble gases in vascular applications due to its availability as a hyperpolarized liquid, with *in vivo* concentrations about 2 orders of magnitude higher than those of ^{3}He and ^{129}Xe. Further, in the work of Svensson *et al.*, the feasibility of hyperpolarized ^{13}C for MRA was investigated (Svensson 2002).

3 Methods

3.1 Hyperpolarization equipment

Three hyperpolarized nuclei were investigated in this thesis: the noble gases ^{129}Xe (Papers I and V) and ^{3}He (Papers III and IV), and a liquid ^{13}C substance (Paper II). The noble gases were polarized by means of optical pumping, whereas a different principle (DNP) was used for polarization of ^{13}C (see section 2.2).

3.1.1 Polarization and handling of ^{3}He and ^{129}Xe

^{129}Xe was polarized using a prototype commercial polarizer (IGI. 9800, Amersham Health, Durham, NC, USA). In this system, a continuously flowing gas mixture at ~5 bar pressure (1% ^{129}Xe, 10% N_2, and 89% ^{4}He) passes an optical cell containing ~1 g of Rb. When the cell is heated to 160–180 °C, small amounts of Rb evaporate and get optically pumped by a circularly polarized 795-nm laser beam illuminating the cell. Via collisions between Xe and Rb, the polarization of the Rb electrons is transferred to the Xe nuclei. After leaving the optical cell, the gas mixture passes a cold-finger trap, cooled by liquid nitrogen, where the hyperpolarized ^{129}Xe is frozen, while the other gases are ventilated out into the atmosphere. When a sufficient amount of Xe has accumulated (typically within half an hour), the cold finger is rapidly heated with water and the thawed Xe is dispensed into a reservoir.

Another prototype commercial polarizer (IGI. 9600, Amersham Health) was used for polarization of ^{3}He. Similar to the Xe polarizer, an optical cell containing Rb is heated to 160–180 °C and illuminated with a 795-nm circularly polarized laser beam, but the gas mixture (99% ^{3}He, 1% N_2) is filled into the cell once and remains inside the closed cell during the polarization procedure. The optical cell is pressurized to ~9 bar, corresponding to a hyperpolarized gas volume of ~1.1 liter at atmospheric pressure. The polarization process usually runs overnight (typically during 15–18 h).

Once sufficient polarization levels were reached, both the ^{129}Xe and the ^{3}He gas were dispensed into a plastic bag (Tedlar®, Jensen Inert, Coral Springs, FL, USA) with low surface relaxation rate and transported ~40 m from the polarizer to the MRI scanner (duration of transport less than 5 min). Using a dedicated measurement equipment (Amersham Health), the actual polarization level in the Tedlar bag was determined before and after the NMR experiments. The measurement principle is based on the detec-

tion of an NMR signal from a small surface coil in contact with the bag, and the subsequent calculation of polarization using a known factory-provided calibration constant. Typical polarization levels for ^{3}He (Papers III and IV) were 35%–40% and up to ~16% for ^{129}Xe (Papers I and V).

3.1.2 Polarization and handling of ^{13}C

^{13}C was hyperpolarized by means of the DNP method in a prototype polarizer (Amersham Health R&D, Malmö, Sweden). The water-soluble, low-toxic imaging agent (hydroxymethyl-^{13}C-cyclopropyl-methanol, see Figure 5) was doped with a paramagnetic agent and frozen in liquid nitrogen as droplets with 1–2 mm diameters. The electrons of the paramagnetic agent were polarized at a magnetic field strength of 3.35 T and a temperature of 1.3 K, and the electronic polarization was transferred to the ^{13}C nuclei by irradiation of the solid sample with 94 GHz microwaves. The ^{13}C nuclei reached a polarization level of ~20% after ~1 h of irradiation, whereat the sample was dissolved and flushed out of the magnet by a rapid injection of hot water. The polarization level in the solid state was estimated by an RF coil built into the polarizer using the same technique as above.

The solution of the hyperpolarized imaging agent was extracted into a plastic syringe and moved ~5 m to the MRI scanner within ~10 s. The polarization level in the syringe at the time of imaging was estimated to ~15%, based on the T_1 relaxation time in the syringe and the duration between the dissolving procedure and imaging.

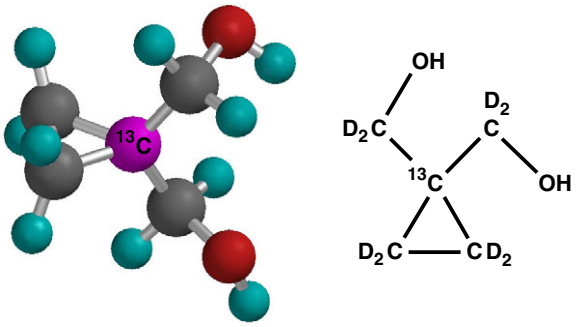

Figure 5. Molecular structure of the hyperpolarized ^{13}C imaging agent. (Courtesy of Dr. O. Axelsson, Amersham Health R&D.)

3.2 Mechanical ventilator for hyperpolarized gas

The experiments involving administration of hyperpolarized gas to the subjects (Papers III–V) used a custom-built mechanical ventilator (Amersham Health R&D). Another small animal ventilator for hyperpolarized gas has been described by Hedlund *et al.* 2000. Besides being MR compatible (no ferromagnetic parts inside or close to the imaging magnet), the ventilator has to be compatible with the hyperpolarized gas. The latter requirement dictates that the gas must not encounter any metallic parts, which may cause depolarization, nor may the gas be contaminated with oxygen from the air, which would also lead to rapid loss of polarization. A valve system, consisting of pneumatically operated membranes, was therefore constructed to control the delivery and outlet of both air and hyperpolarized gas to and from the animal (see Figure 6).

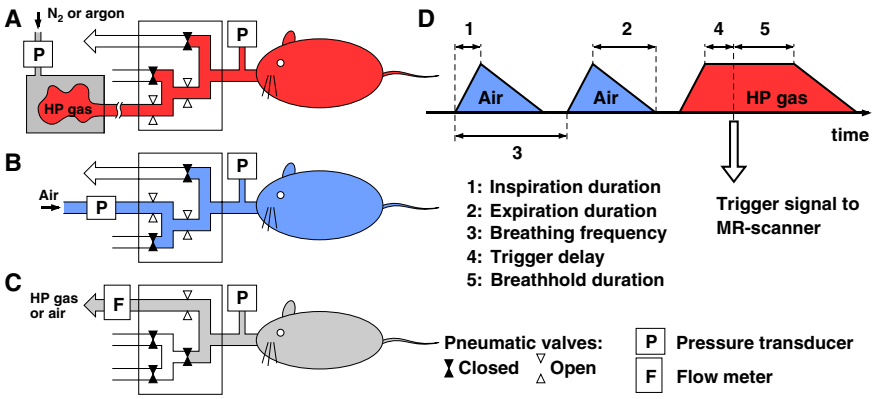

Figure 6. Function of the hyperpolarized gas ventilator during A) inspiration of $^{3}He/^{129}Xe$, B) inspiration of air, and C) expiration. The parameters denoted 1…5 were under computer control (D). (Courtesy of B. Fridlund, Amersham Health R&D.)

The hyperpolarized gas was expelled from the flexible Tedlar bag by placing the bag inside a rigid cylinder, pressurized with nitrogen or argon. During the experiments, the bag was placed as far as possible (about 1.5 m) from the MRI magnet, to reduce T_1 relaxation of the gas due to the gradients of the stray magnetic field (see section 2.4.1). The mixing of hyperpo-

larized gas with air took place as close to the animal as possible (1–2 cm outside the trachea). The volume of hyperpolarized gas delivered to the animal was controlled by adjustment of the pressure within the rigid cylinder surrounding the Tedlar bag. The computer-controlled ventilator also provided a trigger signal to the MR scanner to synchronize the gas delivery with the imaging/spectroscopy acquisitions. The reproducibility of tidal volumes, which was essential for the quantitative experiments in Papers III–V, was measured at ~2% in separate calibration experiments.

3.3 MR equipment

All MRI and MRS experiments of Papers I–V were performed on a 2.35 T animal scanner (Biospec 24/30, Bruker Biospin, Ettlingen, Germany), equipped with a gradient system with a maximum gradient strength of 200 mT m^{-1} and a gradient slew rate of 800 T m^{-1} s^{-1}. The broadband RF electronics of the scanner allow examination of virtually any nucleus, whereas RF transmit/receive coils must be manufactured individually for each nucleus. For the experiments in Papers I and V, a $^{1}H/^{129}Xe$ dual-tuned birdcage coil (Bruker Biospin) was used. The same coil could be tuned to the resonance frequency of ^{13}C, investigated in Paper II, whereas another $^{1}H/^{3}He$ dual-tuned birdcage coil (Bruker Biospin) was used for the ^{3}He experiments (Papers III and IV). The ability of the coils to also detect ^{1}H signals was used to acquire localization images, and to make necessary adjustments of B_0 field homogeneity, receiver frequency, and RF-excitation flip angles.

3.3.1 Pulse sequences

The software of the scanner allows modification of existing imaging and spectroscopy methods, as well as creation of new methods from the start. The timing and amplitudes of gradients and RF pulses are controlled by source code written in the C programming language. Via the source code, additional user interface elements can be added or modified, for instance for adapting the sequence parameters to the settings of the ventilator described in the previous section.

The EPI sequence (Mansfield 1977) employed in Paper I was available on the scanner, but was modified for operation on the ^{129}Xe frequency. The sequence was operated in the "spin-echo mode" (a refocusing 180° RF pulse was placed between the initial 90° excitation pulse and the signal readout) to

reduce the influence of B_0 inhomogeneities, which substantially can degrade the quality of EPI images.

The trueFISP sequence (Oppelt *et al.* 1986) used in Paper II, and the fast low-angle shot (FLASH) sequences (Haase *et al.* 1986) used in Papers III and IV, had to be written from the start, mainly because of the non-standard triggering behavior imposed by the animal ventilator for hyperpolarized gas (see section 3.2). The FLASH sequence offered various options for segmented image acquisition (*k*-space data of one image could optionally be acquired during several consecutive inhalations of hyperpolarized gas), as well as online calculation of the gradient *b*-value (see section 5.3.2, Eq. [28]).

The trueFISP sequence included the options of using a RF preexcitation before the image acquisition, to rapidly reach a steady state of the magnetization, and a flip-back RF pulse after the image acquisition, which returned transverse magnetization to the longitudinal direction, thereby allowing the generation of several consecutive images with arbitrary time spacing (see Figure 7). This concept has been described by Scheffler *et al.* 2001.

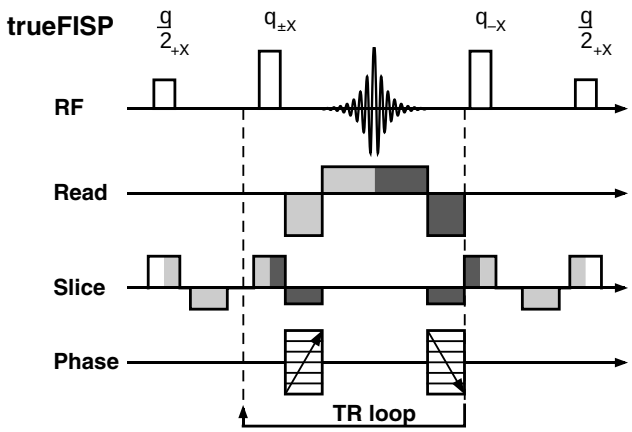

Figure 7. Sketch of the trueFISP sequence used in Paper II. The gradient areas indicated by light and dark gray, respectively, have zero integrals.

The sequence parameters of the imaging sequences used in Papers I–IV are summarized in Table 5.

Table 5. Parameters of the imaging sequences used in Papers I–IV (p = projection).

Sequence type (Paper)		TR/TE/flip angle	Matrix	Field of view (slice thickness), cm	
SE-EPI	(I)	–/32/90°	32 × 32	10 × 10	(p)
trueFISP	(II)	3.6/1.8/180°	64 × 64	7 × 7	(p)
2D FLASH	(III)	15/2/15°	64 × 64	6 × 5	(0.5)
3D FLASH	(IV)	2.1/0.9/2.5°	48 × 48 × 24	6 × 6 × 4.5	

For the measurements of the ^{129}Xe uptake in the lung (Paper V), a dedicated spectroscopy sequence was developed (Figure 8). By adjusting the duration of the rectangular excitation pulses, the ^{129}Xe signal in the tissue and the blood could be selectively destroyed with minimal effect on the alveolar gas. The uptake of ^{129}Xe could thus be measured by repetition of the experiment with different delays $\Delta(n)$ between the saturation pulse and a following readout pulse.

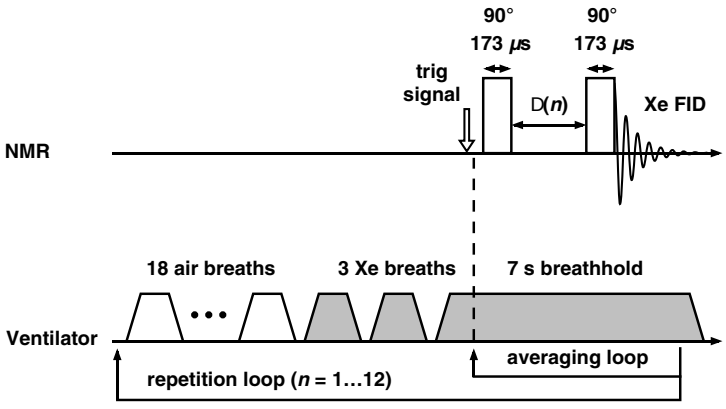

Figure 8. The spectroscopic sequence for the measurement of the ^{129}Xe uptake. The first 90° pulse destroys the Xe signal in tissue and RBC while preserving the gas signal in the alveoli. The second 90° pulse creates a free induction decay (FID) signal from Xe, which has diffused into the tissue and the RBC during the interval $\Delta(n)$ since the first pulse.

3.4 Animals

The *in vivo* experiments in Paper II, III, and IV were performed on naïve animals (Paper II: four male Wistar rats, Paper III: four male Albino guinea pigs, Paper IV: six male Sprague-Dawley rats). Both naïve (ten male Wistar rats) and diseased (ten male Wistar rats instilled with lipopolysaccaride (LPS)) animals were investigated in Paper V. The animal experiments were approved by the local ethical committee *(Malmö/Lunds djurförsöksetiska nämnd)*.

3.5 Investigation of dissolved ^{129}Xe for MRA applications

In Paper I, the potential for angiographic use of hyperpolarized imaging agents was investigated. Ethanol was chosen as a carrier agent for hyperpolarized ^{129}Xe, due to the high solubility (Ostwald solubility coefficient 1.47) of Xe in this carrier (Himm 1986).

3.5.1 Properties of hyperpolarized ^{129}Xe dissolved in ethanol

Plastic syringes were filled with 25 ml ethanol and connected to a Tedlar bag containing hyperpolarized ^{129}Xe (isotopically enriched to 75%). After filling the syringe with 35 ml of gas, the syringe was shaken intensively to dissolve the ^{129}Xe. The dissolved concentration of ^{129}Xe was measured by ^{129}Xe NMR spectra by comparing the area of the dissolved spectral peak (163 ppm) with the area of the gas peak (0 ppm).

The relaxation times of dissolved ^{129}Xe were measured by NMR spectroscopy applied to syringes without any gaseous content. The T_1 relaxation was measured by applying a train of 16 excitation pulses with a small flip angle (3°) and 12 s repetition time (TR). The T_2 relaxation was measured using a Carr-Purcell-Meiboom-Gill (CPMG) multi-echo sequence (128 echoes, inter-echo time 100 ms). The T_1 relaxation was additionally measured in syringes where the ethanol had been pre-bubbled with helium to expel any dissolved oxygen.

3.5.2 Imaging of flowing ^{129}Xe and image analysis

A flow phantom was constructed that consisted of two tubes with 6-mm diameter. With a constant, gravity driven, flow of ethanol through the phantom (mean velocity 15 cm s^{-1}), dissolved hyperpolarized ^{129}Xe was injected upstream of the phantom and rapid SE-EPI images (scan time 44 ms) were acquired repeatedly with 1.5-s intervals during the passage of the Xe bolus.

The images were evaluated with respect to artifacts and SNR, by means of region of interest (ROI) measurements.

To investigate potential losses of hyperpolarization during the dissolving procedure, a syringe filled with thermally polarized ^{129}Xe was imaged for 5 h using an SE-EPI sequence. The SNR of the thermally polarized Xe was compared with the SNR of the hyperpolarized EPI images after normalization with respect to polarization, concentration, and differences in imaging parameters.

3.6 Vascular imaging of a ^{13}C-based imaging agent

In Paper II, the trueFISP pulse sequence was optimized to match the properties of the hyperpolarized ^{13}C imaging agent, in order to obtain *in vivo* angiograms. To describe the signal evolution of a hyperpolarized substance, when imaged with the trueFISP sequence (including a preparation RF pulse, see section 3.3.1), the following expression was derived:

$$S(\theta, n) \propto \sin\frac{\theta}{2}\left(E_1^2\cos^2\frac{\theta}{2} + E_2^2\sin^2\frac{\theta}{2}\right)^{n/2} \qquad [23]$$

where $E_1 = \exp(-\mathrm{TR}/T_1)$, $E_2 = \exp(-\mathrm{TR}/T_2)$, θ is the flip angle, and n the number of applied RF excitations.

3.6.1 In vitro *investigations — sequence optimization*

In a first experiment, the image SNR was measured as a function of the flip angle. Syringes were filled with the hyperpolarized agent and imaged sequentially at different flip angles. The first and last syringe were imaged with the same flip angle, and the difference in signal intensity was used for calculation of the T_1 relaxation value, which subsequently was used to normalize all the image intensities as regards the signal decay between polarization and imaging. For comparison, the corresponding experiment was also performed using a FLASH pulse sequence.

In a second experiment, 15 rapid trueFISP images were acquired with 180° flip angle and no time gap between images. The signal decrease in these images was taken as a measure of the T_2 relaxation, since the magnetization should ideally be present entirely in the transverse plane during the experiment.

3.6.2 In vivo *trueFISP imaging*

Imaging was performed on anesthetized rats using the trueFISP sequence and a flip angle of 180°. A series of consecutive images was started immediately after the injection of the ^{13}C imaging agent in the tail vein. The images were acquired with a small (~5 ms) time separation — each image prepared by a 90° pulse and terminated by a 90° flip-back pulse. Imaging was performed in the thoracic-abdominal region in 2 animals and in the head-neck region in 2 other animals. The concentration of the imaging agent was ~200 mM in these experiments.

3.7 Measurements of regional pulmonary ventilation

Papers III and IV deal with quantitative measurements of pulmonary ventilation. In Paper III, a model was derived where the regional ventilation was calculated from the buildup of signal after increasing numbers of ^3He inspirations.

3.7.1 The ventilation model and measurement procedure

The ventilation model is based on the assumption that during each ^3He inspiration, a fraction r of a given volume element of the lung is replaced by fresh ^3He gas, and a fraction $q = 1-r$ contains gas remaining from previous inspirations. The parameter r gives the per-breath gas exchange ratio, which is used as a measure of lung ventilation.

A mathematical model was developed, which considered a) the change in pulmonary gas composition after a number of n ^3He breaths, b) the T_1 relaxation of ^3He in the lung caused by oxygen, including the washout of oxygen during ^3He breathing, and c) the T_1 relaxation of ^3He in the Tedlar bag during the duration of the experiment. The signal buildup in images acquired after n ^3He breaths can be shown to vary as function of q and n according to

$$S(n,q) \propto E^{(n-1)(N+n/2)}(1-q) \cdot \sum_{k=0}^{n-1}\left(E^{n-k-1} q^k \exp\left(-\frac{p_0 \tau}{\xi} \frac{q^{n-k}(1-q^k)}{1-q} \right) \right) \qquad [24]$$

where $E \equiv \exp(-\tau/T_{1,ext})$, τ is the duration between two breaths, N the number of air breaths separating the ^3He breathing intervals, p_0 the oxygen

partial pressure present within the lung prior to the first ^{3}He breath and ξ the proportionality factor introduced in section 2.4.1 (value at body temperature approx. 2.6 bar s (Saam *et al.* 1995)). The accuracy of measurement was assessed by adding random noise to simulated signal intensities with a known ventilation r_0, according to Eq. [24], and calculating the standard deviation of the relative error $(r - r_0)/r_0$, where r was the ventilation value obtained from the simulated noisy data.

In Paper III, a single coronal slice of the guinea-pig lung was imaged after $n = \{1, 2, \ldots, 7\}$ ^{3}He breaths using a 2D FLASH sequence. Four guinea pigs were examined. Regional ventilation maps were calculated on a pixel-by-pixel basis by fitting Eq. [24] to the intensities of the 7 images.

3.7.2 Detection of vertical ventilation gradients

In Paper IV, the method outlined in Paper III was employed to measure ventilation gradients in the lungs of rats imaged in the prone and supine positions. 3D FLASH images covering the whole lung were acquired in six naïve rats after $n = \{1, 2, \ldots 4\}$ ^{3}He breaths, and 3D ventilation maps were calculated according to the previously described procedure. To normalize for differences in absolute ventilation between the animals, the ventilation values were expressed by the "ventilation index" (VI), which is a measure of regional ventilation relative to the ventilation of the whole lung.

From the VI maps, dorsal–ventral gradients were calculated pixel by pixel by both linear and non-linear fits to the VI data along the vertical direction. Additionally, the linear correlation (R^2) between VI and vertical position was calculated. To be able to separate linear from non-linear gradients, a quadratic term was subtracted from the VI data points. On each animal, the measurement procedure was repeated in both supine and prone postures.

3.8 Diffusion capacity and perfusion of the rat lung

The global uptake of inhaled ^{129}Xe in the rat lung was measured in Paper V using a spectroscopic method. From the uptake dynamics, the average thickness of the respiratory membrane was calculated. Owing to the different resonance frequencies of ^{129}Xe in lung tissue and in RBC, the uptake could be individually assessed in these two compartments.

3.8.1 The alveolar diffusion model

The calculations were based on the diffusion of ^{129}Xe gas from the alveolar space to the pulmonary capillaries in a single-alveolus model. The model defined three compartments: the alveolar gas space, the lung tissue, and the capillary blood surrounding the alveolus (Figure 9a). Fick's laws of diffusion (Fick 1855, Dowse *et al.* 2000) were used to describe the transport of ^{129}Xe within the tissue and capillary. A simple relation was derived, from which the total thickness L $(= L_t + L_b)$ of the respiratory membrane could be calculated from the measured uptake time constant τ_1:

$$L \approx \frac{\pi}{2}\sqrt{D\tau_1}\,. \qquad [25]$$

Here, D is the diffusion constant for Xe ($\sim 1{\cdot}10^{-9}$ m^2 s^{-1} in plasma (Wolber *et al.* 2000c)). From this model, it could be shown that the amplitudes of the spectral peaks corresponding to tissue and capillary compartments, respectively, were characterized by an exponential increase during the early phase, followed by a linear increase with time (Figure 9b). It was further demonstrated that the slope and intercept parameters could be used for calculating several physiological parameters (see section 3.8.2).

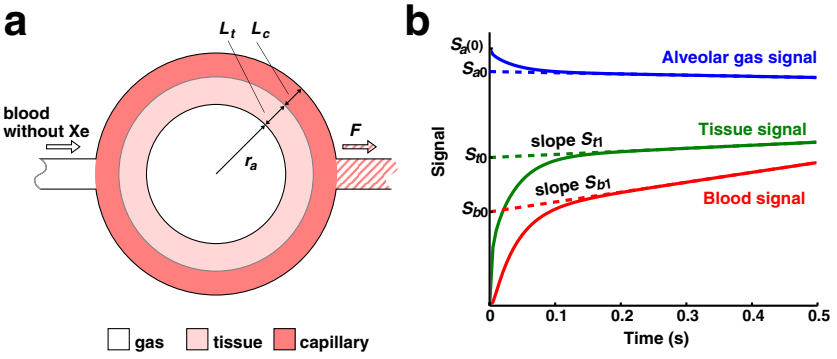

Figure 9. a) The single-alveolus diffusion model. The radius of the alveolar gas space is denoted by r_a and the thickness of the tissue and capillary compartments by L_t and L_c, respectively. F is the blood flow passing the alveolar unit. b) Simulations of gas, tissue, and blood (RBC) ^{129}Xe signals during the diffusion from alveolus to pulmonary capillaries.

3.8.2 Measurement procedure

The spectroscopic sequence shown in Figure 8 was repeated 12 times ($n = 1, \ldots, 12$) with delays $\Delta(n)$ ranging from 15 to 500 ms. Between each repetition, the animal was breathing air for 15 inspirations to wash out remaining Xe gas from the lungs. The non-localized spectra of hyperpolarized ^{129}Xe were acquired with a volume coil. Measurements were performed on one group of 10 naïve rats, and on a second group of 10 rats with acute inflammatory lung injury caused by intratracheal instillation of LPS.

The functions

$$\begin{aligned} S_g(\Delta) &= S_{0,g}\exp(-\Delta/\tau_g) + S_{1,g} \quad \text{(gas peak)} \\ S(\Delta) &= S_0\left(1-\exp(-\Delta/\tau_1)\right) + S_1\Delta \quad \text{(tissue and blood peaks)} \end{aligned} \qquad [26]$$

were fitted to the amplitudes of the gas, tissue, and blood signals as a function of the delay Δ, similar to the plot in Figure 9b. The resulting time constant τ_1 of the tissue peak was used for calculation of the total diffusion length L (Eq. [25]). The intercepts and slopes of the tissue and blood signals were used for calculation of the thickness of tissue and capillary compartments, respectively, of pulmonary perfusion, mean transit time, and relative blood volume. The alveolar radius was estimated from the initial amplitude of the gas signal and the intercept of the asymptote (see Figure 9b).

4 Results

4.1 Investigation of dissolved ^{129}Xe for MRA applications (Paper I)

The spectroscopic measurements of the dissolved ^{129}Xe signal relative to the gas signal yielded an Ostwald solubility coefficient (ratio between dissolved concentration and gas concentration) of 2.8 ± 0.3 after intense shaking of the syringes containing ^{129}Xe gas and ethanol. With only gentle shaking, the solubility was 1.6 ± 0.3, indicating that an equilibrium solution was not reached. The T_1 relaxation of dissolved ^{129}Xe was measured to 160 ± 11 s when oxygen had been expelled from the ethanol by bubbling with helium. Without helium bubbling, the measured T_1 relaxation time was reduced to 55 ± 10 s. The T_2 relaxation time was measured to 25 s.

A series of 4 images of hyperpolarized ^{129}Xe in the flow phantom, acquired with the SE-EPI sequence, is shown in Figure 10. The maximum SNR of these images was measured to 74. The SNR in the EPI image of thermally polarized xenon was 3.8. After normalization with respect to polarization and concentration, the maximum SNR of the hyperpolarized EPI images was ~75% of the thermally polarized image.

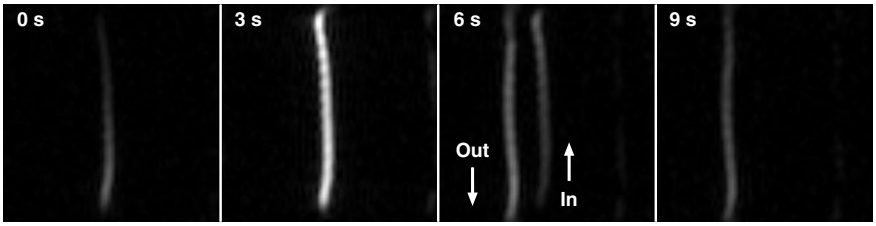

Figure 10. EPI images showing a time series of flowing HP ^{129}Xe, acquired with an inter-image delay of 1.5 s (every second image shown). The acquisition time of each image was 44 ms. The flow direction is indicated in the third image. The mean flow velocity was 15 cm/s and the polarization level was estimated at 2%.

4.2 Vascular imaging of a ^{13}C-based imaging agent (Paper II)

The T_1 relaxation time of the ^{13}C substance in water solution was estimated at 82 ± 6 s. The signal evolution in the 15 consecutive trueFISP images without phase-encoding gradients is shown in Figure 11 (data shown for the first 6 images only), demonstrating that the signal could be retained between images. From the signal decay in a corresponding series of images, but with activated phase-encoding gradients, the T_2 relaxation time was estimated at 18 s.

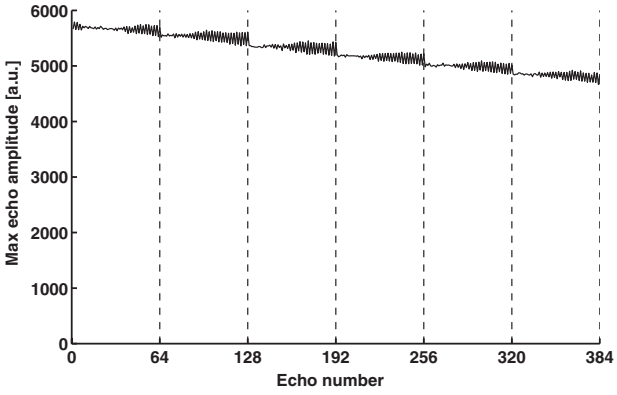

Figure 11. Maximum echo amplitudes from a series of 15 consecutive trueFISP images without phase encoding (data shown for the first 6 images only). The images were acquired with a 180° flip angle and each image was started with a 90° preparation pulse and ended with a 90° flip-back pulse. Dashed lines separate the individual images.

The investigation of the trueFISP sequence at different flip angles confirmed that the maximal signal was obtained at a flip angle of 180°. The corresponding measurement using a FLASH sequence yielded, at an optimal flip angle of ~10°, a ninefold reduction in signal as compared with the maximum signal of the trueFISP sequence.

In vivo trueFISP images are presented in Figure 12. In the image covering the abdomen and thorax (a), the *vena cava*, the heart, the lungs, the aortic arc including the branches of the carotid arteries, the abdominal aorta, and

the kidneys are visualized. The SNR measured in the *vena cava* was 240. In the image covering the head and neck (b), several vessels including the carotid arteries and jugular veins are visible. In the lower part of the image, the aortic arc is only vaguely discerned, due to the gray-level scaling of the image.

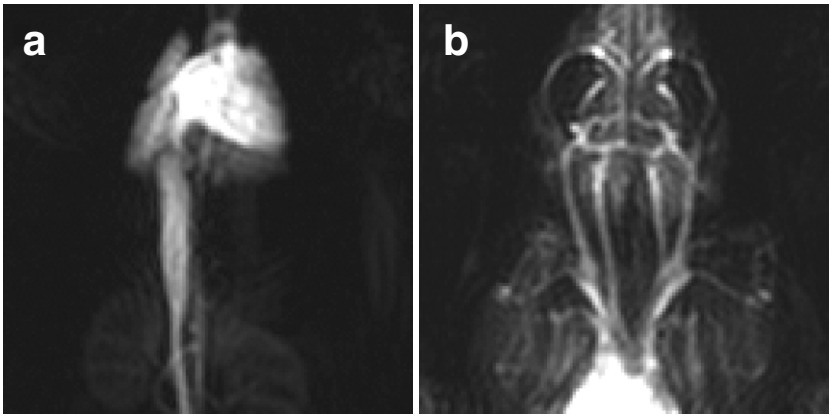

Figure 12. TrueFISP angiograms covering the thoracic-abdominal region (a) and the head-neck region (b), acquired immediately after intravenous injection of a hyperpolarized ^{13}C imaging agent (bolus volume 3 ml). Both images visualize several main vessels within the respective area.

4.3 Measurements of regional pulmonary ventilation (Paper III)

Representative signal buildup curves, obtained from images acquired after 1 to 7 breaths of ^{3}He, are depicted in Figure 13. The solid lines are obtained by a fit of Eq. [24] to measured signal intensities in single pixels in regions with low, moderate, and high ventilation. From the fit curves, ventilation values of 0.16, 0.48, and 0.77, respectively, were determined. Note that the ventilation analysis is independent of absolute image intensity values.

Typical ^{3}He spin density images acquired after n ^{3}He breaths ($n = 1, \ldots, 7$) and the corresponding ventilation map are shown in Figure 14. Ventilation values very close to 1 were found in the trachea and the major airways, indicating a complete renewal of gas per breath in these re-

gions. In central lung areas, regions close to the hilum still exhibited large ventilation values ($r \approx 0.55$–0.75). The lowest ventilation was measured in the periphery of the lungs, where values of $r \approx 0.15$–0.25 were obtained.

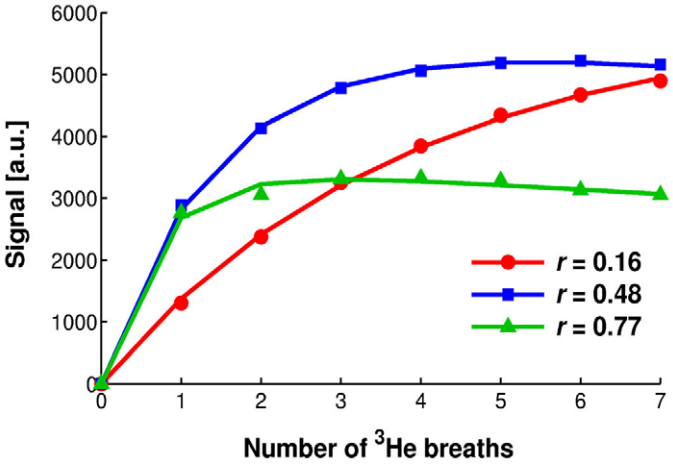

Figure 13. Signal buildup in single pixels of FLASH images of guinea-pig lungs acquired after 1 to 7 breaths of ^{3}He. The parameter r denotes the relative ventilation (fractional gas exchange per breath). The three curves represent pixels located in regions of low ($r = 0.16$), medium ($r = 0.48$), and high ($r = 0.77$) ventilation.

The accuracy of measurement was investigated by Monte Carlo simulations for varying SNR levels. Under the conditions of the experiment, the relative uncertainty of the measured ventilation was assessed to be in the range of 2%–5%. The simulations revealed that similar accuracy could be obtained also with fewer images, e.g., using only {1, 2, 5} ^{3}He breaths.

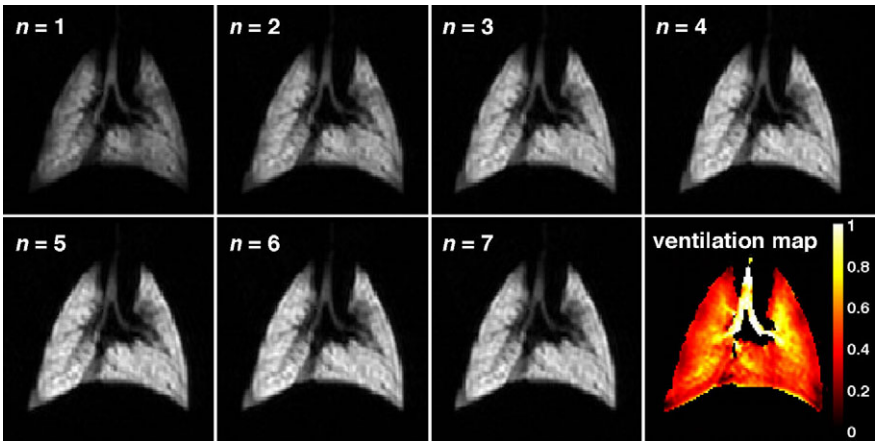

Figure 14. Signal intensities in images obtained after $n = 1, \ldots, 7$ successive ^{3}He breaths, with average SNR ranging from 50 (1 breath) to 85 (7 breaths). The ventilation map calculated from the 7 ^{3}He images is shown at the bottom right, with ventilation values in the range 0–1.

4.4 Vertical gradients of pulmonary ventilation (Paper IV)

Further refining the method outlined in Paper III, 3D ventilation maps were obtained from images of rat lungs. Again, the ventilation values ranged from ~0.2 in the peripheral regions to near 1 in the trachea and the major bronchi. The dorsal-ventral gradient of the VI was calculated for all the animals. Measured globally within the lungs, the vertical gradient of the VI was close to zero for all the animals in the prone position (mean ± SD = -0.01 ± 0.02 cm^{-1}).[†] In the supine position, a vertical gradient of about -0.11 ± 0.03 cm^{-1} was found. Measured regionally, the VI gradient in the supine position was more pronounced in the mid-base region (-0.18 ± 0.04 cm^{-1}) than in the apical region (-0.08 ± 0.03 cm^{-1}). In the supine posture, a high correlation ($R^2 > 0.6$) between VI and vertical location was observed mainly in the base and mid-base regions. In the apical lung regions, R^2 was lower (≈0.3), but increased substantially after subtraction of the quadratic fit term. In the prone posture, there was significantly lower correlation between VI and vertical location in all parts of the lung.

[†] A negative sign of the gradient means higher VI in the dependent (most inferior) lung region.

4.5 Diffusion capacity and perfusion of the rat lung (Paper V)

Spectra of hyperpolarized ^{129}Xe were obtained with gas, tissue, and blood signals clearly visible. The tissue signal SNR ranged from 20 (shortest delay Δ) to 80 (longest delay Δ). The tissue and blood signals were well separated at 198 ppm and 212 ppm, respectively, with amplitudes approximately half of the gas-signal amplitude (Figure 15a). An example of a fit of the function in Eq. [26] to the measured tissue signal amplitude is shown in Figure 15b. The uptake is characterized by a rapid increase during the first ~100 ms, described by exponential terms, followed by a linear signal growth with time. The time constant τ_1 of the exponential growth of the tissue signal was determined to 30 ± 3 ms in the control group and to 41 ± 6 ms in the LPS-treated group.

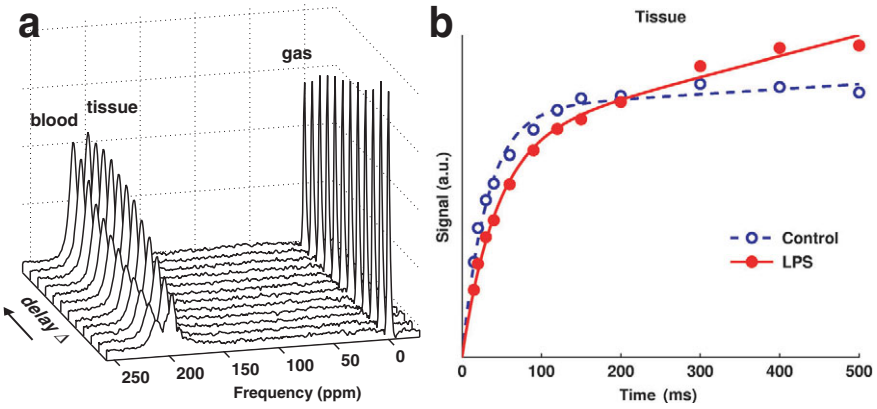

Figure 15. a) Hyperpolarized ^{129}Xe spectra from the rat lung at increasing delays Δ, during which the Xe diffuses from the alveoli to the pulmonary blood. b) ^{129}Xe uptake curves obtained after fitting the function in Eq. [26] to the tissue and blood signals. Examples are shown for one naïve animal (o) and one animal instilled with LPS (●).

The slopes and the intercepts of asymptotes fitted to the linear parts of the uptake curves (see Figure 15b) were used for calculation of total diffusion length, thickness of the tissue and the capillary compartments, pulmonary perfusion, mean transit time, relative blood volume, and alveolar radius. The results are summarized in Table 6.

*Table 6. Summary of parameters calculated from the uptake curves according to the diffusion model presented in section 3.8.1. Values are given as mean ± SD. Significant differences between the control and the LPS-treated groups are indicated in the table (***: $p \leq 0.001$, **: $p \leq 0.01$).*

Parameter	Control group	LPS-group
Total diffusion length ($L = L_t + L_c$), [μm]	8.6 ± 0.5	10.0 ± 0.8***
Tissue thickness (L_t), [μm]	4.9 ± 0.9	6.4 ± 1.2**
Blood thickness (L_c), [μm]	3.6 ± 0.8	3.6 ± 1.3
Perfusion ($\dot{Q}$), [ml s^{-1}/ml]	1.5 ± 0.3	1.3 ± 0.2
Mean transit time (M_{TT}), [s]	0.30 ± 0.11	0.29 ± 0.10
Relative blood volume (rBV)	0.43 ± 0.10	0.36 ± 0.12
Alveolar radius (r_a), [μm]	8.7 ± 3.2	8.5 ± 2.1

5 Discussion

In this thesis, three hyperpolarized nuclei (^{129}Xe, ^{13}C, and ^{3}He) have been used for development of MR methods to study the vascular system and the lung function. Below, specific error sources are pointed out and potential improvements of the techniques are suggested.

5.1 Echo-planar imaging of hyperpolarized imaging agents

The SE-EPI sequence (Paper I) is an example of a "single-shot" technique, in that the full image is acquired after a single RF excitation. Very fast scan times can be achieved with the single-shot EPI sequence, owing to its sampling scheme where the *k*-space is rapidly covered during a single readout period (Mansfield 1977). In order to achieve a successful MRA study *in vivo*, however, it is required that the T_2 of the hyperpolarized imaging agent is sufficiently long and, furthermore, that the T_2^* is at least comparable to the total duration of the data sampling period (Vlaardingerbroek and den Boer 1999), which was ≈25 ms in the investigated sequence.

The *in vitro* model using ^{129}Xe dissolved in ethanol was well suited for the experimental purpose, owing to the long T_2 of ~25 s, as measured by a CPMG sequence. The *in vivo* situation is, however, less favorable, due to the inevitable chemical exchange of ^{129}Xe atoms between different compartments (e.g., plasma and RBC). The varying resonance frequency of ^{129}Xe in different environments will thus cause an irreversible loss of phase coherence and a correspondingly short transverse relaxation time (Woessner 1996). Hence, in pilot *in vivo* experiments with injections of hyperpolarized ^{129}Xe dissolved in ethanol, the EPI-sequence failed to detect any signal. When ^{129}Xe is directly dissolved in blood and tissue, T_2 relaxation times of 2–7 ms have been reported (Wilson *et al.* 1999). Prolonged transverse relaxation time (T_2^* ~40 ms, as measured by the spectral linewidth) has, however, been demonstrated using suitable carrier agents (Möller *et al.* 1999), but it is nevertheless doubtful whether the EPI sequence can be successfully applied to hyperpolarized ^{129}Xe for vascular applications.

Owing to its by far longer transverse relaxation time *in vivo*, the imaging agent used in Paper II has the potential of being successfully used in combination with EPI sequences. This combination has been attempted in preliminary trials, where the *in vivo* experiment of Paper II was repeated, however employing the EPI sequence of Paper I. Some of the resulting images

are presented in Figure 16, which can be compared with the trueFISP images in Figure 12a.

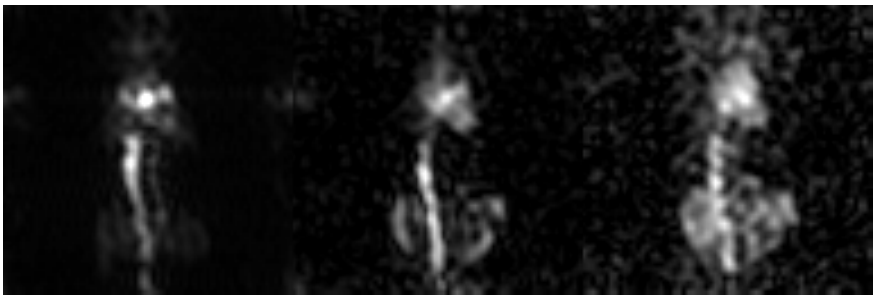

Figure 16. A series of consecutive images of a live rat using the EPI-sequence described in Paper I and the hyperpolarized ^{13}C-based imaging agent in Paper II. The *vena cava*, the heart, the aorta, and the kidneys are discernable despite the coarse resolution.

5.2 Properties of the trueFISP sequence

The trueFISP sequence (Paper II) can reuse transverse magnetization remaining from previous TR intervals and thereby increase the SNR, provided that the relaxation times are sufficiently long (Oppelt *et al.* 1986). The trueFISP technique is known to be very sensitive to field inhomogeneities (Scheffler 1999), and to achieve a homogeneous signal intensity in trueFISP images, the resonant offset, Δf, across the object must fulfil the relation

$$\Delta f \leq \frac{3\pi}{4\mathrm{TR}} \qquad [27]$$

(Patz 1988), i.e., a long TR requires a better homogeneity. Due to this relation, efforts were made to reduce the TR and TE of the trueFISP sequence during the experiments in Paper II. A reduction of the TR from 8 ms to below 4 ms resulted in a dramatic improvement of the image quality. Owing to the ≈4 times lower γ of ^{13}C as compared with ^{1}H, the resonant-offset problem is accordingly reduced, however, the lower γ is also a disadvantage

due to the increased demand on the gradient strength to obtain a given spatial resolution.

A calculation of the point-spread function† (PSF) for the trueFISP sequence at a resonant offset of 5 ppm (Figure 17) shows pronounced ghosting artifacts at a flip angle, θ, of 90°. With increasing flip angle, these artifacts decrease and are virtually invisible at a flip angle of 180°. The simulation was made under the assumption that the T_1 and T_2 relaxation times were long as compared with the duration of the imaging sequence, i.e., no regrowth of longitudinal magnetization took place, thus the calculation corresponded to imaging of hyperpolarized spins.

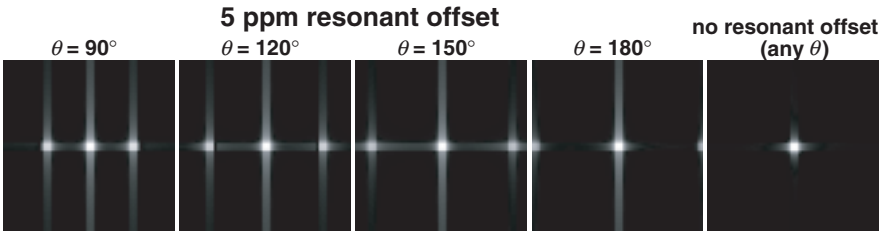

Figure 17. PSF of the trueFISP sequence at various flip angles θ, for 5 ppm off-resonance spins. The images display ln(1+|PSF|) for improved visualization of low intensities. To improve the visualization of the PSFs, the calculation was made for 3×3 pixels instead of a single pixel. The PSFs were calculated by means of a spin vector simulation of $5 \cdot 10^5$ spin isochromats. The same imaging parameters as in Paper II were used. (Phase-encoding direction: horizontal).

In Paper II, the signal from 15 consecutive ^{13}C images were collected without phase-encoding gradients. The resulting signal (Figure 11) showed a slow decay, but also a weak oscillation. The sensitivity of the trueFISP sequence to resonant offset could tentatively be the cause of the oscillations. A spin-vector simulation of the trueFISP sequence, as it was used in the actual experiment, revealed some noteworthy phenomena (Figure 18). In the simulation, the effect of different amounts of resonant offsets, as well as flip angles deviating from the ideal 90°/180° values, were investigated. T_1 and T_2

† The PSF is a measure of how the signal from a single voxel propagates to the image domain, and can be used to quantify effects of susceptibility and chemical shift (Robson *et al.* 1997).

relaxation were not included in the simulation. Despite the similar parameters used in Figure 18a–d, the resulting signals differ substantially. Especially Figure 18c presents a signal evolution similar to the result obtained in the actual experiment. Non-ideal flip angles alone cannot explain the signal oscillations, since these are visible also when using ideal flip angles (b and d). The outcome of the simulation suggests that resonant offset may have partly contributed to the apparent T_2 relaxation, as measured in Paper II. Thus, the estimated relaxation times of the ^{13}C imaging agent *in vitro* and *in vivo* could be regarded as a lower limit. Furthermore, small variations of the flip angle (1°-steps) around the ideal 180° value were found to produce substantial variations in the signal evolution. This sensitivity may explain the tendency towards increased signal fluctuation, as observed in Figure 4 of Paper II.

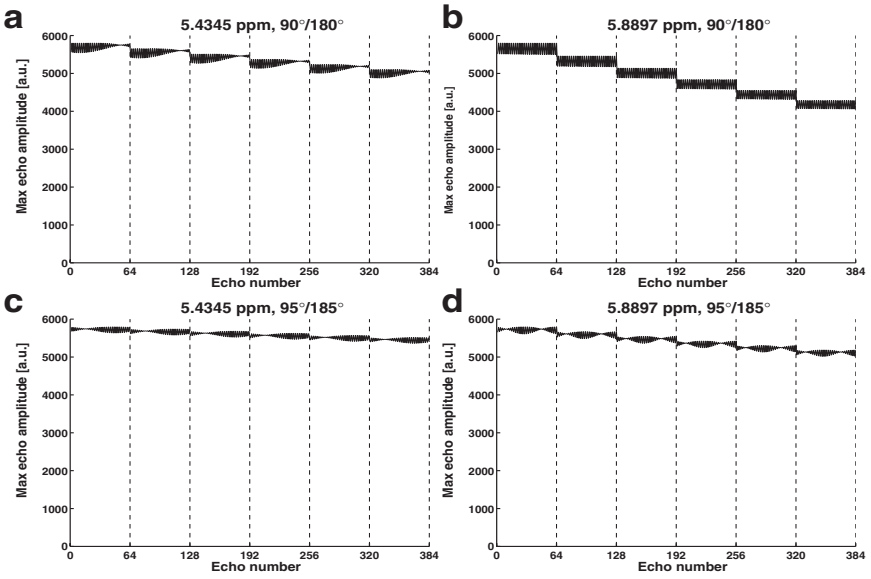

Figure 18. Simulation of the ^{13}C signal from 6 consecutive trueFISP images, corresponding to the *in vitro* experiment performed on static spins in Paper II (c.f. Figure 11). The resonant offset and the flip angles of the $\theta/2$- and θ-pulses are shown in the figures a–d. The simulation assumed infinite T_1 and T_2 relaxation times, and a complete removal of transverse magnetization after the flip-back $\theta/2$-pulse terminating each image. The simulation was based on $1{\cdot}10^6$ spin isochromats.

5.3 Hyperpolarized ^{3}He ventilation imaging in animals

5.3.1 Aspects on T_1 relaxation

Once created by the polarizing equipment, the hyperpolarized state is subject to various T_1 relaxation mechanisms (see section 2.4.1). The successful application of hyperpolarized substances relies on the polarization level being preserved until the nuclei reach the imaging location, and it is therefore essential to minimize polarization losses caused by T_1 relaxation.

Due to the high diffusion coefficient of ^{3}He, magnetic gradients may significantly depolarize the gas during the experiments (Papers III and IV). This effect was investigated theoretically by modeling the fringe field of the imaging magnet and inserting the calculated gradients in Eq. [12]. The fringe field was calculated from six current loops using the Biot-Savart law (Figure 19a). For each point in the *xz*-plane, the gradient of the field component perpendicular to the $\boldsymbol{B}_z$ direction was calculated. A measurement of the fringe field along the main axis of the magnet demonstrated excellent agreement with the calculated values (Figure 19b).

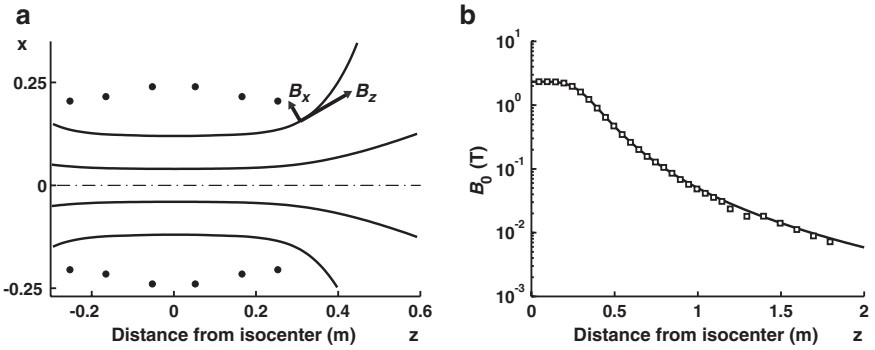

Figure 19. The fringe field was modeled by six circular current loops, indicated by (•) in (a). The calculated (—) and measured (□) B_0 field along the magnet main axis is plotted in (b). (Field measurement data courtesy of M. Månsson, Amersham Health R&D.)

The resulting T_1 relaxation rate of ^{3}He in the vicinity of the magnet, as calculated from Eq. [12], is depicted in Figure 20. The Tedlar bag contain-

ing ^{3}He was located about 1.5 m from the magnet isocenter. At this location, the gradient-induced T_1 relaxation time was about 50 min, whereas the shortest T_1 along the glass tube transporting the gas to the animal was about 4.5 min.† The total polarization decay in the glass tube when integrated over its full length corresponds to a T_1 of ~11 min.† As seen in Figure 20, the shortest T_1 values on the whole are found near the edges of the magnet bore, where the T_1 can be as short as 2 min.

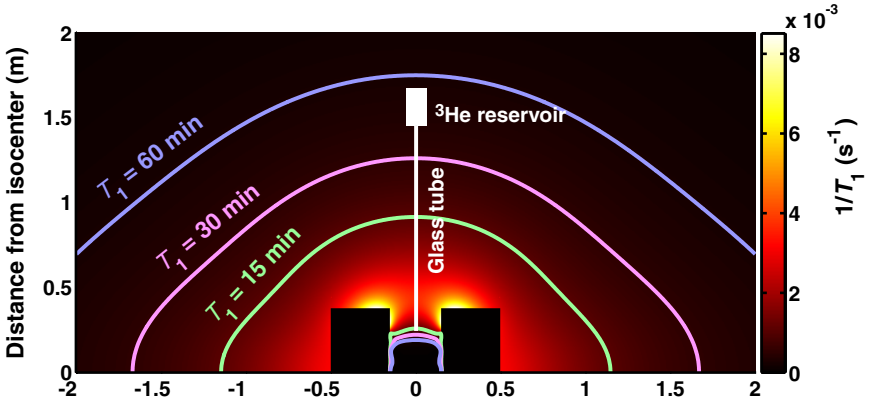

Figure 20. Map of ^{3}He relaxation rate induced by magnetic gradients of the fringe field around the imaging magnet. The positions of the ^{3}He reservoir and the glass tube transporting ^{3}He to the animal are indicated in the figure.

These estimations of the gradient-induced relaxation time can be compared to the effects of surface relaxation in the Tedlar bag and in the glass tube. After relaxation measurements in a homogeneous magnetic field, using a dedicated calibration station (Amersham Health), the surface relaxation coefficient η (cf. Eq. [9]) was estimated at ≈8.4 h cm^{-1} for the glass tube and at ≈5.4 h cm^{-1} for the Tedlar bag. Based on these values, the surface relaxation time T_1 was estimated at ~160 min in the Tedlar bag and at ~20 min in the glass tube during the imaging experiments. Thus, the fringe-field gradients contributed more to the overall relaxation of ^{3}He than the surface relaxation. The combined effects of gradients and surface relaxation resulted in

† The T_1 value is calculated for free diffusion. The actual value is expected to be slightly longer because the diffusion is restricted along the direction perpendicular to the tube.

a theoretical T_1 of ~38 min in the Tedlar bag, which agrees well with values of 25–40 min obtained during the experiments in Papers III and IV. In the glass tube, the corresponding total T_1 value was ~7 min. Under the experimental conditions in Papers III and IV, with an interval of about 0.5 min between successive ^{3}He images, the polarization loss within the glass tube (corresponding to a volume of less than one breath) can thus be estimated at ~7%. To avoid this loss, the ventilator could possibly be redesigned to flush away the gas contained in the tube before each ^{3}He-inspiration period. To obtain prolonged relaxation times in the Tedlar bag, active shielding against magnetic gradients may be employed.

Another potential source of depolarization of ^{3}He is leakage of oxygen from the surrounding atmosphere into the ventilator. To reach T_1 relaxation times of 7 min (38 min), a pO_2 as low as ~6 mbar (~1 mbar) would suffice, if this had been the only relaxation mechanism (Eq. [10]). It can therefore not be ruled out that leakage of oxygen was the dominant source of relaxation during the experiments in Papers III and IV.

For the ^{129}Xe experiments in Paper V, the T_1 relaxation induced by magnetic gradients was of minor importance, due to the much lower (~35 times) diffusion constant of ^{129}Xe, as compared with ^{3}He.

5.3.2 Pulse sequence considerations

Noble-gas imaging of the lungs has hitherto mainly employed gradient-echo sequences using low flip angles. The possibilities to use single-shot imaging sequences (e.g., EPI, trueFISP, and rapid acquisition with relaxation enhancement (RARE)) are limited by the high diffusion coefficients of the gases, especially in the case of ^{3}He. Loss of phase coherence of the nuclei, and hence of signal, is induced by the random diffusion movement within magnetic gradients, caused by susceptibility differences within the lungs (Wong *et al.* 1999), as well as by the imaging gradients of the pulse sequence. The signal loss due to the latter gradients can be expressed by the *b*-value

$$\boldsymbol{b}(t) = \int_{\tau=0}^{t} \boldsymbol{k}(\tau)^2 \, d\tau, \qquad \boldsymbol{k}(\tau) = \gamma \int_{\tau'=0}^{\tau} \boldsymbol{G}(\tau') d\tau' \qquad [28]$$

resulting in a signal attenuation of $\exp(-\boldsymbol{b}D)$, which becomes increasingly severe with increasing spatial resolution (Brandl and Haase 1994). Successful application of RARE (Durand *et al.* 2002) and trueFISP (Mugler *et al.*

2002) to ^{3}He MRI of humans have been reported, albeit at a low resolution (~5–10 mm in-plane) compared to the small animal studies in Papers III and IV (~1-mm resolution). Due to the effect of diffusion, the low flip angle FLASH sequence was chosen for these experiments.

Because no magnetization is regained from one RF excitation to the next in the FLASH sequence, the signal at the *k*-space center, for the linear phase-encoding scheme employed in Papers III and IV, is expected to vary according to

$$S(\theta) = const \cdot \cos^{\frac{N}{2}}(\theta)\sin(\theta) \qquad [29]$$

where θ is the flip angle and N the total number of RF excitations. From Eq. [29], it can easily be derived (Mugler 1998) that the optimal flip angle is given by

$$\theta_{opt} = \text{atan}\left(\sqrt{2/N}\right). \qquad [30]$$

If the optimal flip angle is inserted in Eq. [29], one obtains $S(\theta_{opt}) = const \cdot 0.11$ for $N = 64$ and $S(\theta_{opt}) = const \cdot 0.08$ for $N = 128$,† which could give the impression that the achievable SNR depended on the total number of RF excitations. However, for a fixed voxel volume and receiver bandwidth, the SNR is proportional to $N^{1/2}S(\theta_{opt})$ — an expression which is roughly constant for $N > 20$. An additional remark can be made regarding the signal amplitude after the N-th RF excitation (if the phase-encoding gradients are switched off): this amplitude is, to good approximation, exp(–1) times the amplitude after the 1st RF excitation when θ_{opt} is employed. This simple relation was used to verify the proper adjustment of the flip angle (Papers III and IV).

The above discussion concerning the optimal flip angle assumes that the full image is acquired after a single inspiration of hyperpolarized gas. However, the FLASH sequence (Papers III and IV), in combination with the computer-controlled ventilator described in section 3.2, permits the acquisition of a single image to be distributed over several consecutive inspirations, i.e., a fraction of the *k*-space is covered during each inspiration ("segmented" image acquisition). This strategy may be necessary to avoid excessively long

† See Table 4.

breath-holding periods during, e.g., the acquisition of large-matrix 3D images. If, in this fashion, n breaths are employed instead of a single breath, a roughly $\sqrt{n}$-fold increase of SNR will result, albeit with n times increased gas consumption. To avoid abrupt signal variations in the k-space between the breaths, however, care must be taken concerning the ordering of the phase-encoding steps. As illustrated in Figure 21, ghosting artifacts may result with sequential phase-encoding order of breaths (1-1-1-2-2-2-3-3-3…), whereas the ghosting is completely suppressed with the ordering employed in, e.g., RARE imaging (1-2-3-1-2-3-1-2-3…). The images in Figure 21 are simulations of a FLASH sequence employing the optimal flip angle according to Eq. [30]. The situation in 3D imaging is more complex, since the ghosting artifacts can appear in two phase-encoding directions.

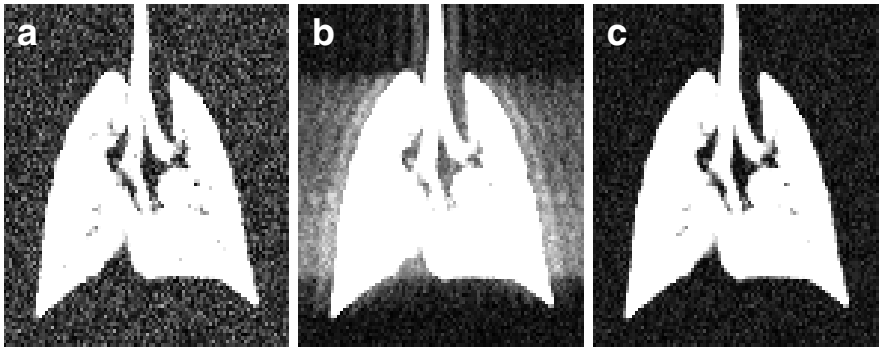

Figure 21. Simulated 2D FLASH ^{3}He lung images illustrating the effect of segmented image acquisition using a) one ^{3}He inspiration (non-segmented), b) 6 inspirations with sequential phase-encoding, and c) 6 inspirations with RARE-type phase-encoding. Note the ghosting in image (b) and lower SNR of image (a). All images have a matrix size of 96×96. The grayscale is adjusted to display the lower 1/3 of the intensity range.

5.4 Measurement of the uptake of ^{129}Xe in the lung

The method to dynamically measure the uptake of ^{129}Xe from the alveolar gas space to the pulmonary blood (Paper V) employed a 90° RF pulse to destroy the hyperpolarization in the lung parenchyma and in the blood. This saturation pulse was, after a delay Δ, followed by a second 90° pulse, creat-

ing a free induction decay (FID) signal from the ^{129}Xe having diffused from the alveoli into the lung parenchyma during the delay Δ.

It is essential that the RF pulses are carefully adjusted to a 90° flip angle at the tissue/blood resonances (at 197/212 ppm, respectively), but the flip angle at the gas resonance (at 0 ppm) must be kept small. A too high flip angle at the gas resonance will deplete the polarization of the alveolar gas, with a corresponding reduction in SNR for the subsequent FID accumulations. Further, a high flip angle on the gas resonance will create a gas peak many times larger than the tissue/blood peaks, thereby introducing a problem with too high dynamic range of the spectrum. On the other hand, it is desired to excite the gas resonance with a flip angle slightly larger than zero, since the position of the gas resonance peak provides the 0-ppm reference frequency of the spectrum. Further, the decay of the gas signal amplitude over time provide information about the size of the gas space within a respiratory unit.

In Paper V, a short rectangular 90° RF pulse was used, with the excitation frequency centered between the resonance frequencies of tissue and blood. Under the assumption that the spectral excitation profile of the pulse is described by a sinc-function, the pulse duration should be adjusted to δ_f^{-1}, where δ_f is the frequency shift between the excitation frequency and the gas resonance frequency. Another possibility is to use a shaped pulse of sufficient length, e.g. a gaussion pulse (Ruppert *et al.* 2000a). During the experiments in Paper V, a 174 μs rectangular pulse was used, which resulted in gas signal amplitudes about 1–2 times higher than the blood/tissue amplitudes. A similar suppression of the gas signal was obtained in pilot experiments using a 500 μs gaussian pulse. However, the rectangular pulse shape was preferred due to superior SNR of the spectra.

A volume coil was used for excitation and signal detection. Presumably, a surface coil could result in improved sensitivity when used to receive the signal, but will cause a problem of non-uniform flip angles if used for excitation. As a potential improvement of the method, a surface coil could be used for signal detection, while keeping the volume coil for transmission of the excitation pulses. A substantial increase of the SNR would open for the use of low flip-angle excitations, rather than 90° excitations. Using the former approach, the uptake of ^{129}Xe could be probed by a single, rapid train of low-angle pulses after a single inspiration of ^{129}Xe, which would greatly reduce the overall duration of the experiment, and moreover remove the requirement for multiple gas inspirations of equal tidal volumes.

6 Conclusions

The phantom study in Paper I indicated that a flowing hyperpolarized substance could be imaged using an ultra-fast EPI sequence. ^{129}Xe has suitable properties for MRA when dissolved in ethanol, but is less favorable when employed *in vivo* (short T_2^*). Under optimized *in vivo* conditions (isotopically enriched ^{129}Xe, polarization levels >25%, bolus concentrations >40 mM), it was estimated that the SNR would be sufficient for EPI angiography, but the success of this technique is hampered by the short transverse relaxation time of ^{129}Xe, which may only be ameliorated by improved carrier agents.

A superior imaging agent with respect to prolonged relaxation times was found in the ^{13}C-based substance, which was investigated in Paper II. In this study, a trueFISP sequence was employed, which enabled the depiction of *in vivo* angiograms with high SNR (up to ~500). The novel ^{13}C imaging agent holds promise for being useful in angiographic and, potentially, in quantitative perfusion applications. Besides the SNR aspect, unique properties of hyperpolarized nuclei — such as lack of background signal from surrounding tissues and the possibility to selectively destroy the signal by means of RF excitations — may add value as compared with existing techniques.

To date, the most widespread application of hyperpolarized gas MRI is ^{3}He lung imaging. In Paper III, a method was developed to obtain a quantitative measure of regional pulmonary ventilation from high-resolution, spin-density ^{3}He images. This method was able, as demonstrated in Paper IV, to quantify gradients of regional ventilation depending on the posture of the subject, which previously have not been demonstrated in animals as small as the rat. The prospective of gaining physiological, rather than morphological, information can increase the value of hyperpolarized substances both within clinical examinations and within pharmacological research.

In Paper V, hyperpolarized ^{129}Xe gas was inhaled and measured using a spectroscopic technique. This method, which currently provides a global measure across the lung without localized information, further emphasizes the physiological aspects of hyperpolarized NMR investigations. As demonstrated in the paper, several physiological parameters (e.g., the thickness of the respiratory membrane) were altered in animals with inflammatory lung injury as compared with healthy control animals, whereas other parameters remained unaffected (e.g., the pulmonary perfusion). Thus, hyperpolarized substances may assist the diagnosis and characterization of various disease conditions of the lung.

7 Acknowledgements

The writing of a thesis is not simple or easily won, and I would not have been able to complete this task without a great deal of help from many friends and colleagues, all included. I am deeply grateful to all of you. However, I would like to mention in particular:

My supervisors, Professors **Freddy Ståhlberg** and **Kjell Lindström**. Freddy, for your impressive accuracy in pinpointing relevant and irrelevant parts of the thesis, and Kjell, for your confidence when setting up tough deadlines, without which the thesis would not have been completed this year.

Professor **Klaes Golman**, for creating a unique research environment and giving me the opportunity to write this thesis.

Anselm Deninger and **Jan Wolber**, for spending numerous hours on giving excellent comments and suggestions to both the papers and the thesis. (Anselm, I've counted 186 emails to/from you!).

Edvin Johansson and **Jonas Svensson**, for both interesting and enjoyable MRI-discussions, and for the pleasant collaboration during all the hyperpolarized experiments.

Lars E. Olsson, for sharp-eyed and helpful criticism.

Jan-Henrik Ardenkjœr-Larsen, **Oskar Axelsson**, **Haukur Jóhannesson**, **Ib Leunbach**, **Peter Magnusson**, **J. Stefan Petersson**, **Göran Pettersson**, and **Per Wollmer** — for many comments and suggestions during the work on the papers.

All other co-authors not mentioned so far — it has been a pleasure to work together with you.

Birgit, **Britt-Marie** and **Kerstin** — I am most grateful for all help with the animal handling during this period!

Other colleagues at Amersham Health R&D and Dept. of Experimental Research. Thank you for having had patience (I hope!) with me during this busy period!

My parents, **Birgitta** and **Bertil** — thank you for being my parents!

Last but not least, **Maria**, for your love and support during this time, and for still being my wife, despite the fact that we haven't seen each other very often the last half year.

8 References

ABRAGAM A, GOLDMAN M. Principles of dynamic nuclear polarisation. *Rep Prog Phys* 1978; 41:395–467.

ALBERT MS, BALAMORE D. Development of hyperpolarized noble gas MRI. *Nucl Instrum Methods Phys Res A* 1998; 402:441–453.

ALBERT MS, BALAMORE D, KACHER DF, VENKATESH AK, JOLESZ FA. Hyperpolarized ^{129}Xe T_1 in oxygenated and deoxygenated blood. *NMR Biomed* 2000; 13:407–414.

ALBERT MS, CATES GD, DRIEHUYS B, HAPPER W, SAAM B, SPRINGER CS, JR., WISHNIA A. Biological magnetic resonance imaging using laser-polarized ^{129}Xe. *Nature* 1994; 370:199–201.

ALBERT MS, KACHER DF, BALAMORE D, VENKATESH AK, JOLESZ FA. T_1 of ^{129}Xe in blood and the role of oxygenation. *J Magn Reson* 1999; 140:264–273.

ALBERT MS, TSENG CH, WILLIAMSON D, OTEIZA ER, WALSWORTH RL, KRAFT B, KACHER D, HOLMAN BL, JOLESZ FA. Hyperpolarized ^{129}Xe MR imaging of the oral cavity. *J Magn Reson B* 1996; 111:204–207.

AUSTIN BB. The effective resistance of inductance coils at radio frequency. *Wireless Eng* 1934; 11:12–16.

AZIZ TS. Xenon in anesthesia. *Int Anesthesiol Clin* 2001; 39:1–14.

BACHERT P, SCHAD LR, BOCK M, KNOPP MV, EBERT M, GROSSMANN T, HEIL W, HOFMANN D, SURKAU R, OTTEN EW. Nuclear magnetic resonance imaging of airways in humans with use of hyperpolarized ^{3}He. *Magn Reson Med* 1996; 36:192–196.

BERGIN CJ, GLOVER GH, PAULY JM. Lung parenchyma: magnetic susceptibility in MR imaging. *Radiology* 1991; 180:845–848.

BERGIN CJ, GLOVER GM, PAULY J. Magnetic resonance imaging of lung parenchyma. *J Thorac Imaging* 1993; 8:12–17.

BIFONE A. Production of optically polarized xenon for medical applications. In: Maraviglia B, ed. Magnetic resonance and brain function: approaches from physics. IOS Press, Amsterdam 1999. p. 493–503.

BIFONE A, SONG YQ, SEYDOUX R, TAYLOR RE, GOODSON BM, PIETRASS T, BUDINGER TF, NAVON G, PINES A. NMR of laser-polarized xenon in human blood. *Proc Natl Acad Sci U S A* 1996; 93:12932–12936.

BLOCH F, HANSEN WW, PACKARD M. The nuclear induction experiment. *Phys Rev* 1946; 70:474–485.

BOCK M. Simultaneous T_2^* and diffusion measurements with ^{3}He. *Magn Reson Med* 1997; 38:890–895.

BOUCHIAT MA, CARVER TR, VARNUM CM. Nuclear polarization in He^3 gas induced by optical pumping and dipolar exchange. *Phys Rev Lett* 1960; 5:373–375.

BRANDL M, HAASE A. Molecular diffusion in NMR microscopy. *J Magn Reson B* 1994; 103:162–167.

BRAUER RW, HOGAN PM, HUGON M, MACDONALD AG, MILLER KW. Patterns of interaction of effects of light metabolically inert gases with those of hydrostatic pressure as such: a review. *Undersea Biomed Res* 1982; 9:353–396.

BUROV NE, DZHABAROV DA, OSTAPCHENKO DA, KORNIENKO L, SHULUNOV MV. [Clinical stages and subjective sensations in xenon anesthesia]. *Anesteziol Reanimatol* 1993; 7–11.

CALLOT V, CANET E, BROCHOT J, VIALLON M, HUMBLOT H, BRIGUET A, TOURNIER H, CREMILLIEUX Y. MR perfusion imaging using encapsulated laser-polarized ^{3}He. *Magn Reson Med* 2001; 46:535–540.

CATES GD, SCHAEFER SR, HAPPER W. Relaxation of spins due to field inhomogeneities in gaseous samples at low magnetic fields and low pressures. *Phys Rev A* 1988; 37:2877–2885.

CHANN B, NELSON IA, ANDERSON LW, DRIEHUYS B, WALKER TG. ^{129}Xe-Xe molecular spin relaxation. *Phys Rev Lett* 2002; 88:113201.

CHAWLA MS, CHEN XJ, COFER GP, HEDLUND LW, KERBY MB, OTTOBONI TB, JOHNSON GA. Hyperpolarized ^{3}He microspheres as a novel vascular signal source for MRI. *Magn Reson Med* 2000; 43:440–445.

CHAWLA MS, CHEN XJ, MÖLLER HE, COFER GP, WHEELER CT, HEDLUND LW, JOHNSON GA. In vivo magnetic resonance vascular imaging using laser-polarized ^{3}He microbubbles. *Proc Natl Acad Sci U S A* 1998; 95:10832–10835.

CHEN XJ, MÖLLER HE, CHAWLA MS, COFER GP, DRIEHUYS B, HEDLUND LW, JOHNSON GA. Spatially resolved measurements of hyperpolarized gas properties in the lung in vivo. Part I: diffusion coefficient. *Magn Reson Med* 1999a; 42:721–728.

CHEN XJ, MÖLLER HE, CHAWLA MS, COFER GP, DRIEHUYS B, HEDLUND LW, MACFALL JR, JOHNSON GA. Spatially resolved measurements of hyperpolarized gas properties in the lung in vivo. Part II: T_2^*. *Magn Reson Med* 1999b; 42:729–737.

COLEGROVE FD, FRANKEN PA. Optical pumping of helium in the $^3S_1$ metastable state. *Phys Rev* 1960; 119:680–690.

COLEGROVE FD, SCHEARER LD, WALTERS GK. Polarization of He^3 gas by optical pumping. *Phys Rev* 1963; 132:2561–2572.

CREMILLIEUX Y, BERTHEZENE Y, HUMBLOT H, VIALLON M, CANET E, BOURGEOIS M, ALBERT T, HEIL W, BRIGUET A. A combined ^{1}H perfusion/^{3}He ventilation NMR study in rat lungs. *Magn Reson Med* 1999; 41:645–648.

DANIELS JM, SHEARER LD, LEDUC M, NACHER PJ. Polarizing ^{3}He nuclei with neodymium $La_{1-x}Nd_xMgAl_{11}O_{19}$ lasers. *J Opt Soc Am* 1987; B4:1133–1135.

DENINGER AJ, EBERLE B, BERMUTH J, ESCAT B, MARKSTALLER K, SCHMIEDESKAMP J, SCHREIBER WG, SURKAU R, OTTEN E, KAUCZOR HU. Assessment of a single-acquisition imaging sequence for oxygen-sensitive ^{3}He-MRI. *Magn Reson Med* 2002; 47:105–114.

DENINGER AJ, EBERLE B, EBERT M, GROSSMANN T, HEIL W, KAUCZOR H, LAUER L, MARKSTALLER K, OTTEN E, SCHMIEDESKAMP J, SCHREIBER W, SURKAU R, THELEN M, WEILER N. Quantification of regional intrapulmonary oxygen partial pressure evolution during apnea by ^{3}He MRI. *J Magn Reson* 1999; 141:207–216.

DOWSE HB, NORTON S, SIDELL BD. The estimation of the diffusion constant and solubility of O(2)in tissue using kinetics. *J Theor Biol* 2000; 207:531–541.

DRIEHUYS B, CATES GD, HAPPER W. Surface relaxation mechanisms of laser-polarized ^{129}Xe. *Phys Rev Lett* 1995; 74:4943–4946.

DRIEHUYS B, CATES GD, MIRON E, SAUER K, WALTER DK, HAPPER W. High-volume production of laser-polarized ^{129}Xe. *Appl Phys Lett* 1996; 69:1668–1670.

DUHAMEL G, CHOQUET P, GRILLON E, LAMALLE L, LEVIEL JL, ZIEGLER A, CONSTANTINESCO A. ^{129}Xe MR imaging and spectroscopy of rat brain using arterial delivery of hyperpolarized xenon in a lipid emulsion. *Magn Reson Med* 2001; 46:208–212.

DURAND E, GUILLOT G, DARRASSE L, TASTEVIN G, NACHER PJ, VIGNAUD A, VATTOLO D, BITTOUN J. CPMG measurements and ultrafast imaging in human lungs with hyperpolarized ^{3}He at low field (0.1 T). *Magn Reson Med* 2002; 47:75–81.

EBERLE B. Quantification of regional intrapulmonary oxygen partial pressure (pO_2). In: Proc HELION 02, Oppenheim 2002, p. 34.

EBERT M, GROSSMANN T, HEIL W, OTTEN WE, SURKAU R, LEDUC M, BACHERT P, KNOPP MV, SCHAD LR, THELEN M. Nuclear magnetic resonance imaging with hyperpolarised ^{3}He. *Lancet* 1996; 347:1297–1299.

EDELSTEIN WA, GLOVER GH, HARDY CJ, REDINGTON RW. The intrinsic signal-to-noise ratio in NMR imaging. *Magn Reson Med* 1986; 3:604–618.

FAES TJ, VAN DER MEIJ HA, DE MUNCK JC, HEETHAAR RM. The electric resistivity of human tissues (100 Hz–10 MHz): a meta-analysis of review studies. *Physiol Meas* 1999; 20:R1–10.

FICK A. Über Diffusion. *Ann Phys-Leipzig* 1855; 170:59–86.

FITZSIMMONS WA, TANKERSLEY LL, WALTERS GK. Nature of surface-induced nuclear-spin relaxation of gaseous He^{3}. *Phys Rev* 1969; 179:156–165.

FRANKEN PA, COLEGROVE FD. Alignment of metastable helium atoms by unpolarized resonance radiation. *Phys Rev Lett* 1958; 1:316–318.

FROSSATI G. Polarization of ^{3}He, D_2 (and possibly ^{129}Xe) using cryogenic techniques. *Nucl Instrum Meth A* 1998; 402:479–483.

GAMBLIN RL, CARVER TR. Polarization and relaxation processes in He^{3} gas. *Phys Rev* 1965; 138:A946–A960.

GATZKE M, CATES GD, DRIEHUYS B, FOX D, HAPPER W, SAAM B. Extraordinarily slow nuclear spin relaxation in frozen laser-polarized ^{129}Xe. *Physical Review Letters* 1993; 70:690–693.

GENTILE TR, CHEN W, THOMPSON AK, SNOW WM, BAILEY C, HUSSEY D, JONES GL. Neutron spin filter development at NIST and Indiana University. In: Proc HELION 02, Oppenheim 2002, p. 24.

GENTILE TR, RICH DR, THOMPSON AK, SNOW WM, JONES GL. Compressing spin-polarized ^{3}He with a modified diaphragm pump. *J Research NIST* 2001; 106:709–729.

GIERADA DS, SAAM B, YABLONSKIY D, COOPER JD, LEFRAK SS, CONRADI MS. Dynamic echo planar MR imaging of lung ventilation with hyperpolarized ^{3}He in normal subjects and patients with severe emphysema. *NMR Biomed* 2000; 13:176–181.

GOLMAN K, ARDENKJAER-LARSEN JH, SVENSSON J, AXELSSON O, HANSSON G, HANSSON L, JOHANNESSON H, LEUNBACH I, MÅNSSON S, PETERSSON JS, PETTERSSON G, SERVIN R, WISTRAND LG. ^{13}C-angiography. *Acad Radiol* 2002; 9: Suppl 2, S507–S510.

GOLMAN K, AXELSSON O, JOHANNESSON H, MÅNSSON S, OLOFSSON C, PETERSSON JS. Parahydrogen-induced polarization in imaging: subsecond ^{13}C angiography. *Magn Reson Med* 2001; 46:1–5.

GOLMAN K, PETERSSON JS, ARDENKJAER-LARSEN JH, LEUNBACH I, WISTRAND LG, EHNHOLM G, LIU K. Dynamic in vivo oxymetry using overhauser enhanced MR imaging. *J Magn Reson Imaging* 2000; 12:929–938.

GOODSON BM. Using injectable carriers of laser-polarized noble gases for enhancing NMR and MRI. *Concept Magnetic Res* 1999; 11:203–223.

GOODSON BM. Nuclear magnetic resonance of laser-polarized noble gases in molecules, materials, and organisms. *J Magn Reson* 2002; 155:157–216.

GROSSMANN T. Realisierung des ^{3}He-Kreislaufs zur ^{3}He-Magnet-Resonanz-Tomographie. PhD Thesis, Johannes Gutenberg-Universität, Mainz 2000.

GROVER BC. Noble-gas NMR detection through noble-gas-rubidium hyperfine contact interaction. *Phys Rev Lett* 1978; 40:391–392.

GUR D, YONAS H, GOOD WF. Local cerebral blood flow by xenon-enhanced CT: current status, potential improvements, and future directions. *Cerebrovasc Brain Metab Rev* 1989; 1:68–86.

GUYTON AC. Textbook of Medical Physiology, 7 ed. W. B. Saunders, Philadelphia 1986.

HAASE A, FRAHM J, MATTHAEI D, HÄNICKE W, MERBOLDT K-D. FLASH imaging. Rapid NMR imaging using low flip-angle pulses. *J Magn Reson* 1986; 67:258–266.

HALL DA, MAUS DC, GERFEN GJ, INATI SJ, BECERRA LR, DAHLQUIST FW, GRIFFIN RG. Polarization-enhanced NMR spectroscopy of biomolecules in frozen solution. *Science* 1997; 276:930–932.

HAPPER W. Optical pumping. *Rev Mod Phys* 1972; 44:169–249.

HARRIS RK. Nuclear magnetic resonance spectroscopy: a physicochemical view. Longman Scientific & Technical, Essex 1983.

HEDLUND LW, COFER GP, OWEN SJ, ALLAN JOHNSON G. MR-compatible ventilator for small animals: computer-controlled ventilation for proton and noble gas imaging. *Magn Reson Imaging* 2000; 18:753–759.

HEIL W, HUMBLOT H, OTTEN E, SCHAFER M, SARKAU R, LEDUC M. Very long nuclear relaxation times of spin polarized ^{3}He in metal coated cells. *Phys Lett A* 1995; A201:337–343.

HIMM JF. The solubility of xenon in simple organic solvents and in aqueous amino acid solutions. PhD Thesis, Michigan State University 1986.

HOULT DI, LAUTERBUR PC. The sensitivity of the zeugmatographic experiment involving human samples. *J Magn Reson* 1979; 34:425–433.

HOULT DI, RICHARDS RE. The signal-to-noise ratio of the nuclear magnetic resonance experiment. *J Magn Reson* 1976; 24:71–85.

HSU MF, CATES GD, KOMINIS I. Sol-gel coated glass cells for spin-exchange polarized ^{3}He. *Appl Phys Lett* 2000; 77:2069–2071.

HUNT ER, CARR HY. Nuclear magnetic resonance of Xe^{129} in natural xenon. *Phys Rev* 1963; 130:2302–2305.

INSKO EK, ELLIOTT MA, SCHOTLAND JC, LEIGH JS. Generalized reciprocity. *J Magn Reson* 1998; 131:111–117.

JAMESON CJ, JAMESON AK, HWANG JK. Nuclear spin relaxation by intermolecular magnetic dipole coupling in the gas phase. ^{129}Xe in oxygen. *J Chem Phys* 1988; 89:4074–4081.

JOHNSON GA, CATES G, CHEN XJ, COFER GP, DRIEHUYS B, HAPPER W, HEDLUND LW, SAAM B, SHATTUCK MD, SWARTZ J. Dynamics of magnetization in hyperpolarized gas MRI of the lung. *Magn Reson Med* 1997; 38:66–71.

KASTLER A. Quelques suggestions concernant la production optique et la détection optique d'une inégalité de population des niveaux de quantification spatiale des atomes: application à l'expérience de Stern et Gerlach et à la résonance magnétique. *J Phys Rad* 1950; 11:255–265.

KAUCZOR H, SURKAU R, ROBERTS T. MRI using hyperpolarized noble gases. *Eur Radiol* 1998; 8:820–827.

KAUCZOR HU, HANKE A, VAN BEEK EJ. Assessment of lung ventilation by MR imaging: current status and future perspectives. *Eur Radiol* 2002; 12:1962–1970.

KAUCZOR HU, HOFMANN D, KREITNER KF, NILGENS H, SURKAU R, HEIL W, POTTHAST A, KNOPP MV, OTTEN EW, THELEN M. Normal and abnormal pulmonary ventilation: visualization at hyperpolarized ^{3}He MR imaging. *Radiology* 1996; 201:564–568.

KILIAN W. Erzeugung von hyperpolarisiertem ^{129}Xe-Gas und Nachweis mittels *in vivo* NMR-Bildgebung, NMR-Spektroskopie sowie SQUID-Messtechnik. PhD Thesis, Freie Universität Berlin 2001.

LADEFOGED J, ANDERSEN AM. Solubility of ^{133}Xe at 37°C in water, saline, olive oil, liquid paraffin, solutions of albumin, and blood. *Phys Med Biol* 1967; 12:353–358.

LAUTERBUR PC. Image formation by induced local interactions: examples employing nuclear magnetic resonance. *Nature* 1973; 242:190–191.

LAVINI C, PAYNE GS, LEACH MO, BIFONE A. Intravenous delivery of hyperpolarized ^{129}Xe: a compartmental model. *NMR Biomed* 2000; 13:238–244.

LIPSON DA, ROBERTS DA, HANSEN-FLASCHEN J, GENTILE TR, JONES G, THOMPSON A, DIMITROV IE, PALEVSKY HI, LEIGH JS, SCHNALL M, RIZI RR. Pulmonary ventilation and perfusion scanning using hyperpolarized ^{3}He MRI and arterial spin tagging in healthy normal subjects and in pulmonary embolism and orthotopic lung transplant patients. *Magn Reson Med* 2002; 47:1073–1076.

MACFALL JR, CHARLES HC, BLACK RD, MIDDLETON H, SWARTZ JC, SAAM B, DRIEHUYS B, ERICKSON C, HAPPER W, CATES G D, JOHNSON GA, RAVIN CE. Human lung air spaces: potential for MR imaging with hyperpolarized ^{3}He. *Radiology* 1996; 200:553–558.

MACOVSKI A. Noise in MRI. *Magn Reson Med* 1996; 36:494–497.

MAKI JH, CHENEVERT TL, PRINCE MR. Three-dimensional contrast-enhanced MR angiography. *Top Magn Reson Imaging* 1996; 8:322–344.

MANSFIELD P. Multi-planar image formation using NMR spin echoes. *J Phys C Solid State* 1977; 10:L55–L58.

MARTIN CC, WILLIAMS RF, GAO JH, NICKERSON LD, XIONG J, FOX PT. The pharmacokinetics of hyperpolarized xenon: implications for cerebral MRI. *J Magn Reson Imaging* 1997; 7:848–854.

MERBACH A, TÓTH É (eds). The Chemistry of Contrast Agents in Medical Magnetic Resonance Imaging. John Wiley & Sons, Chichester 2001.

MIDDLETON H, BLACK RD, SAAM B, CATES GD, COFER GP, GUENTHER R, HAPPER W, HEDLUND LW, JOHNSON GA, JUVAN K, *et al*. MR imaging with hyperpolarized ^{3}He gas. *Magn Reson Med* 1995; 33:271–275.

MILLER KW, REO NV, SCHOOT UITERKAMP AJ, STENGLE DP, STENGLE TR, WILLIAMSON KL. Xenon NMR: chemical shifts of a general anesthetic in common solvents, proteins, and membranes. *Proc Natl Acad Sci U S A* 1981; 78:4946–4949.

MÖLLER HE, CHAWLA MS, CHEN XJ, DRIEHUYS B, HEDLUND LW, WHEELER CT, JOHNSON GA. Magnetic resonance angiography with hyperpolarized ^{129}Xe dissolved in a lipid emulsion. *Magn Reson Med* 1999; 41:1058–1064.

MÖLLER HE, CHEN XJ, SAAM B, HAGSPIEL KD, JOHNSON GA, ALTES TA, DE LANGE EE, KAUCZOR HU. MRI of the lungs using hyperpolarized noble gases. *Magn Reson Med* 2002; 47:1029–1051.

MÖLLER HE, HEDLUND LW, CHEN XJ, CAREY MR, CHAWLA MS, WHEELER CT, JOHNSON GA. Measurements of hyperpolarized gas properties in the lung. Part III: ^{3}He T_1. *Magn Reson Med* 2001; 45:421–430.

MUGLER JP 3RD, DRIEHUYS B, BROOKEMAN JR, CATES GD, BERR SS, BRYANT RG, DANIEL TM, DE LANGE EE, DOWNS JH, 3RD, ERICKSON CJ, HAPPER W, HINTON DP, KASSEL NF, MAIER T, PHILLIPS CD, SAAM BT, SAUER KL, WAGSHUL ME. MR imaging and spectroscopy using hyperpolarized ^{129}Xe gas: preliminary human results. *Magn Reson Med* 1997; 37:809–815.

MUGLER JP 3RD, SALERNO M, DE LANGE EE, BROOKEMAN JR. Optimized trueFISP hyperpolarized ^{3}He MRI of the lung yields a 3-fold SNR increase compared to FLASH. In: Proc 10th ISMRM, Honolulu 2002, p. 2019.

MUGLER JP 3RD. Optimization of gradient-echo sequences for hyperpolarized noble gas MRI. In: Proc 6th ISMRM, Sydney 1998, p. 1904.

NEWBURY N R, BARTON AS, CATES GD, HAPPER W, MIDDLETON H. Gaseous ^{3}He-^{3}He magnetic dipolar spin relaxation. *Phys Rev A* 1993; 48:4411–4420.

OCALI O, ATALAR E. Ultimate intrinsic signal-to-noise ratio in MRI. *Magn Reson Med* 1998; 39:462–473.

OLSSON LE, MAGNUSSON P, DENINGER AJ, PETTERSSON G, ÅKESSON P, PETERSSON JS, GOLMAN K. Intrapulmonary pO_2 measured by low field MR imaging of hyperpolarized ^{3}He. In: Proc 10th ISMRM, Honolulu 2002, p. 2021.

OPPELT A, GRAUMANN R, BARFUSS H, FISCHER H, HARTL W, SCHAJOR W. FISP: Eine neue schnelle Pulssequenz für die Kernspintomographie. *Electromedica* 1986; 54:15–18.

OVERHAUSER AW. Polarization of nuclei in metals. *Phys Rev* 1953; 92:411–415.

PATYAL BR, GAO JH, WILLIAMS RF, ROBY J, SAAM B, ROCKWELL BA, THOMAS RJ, STOLARSKI DJ, FOX PT. Longitudinal relaxation and diffusion measurements using magnetic resonance signals from laser-hyperpolarized ^{129}Xe nuclei. *J Magn Reson* 1997; 126:58–65.

PATZ S. Some factors that influence the steady state in steady-state free precession. *Magn Reson Imaging* 1988; 6:405–413.

PELED S, JOLESZ FA, TSENG C H, NASCIMBEN L, ALBERT MS, WALSWORTH RL. Determinants of tissue delivery for ^{129}Xe magnetic resonance in humans. *Magn Reson Med* 1996; 36:340–344.

PURCELL EM, TORREY HC, POUND RV. Resonance absorption by nuclear magnetic moments in a solid. *Phys Rev* 1946; 69:37–38.

RAMIREZ MP, SIGALOFF KC, KUBATINA LV, DONAHUE MA, VENKATESH AK, ALBERT MS. Physiological response of rats to delivery of helium and xenon: implications for hyperpolarized noble gas imaging. *NMR Biomed* 2000; 13:253–264.

ROBSON MD, GORE JC, CONSTABLE RT. Measurement of the point spread function in MRI using constant time imaging. *Magn Reson Med* 1997; 38:733–740.

RUBIN SM, SPENCE MM, GOODSON BM, WEMMER DE, PINES A. Evidence of nonspecific surface interactions between laser-polarized xenon and myoglobin in solution. *Proc Natl Acad Sci U S A* 2000; 97:9472–9475.

RUPPERT K, BROOKEMAN JR, HAGSPIEL KD, DRIEHUYS B, MUGLER JP 3RD. NMR of hyperpolarized ^{129}Xe in the canine chest: spectral dynamics during a breath-hold. *NMR Biomed* 2000a; 13:220–228.

RUPPERT K, BROOKEMAN JR, HAGSPIEL KD, MUGLER JP 3RD. Probing lung physiology with xenon polarization transfer contrast (XTC). *Magn Reson Med* 2000b; 44:349–357.

SAAM B, HAPPER W, MIDDLETON H. Nuclear relaxation of ^{3}He in the presence of O_2. *Phys Rev A* 1995; 52:862–865.

SAAM BT, YABLONSKIY DA, KODIBAGKAR VD, LEAWOODS JC, GIERADA DS, COOPER JD, LEFRAK SS, CONRADI MS. MR imaging of diffusion of ^{3}He gas in healthy and diseased lungs. *Magn Reson Med* 2000; 44:174–179.

SAKAI K, BILEK AM, OTEIZA E, WALSWORTH RL, BALAMORE D, JOLESZ FA, ALBERT MS. Temporal dynamics of hyperpolarized ^{129}Xe resonances in living rats. *J Magn Reson B* 1996; 111:300–304.

SALERNO M, ALTES TA, BROOKEMAN JR, DE LANGE EE, MUGLER JP 3RD. Dynamic spiral MRI of pulmonary gas flow using hyperpolarized ^{3}He: preliminary studies in healthy and diseased lungs. *Magn Reson Med* 2001a; 46:667–677.

SALERNO M, ALTES TA, MUGLER JP 3RD, NAKATSU M, HATABU H, DE LANGE EE. Hyperpolarized noble gas MR imaging of the lung: potential clinical applications. *Eur J Radiol* 2001b; 40:33–44.

SANDERS JK, HUNTER BK. Modern NMR spectroscopy: a guide for chemists. Oxford University Press, Oxford 1987.

SCHEARER LD, WALTERS GK. Nuclear spin-lattice relaxation in the presence of magnetic-field gradients. *Phys Rev* 1965; 139:A1398–A1402.

SCHEFFLER K. A pictorial description of steady-states in rapid magnetic resonance imaging. *Concept Magnetic Res* 1999; 11:291–304.

SCHEFFLER K, HEID O, HENNIG J. Magnetization preparation during the steady state: fat-saturated 3D TrueFISP. *Magn Reson Med* 2001; 45:1075–1080.

SVENSSON J. Contrast-enhanced magnetic resonance angiography: development and optimization of techniques for paramagnetic and hyperpolarized contrast media. PhD Thesis, Lund University, Malmö 2002.

SWANSON S D, ROSEN MS, AGRANOFF BW, COULTER KP, WELSH RC, CHUPP TE. Brain MRI with laser-polarized ^{129}Xe. *Magn Reson Med* 1997; 38:695–698.

SWANSON SD, ROSEN MS, COULTER KP, WELSH RC, CHUPP TE. Distribution and dynamics of laser-polarized ^{129}Xe magnetization in vivo. *Magn Reson Med* 1999; 42:1137–1145.

TAJIK JK, CHON D, WON C, TRAN BQ, HOFFMAN EA. Subsecond multisection CT of regional pulmonary ventilation. *Acad Radiol* 2002; 9:130–146.

TILTON RF, JR., KUNTZ ID, JR. Nuclear magnetic resonance studies of ^{129}Xe with myoglobin and hemoglobin. *Biochemistry* 1982; 21:6850–6857.

TORREY HC. Chemical shift and relaxation of Xe^{129} in xenon gas. *Phys Rev* 1963; 130:2306–2312.

TSENG C H, WONG G P, POMEROY VR, MAIR RW, HINTON DP, HOFFMANN D, STONER RE, HERSMAN FW, CORY DG, WALSWORTH RL. Low-field MRI of laser polarized noble gas. *Phys Rev Lett* 1998; 81:3785–3788.

VENKATESH AK, ZHAO L, BALAMORE D, JOLESZ FA, ALBERT MS. Evaluation of carrier agents for hyperpolarized xenon MRI. *NMR Biomed* 2000; 13:245–252.

VLAARDINGERBROEK MT, DEN BOER JA. Magnetic resonance imaging: theory and practice. Springer-Verlag, Heidelberg 1999.

WAGSHUL ME, BUTTON TM, LI HF, LIANG Z, SPRINGER CS, ZHONG K, WISHNIA A. In vivo MR imaging and spectroscopy using hyperpolarized ^{129}Xe. *Magn Reson Med* 1996; 36:183–191.

WEATHERSBEE P, HOMER L. Solubility of inert gases in biological fluids and tissues. *Undersea Biomed Res* 1980; 7:277–296.

WILD J M, PALEY MN, VIALLON M, SCHREIBER WG, VAN BEEK E J, GRIFFITHS PD. *k*-space filtering in 2D gradient-echo breath-hold hyperpolarized ^{3}He MRI: spatial resolution and signal-to-noise ratio considerations. *Magn Reson Med* 2002a; 47:687–695.

WILD JM, SCHMIEDESKAMP J, PALEY MN, FILBIR F, FICHELE S, KASUBOSKI L, KNITZ F, WOODHOUSE N, SWIFT A, HEIL W, MILL GH, WOLF M, GRIFFITHS PD, OTTEN E, VAN BEEK EJ. MR imaging of the lungs with hyperpolarized ^{3}He gas transported by air. *Phys Med Biol* 2002b; 47:N185–190.

WILSON GJ, SANTYR GE, ANDERSON ME, DELUCA JR PM. T_2 of ^{129}Xe in rat tissue homogenates and blood at 9.4 T. In: Proc 7th ISMRM, Philadelphia 1999, p. 2102.

WIND RA, DUIJVESTIJN MJ, VAN DER LUGT C, MANENSCHIJN A, VRIEND J. Applications of dynamic nuclear polarization in ^{13}C NMR in solids. *Prog Nucl Mag Res Sp* 1985; 17:33–67.

WITTENBERG LJ, SANTARIUS JF, KULCINSKI GL. Lunar source of ^{3}He for commercial fusion power. *Fusion Technol* 1986; 10:167–178.

WOESSNER DE. Relaxation effects of chemical exchange. In: Grant DI and Harris RK, eds. Encyclopedia of NMR. John Wiley & Sons, Chichester 1996. p. 4018–4028.

WOLBER J, CHERUBINI A, DZIK-JURASZ AS, LEACH MO, BIFONE A. Spin-lattice relaxation of laser-polarized xenon in human blood. *Proc Natl Acad Sci U S A* 1999a; 96:3664–3669.

WOLBER J, CHERUBINI A, LEACH MO, BIFONE A. Hyperpolarized ^{129}Xe NMR as a probe for blood oxygenation. *Magn Reson Med* 2000a; 43:491–496.

WOLBER J, CHERUBINI A, LEACH MO, BIFONE A. On the oxygenation-dependent ^{129}Xe T_1 in blood. *NMR Biomed* 2000b; 13:234–237.

WOLBER J, MCINTYRE DJ, RODRIGUES LM, CARNOCHAN P, GRIFFITHS JR, LEACH MO, BIFONE A. In vivo hyperpolarized ^{129}Xe NMR spectroscopy in tumors. *Magn Reson Med* 2001; 46:586–591.

WOLBER J, ROWLAND IJ, LEACH MO, BIFONE A. Perfluorocarbon emulsions as intravenous delivery media for hyperpolarized xenon. *Magn Reson Med* 1999b; 41:442–449.

WOLBER J, SANTORO D, LEACH MO, BIFONE A. Diffusion of hyperpolarized ^{129}Xe in biological systems: effect of chemical exchange. In: Proc 8th ISMRM, Denver 2000c, p. 754.

WOLF M. Systematische Untersuchungen zur oberflächeninduzierten Relaxation von kernspinpolarisiertem ^{3}He. Diploma Thesis, Johannes Gutenberg-Universität, Mainz 2000.

WONG GP, TSENG CH, POMEROY VR, MAIR RW, HINTON DP, HOFFMANN D, STONER RE, HERSMAN FW, CORY DG, WALSWORTH RL. A system for low field imaging of laser-polarized noble gas. *J Magn Reson* 1999; 141:217–227.

YABLONSKIY DA, SUKSTANSKII AL, LEAWOODS JC, GIERADA DS, BRETTHORST GL, LEFRAK SS, COOPER JD, CONRADI MS. Quantitative in vivo assessment of lung microstructure at the alveolar level with hyperpolarized ^{3}He diffusion MRI. *Proc Natl Acad Sci U S A* 2002; 99:3111–3116.

ZANG LH, LAUGHLIN MR, ROTHMAN DL, SHULMAN RG. ^{13}C NMR relaxation times of hepatic glycogen in vitro and in vivo. *Biochemistry* 1990; 29:6815–6820.

ZHAO L, ALBERT MS. Biomedical imaging using hyperpolarized noble gas MRI: pulse sequence considerations. *Nucl Instrum Methods Phys Res A* 1998; 402:454–460.

Paper I

Acta Radiologica 43 (2002) 455–460
Printed in Denmark · All rights reserved

Copyright © Acta Radiologica 2002

ACTA RADIOLOGICA
0284-1851

ECHO-PLANAR MR IMAGING OF DISSOLVED HYPERPOLARIZED ^{129}Xe

Potential for MR angiography

S. Månsson[1], E. Johansson[2], J. Svensson[3], L. E. Olsson[3], F. Ståhlberg[4], J. S. Petersson[5] and K. Golman[5]

[1]Department of Experimental Research, Malmö University Hospital, [2]Department of Radiation Physics, Lund University Hospital, [3]Department of Radiation Physics, Malmö University Hospital, [4]Department of Radiology, Lund University Hospital, and [5]Amersham Health R&D, Medeon, Malmö, Sweden.

Abstract

Purpose: The feasibility of hyperpolarized ^{129}Xe for fast MR angiography (MRA) was evaluated using the echo-planar imaging (EPI) technique.

Material and Methods: Hyperpolarized Xe gas was dissolved in ethanol, a carrier agent with high solubility for Xe (Ostwald solubility coefficient 2.5) and long relaxation times. The dissolved Xe was injected as a bolus into a flow phantom where the mean flow velocity was 15 cm/s. Ultrafast EPI images with 44 ms scan time were acquired of the flowing bolus and the signal-to-noise ratios (SNR) were measured.

Results: The relaxation times of hyperpolarized Xe in ethanol were measured to T1 = 160 ± 11 s and T2 ≈ 20 s. The resulting images of the flowing liquid were of reasonable quality and had an SNR of about 70.

Conclusion: Based on the SNR of the obtained Xe EPI images, it was estimated that rapid *in vivo* MRA with ^{129}Xe may be feasible, provided that an efficient, biologically acceptable carrier for Xe can be found and polarization levels of more than 25% can be achieved in isotopically enriched ^{129}Xe.

Key words: MR angiography, hyperpolarized gas; dissolved xenon-129; echo-planar imaging; experimental.

Correspondence: Sven Månsson, Department of Experimental Research, Malmö University Hospital, SE-205 02 Malmö, Sweden.
FAX +46 40 33 62 07.

Accepted for publication 10 June 2002.

In conventional proton MR imaging, only about 1 ppm of the available nuclei contribute to the observable NMR signal at thermal equilibrium and at clinical magnetic field strengths. However, by using optical pumping methods (5), it is possible to create non-equilibrium polarizations of noble gases (^{3}He and ^{129}Xe) 5–6 orders of magnitude higher than their thermal equilibrium polarization. MR imaging of hyperpolarized gases is thus possible, despite the low spin density (2, 17).

Imaging of hyperpolarized nuclei differs in several respects from traditional proton imaging. Once the hyperpolarized state is created, the longitudinal magnetization will decay towards the thermal equilibrium value with the time constant 1/T1. Typical imaging strategies for utilizing the initial magnetization are therefore to use gradient echo sequences with small radio frequency (RF) flip angles, or sequences which acquire the full *k*-space data after a single RF excitation, such as echo-planar imaging (EPI) (19), rapid acquisition with relaxation enhancement (RARE) (7) or spiral imaging (22). When imaging a low-gamma nucleus like xenon (Xe), attention must be paid to the per-

formance of the gradient system, since the time integral of the imaging gradients must be increased compared to proton imaging.

Although visualization of the respiratory airways and the lungs has been the primary target for the potential clinical use of hyperpolarized gases (13, 15), attempts have been made to assess the usefulness of hyperpolarized gases for other applications. With respect to vascular studies, Xe is soluble in biological tissues and, when inhaled, is taken up into the pulmonary blood. Applications such as functional MR imaging (fMRI) (9) and measurement of cerebral blood flow (20) have been suggested using inhaled hyperpolarized Xe. Various carriers have also been proposed as delivery media for Xe after i.v. injections (6, 21, 24). Injection of such solutions or emulsions of hyperpolarized Xe may be used for fMRI (10), perfusion measurements (6, 14) or MR angiography (MRA) (4).

MRA using hyperpolarized contrast media has the advantage of absence of background signal from surrounding tissues. The lack of background signal improves the contrast-to-noise ratio and may enable reduced field of view without folding artifacts, thereby allowing reduced matrix sizes and correspondingly faster acquisition times. Angiographic imaging using injected hyperpolarized ^{129}Xe has previously been reported (18). This study employed a gradient echo sequence with moderate flip angle and a few seconds' scan time. However, a fast single-shot acquisition technique, like EPI, could potentially improve the result, due to the full utilization of the longitudinal magnetization of the hyperpolarized contrast agent. Ultrafast imaging could furthermore reduce flow and motion artifacts, thereby opening possibilities for imaging of rapidly moving vessels, where conventional proton-based techniques are hampered by object motion and tissue background signal.

The use of hyperpolarized contrast agents for rapid MRA has to date been sparsely investigated and the feasibility of the technique needs further evaluation. It was the aim of the present study to evaluate the potential application of ^{129}Xe as an angiographical contrast agent, using EPI of a flow phantom. From the obtained signal-to-noise ratio (SNR) the efficacy of the EPI sequence was evaluated and predictions and extrapolations to clinical whole-body imaging were performed.

Material and Methods

Xe polarization and handling: ^{129}Xe was polarized with laser optical pumping using a prototype commercial polarizer (IGI 9800, Amersham Health, Durham, NC, USA). A gas mixture of 1% enriched Xe (75% ^{129}Xe), 10% N_2 and 89% ^{4}He flowed at a rate of 1.0 l/min through an optical cell where the ^{129}Xe spins were polarized via spin exchange with optically pumped Rb vapor (5). Hyperpolarized Xe (HpXe) was accumulated for 37 min and frozen at liquid nitrogen temperature. After thawing, the HpXe was collected in a plastic bag (volume 300 ml, Tedlar, Jensen Inert, Coral Springs, FL, USA) at 1 atm pressure. The polarization level in the bag immediately after thawing was measured to 6% using a stand-alone calibration station (Amersham Health). The HpXe bag was transported 40 m from the polarizer to the MR scanner in a transport suitcase (Amersham Health) with a static magnetic field of 0.5 mT. The first HpXe image was acquired 1 h after the polarization measurement. After the last HpXe image, the polarization of the gas remaining in the bag was again measured at the calibration station and the T1 relaxation within the bag was calculated. Using this T1 value, the actual polarization level at each imaging time point could be interpolated.

Dissolving of Xe gas in ethanol: A 60-ml plastic syringe (Plastipak; Becton Dickinson, Drogheda, Ireland) containing 25 ml 95% ethanol was connected to the HpXe bag. The syringe was filled with Xe gas from the bag to a total volume of 60 ml and intensely shaken for 3 s to achieve an equilibrium solution. Thereafter the remaining gas was removed from the syringe. To determine the amount of shaking necessary to reach an equilibrium solution, the concentration of dissolved HpXe was measured after intense shaking of the gas-ethanol mixture, after gentle shaking and without shaking. For determination of the concentration of dissolved HpXe, a syringe containing 50% ethanol volume and 50% HpXe gas volume after shaking was placed in the magnet and NMR spectra were acquired. The dissolved concentration was calculated from the ratio of the areas of the gas peak and the dissolved peak (163 ppm apart) and the known gas concentration at 1 atm pressure.

The T1 and T2 relaxation times of dissolved HpXe were measured in syringes containing only liquid (no gaseous HpXe). T1 relaxation was measured using a train of 16 RF excitations with 12 s interdelay time and a flip angle of 3°. Due to the small flip angle, the apparent relaxation caused by the RF pulses was ignored. The T1 relaxation was measured both with and without removal of solved oxygen from the ethanol, by intense bubbling with helium gas for 5 min, before mixing with HpXe. T2 relaxation was estimated using a Carr-Purcell-Meiboom-Gill (CPMG) multiecho sequence with

128 echoes and an interecho time of 100 ms. The T1 and T2 relaxation times were calculated by fitting of mono-exponential functions to the peaks of the dissolved HpXe spectral line. T2 relaxation was measured without He bubbling.

Flow phantom: A flow phantom was constructed consisting of two thin-walled (0.1 mm) plastic tubes with 6.0-mm inner diameter, inserted into a Plexiglas cylinder with 65-mm diameter (Fig. 1). The Plexiglas cylinder was filled with tap water in order to minimize susceptibility gradients from air-fluid boundaries. The plastic tubes were connected via flexible silicone tubing (5-mm inner diameter) to two glass containers, allowing free, gravity-induced flow of ethanol from the upper to the lower container through the phantom. The phantom was placed horizontally in the magnet. The vertical distance between the two containers was adjusted to give a mean flow velocity of 15 cm/s. The mean velocity was calculated from the measured flow (as measured by stop-watch and measure glass) divided by the cross-section area of the tube.

A 25-ml bolus of hyperpolarized Xe dissolved in ethanol was injected in the flow phantom through a plastic catheter 45 cm upstream from the magnet isocenter. The injection rate was approximately 12 ml/s. To ensure an even mixing of the injection bolus throughout the full diameter of the tube, the catheter was directed upstream relative to the flow direction. Image acquisition was started before the bolus injection and continued for 1 min.

MR imaging and image evaluation: Imaging was performed on a 2.4 T animal imaging system (Biospec 24/30, Bruker Biospin, Ettlingen, Germany) with a maximum gradient strength of 200 mT/m and a gradient rise time of 240 μs. The RF coil was a birdcage resonator double-tuned for ^{1}H and ^{129}Xe (Bruker Biospin). Flow phantom images of HpXe were acquired approximately 20 s after the mixing of HpXe with ethanol, using a single-shot, spin-echo EPI sequence. The readout gradient direction was aligned parallel to the flow direction (Fig. 1). The sequence parameters were: FOV 10×10 cm, matrix 32×32, echo time 32 ms, ADC bandwidth 50 kHz, total scan time 44 ms. The images were acquired without slice-selection gradients. During the bolus passage, images were acquired repeatedly with 1.5 s intervals.

For comparison, imaging was also performed using non-hyperpolarized Xe. A syringe filled with thermally polarized Xe dissolved in ethanol was placed in the magnet and a spin-echo EPI image was acquired with parameters: FOV 24×24 cm, matrix 64×64, echo time 192 ms, ADC bandwidth 25 kHz, without slice gradient. Due to the weak signal from the non-hyperpolarized Xe, the sequence was averaged 64 times with a repetition time of 300 s and a 90° flip-back pulse between each single-shot acquisition.

The time-course of the signal intensities in the flow phantom images was measured as the average signal within a central 1×5 pixel region perpendicular to the inflow and outflow tubes. The SNR of all images was measured as the mean signal within a region of interest (ROI) divided by the noise level σ. σ was estimated using the relation (11)

$$\sigma = \sqrt{\frac{2}{\pi}}\, S_{back} \qquad \text{(Eqn. 1)}$$

where S_{back} is the mean signal within a ROI containing only background noise. For the image of thermal equilibrium Xe, the measured SNR was corrected by the method suggested by Gudbjartsson & Patz (11) for low SNR images:

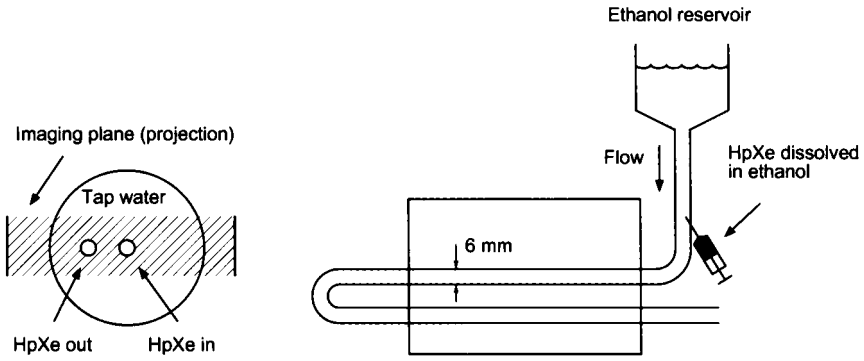

Fig. 1. The flow phantom and image orientation of the echo planar images. In the experiment, no slice selection gradient was used.

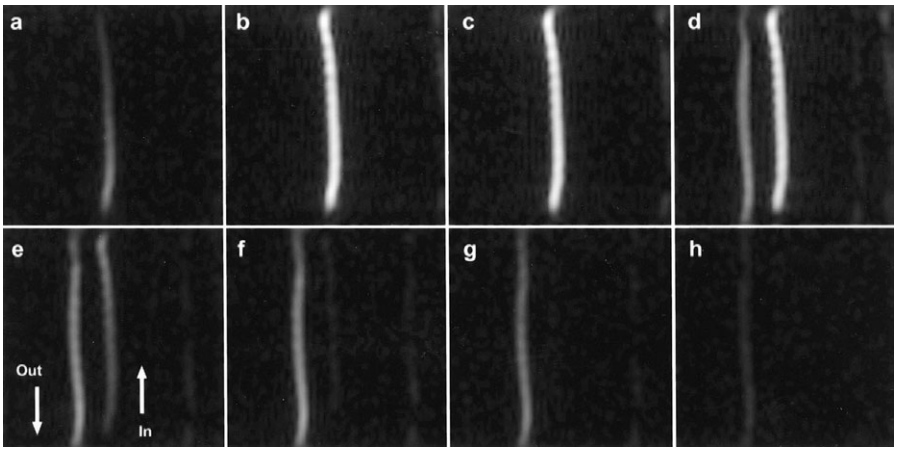

Fig. 2. a–h) EPI images showing a time series of flowing Hp ^{129}Xe, acquired at 1.5-s intervals. The acquisition time of each image was 44 ms. The flow direction is indicated in (e). The mean flow velocity was 15 cm/s and the HpXe polarization level was estimated to 2%.

$$S_{corrected} = \sqrt{|S^2 - \sigma^2|} \quad \text{(Eqn. 2)}$$

where S is the measured signal intensity. Without this correction, the SNR of a noisy image would be overestimated.

To be able to compare the different SNR values, a normalization was made using the following relation (8):

$$SNR \propto cPV_{vox}\sqrt{t_{aq}} \quad \text{(Eqn. 3)}$$

where c is the spin concentration, P is the polarization, V_{vox} is the voxel volume and t_{aq} is the total sampling time. The SNR was normalized to c=1 M, 10 mm^3 voxel volume, 1 s sampling time and P corresponding to thermal equilibrium polarization.

Results

Solution and relaxation properties: After intense shaking for 3 s, the measured Ostwald solubility coefficient (the ratio between dissolved concentration and gas concentration) of Xe in ethanol was 2.8±0.3, corresponding to 87±8 mM ^{129}Xe. Prolonged shaking (10 s) of the gas-ethanol solution did not significantly increase the solubility. With only gentle shaking, or without shaking, the solubility was 1.6±0.3, indicating that an equilibrium solution had not been reached.

The T1 relaxation of HpXe dissolved in ethanol was measured to 55±10 s without He bubbling, and to 160±11 s after He bubbling. The T2 relaxation was measured to 25 s.

Flow phantom images: A series of eight consecutive EPI images with 1.5-s intervals are presented in Fig. 2. The polarization level at the time of imaging was estimated to 2% when considering the T1 relaxations in both the Tedlar bag and the ethanol. The time course of the signal intensities are plotted for the inflow and the outflow tubes (Fig. 3). The delay between the arrival of the inflow and outflow boluses, as defined by the half-maximum intensity in the center of the image, was measured to 3.2 s. The dis-

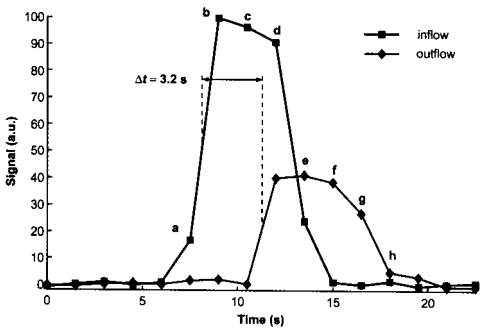

Fig. 3. Time course of the signal intensities in the EPI images of flowing hyperpolarized Xe. The time delay (Δt) of 3.2 s between the arrival of the inflow and outflow boluses corresponds to a mean flow velocity of about 17 cm/s. The letters a–h correspond to the images shown in Fig. 2.

tance traveled by the bolus was about 55 cm, hence the time delay corresponded to a mean flow velocity of 17 cm/s, which was in good agreement with the stop-watch measured flow of 15 cm/s.

The maximum SNR in the flow phantom images was measured to 74. The SNR of the thermally polarized Xe was 3.8 (after correction according to (11)). The normalized SNR values, according to Eqn. 3, were 14 (flow phantom) and 19 (thermal polarization), respectively.

Discussion

In the EPI images of the flowing, hyperpolarized Xe, no severe artifacts related to improper adjustment of the imaging gradients were visible, except a minor ghost in the phase encoding direction ("N/2-ghost"). The slight curvatures of the straight tubes in the flow phantom were caused by B_0-field inhomogeneities. The maximum SNR was measured to 74, and the images were of reasonable quality. The relatively coarse spatial resolution in the experiment (3 mm) was mainly dictated by the performance of the gradient system. From an SNR point of view, an increased spatial resolution would have been possible. The low polarization level during the experiment also leaves room for SNR improvements. When using Xe at thermal equilibrium, an EPI image could only be acquired after extensive averaging. After normalization according to Eqn. 3, the SNR of the hyperpolarized, flowing Xe was about 25% lower than the SNR of the thermal equilibrium, static Xe. A possible explanation for this difference could be flow-induced signal losses, but the normalized SNR values of the hyperpolarized and the non-hyperpolarized images were within the same range and thus indicated that no major, unexpected signal loss had taken place, e.g., during the process of solving the hyperpolarized gas in the ethanol. Neither did the experiments where the Ostwald solubility coefficient of HpXe in ethanol was investigated indicate any such polarization losses.

The Ostwald solubility coefficient of Xe in ethanol, as measured via the NMR procedure in the present study, agreed reasonably well with reported measurements of Ostwald solubility coefficients using radiographic methods (12), where the solubility was 2.47 ± 0.02. The measured T1 and T2 relaxation times of hyperpolarized Xe in ethanol are 1–2 orders of magnitude longer than the proton relaxation times within the body. Long relaxation times are essential for preserving the magnetization from the injection site to the target organ, but also for permitting fast, single-shot techniques, like the EPI sequence. Without a suitable carrier agent, the relaxation times of Xe in blood is short (T1 of 3–10 s depending on the oxygenation level (1), T2 of 2–7 ms) (23). When using lipid emulsion as a carrier, however, the relaxation times may be prolonged (T1 of 25 s, T2* of 37 ms) (18).

Taking the normalized SNR from the EPI images of flowing HpXe as a starting point, the SNR can be predicted for various scenarios. In our experiments, the polarization level during imaging was approximately 2%. With further developments of the optical pumping techniques, and by minimizing the delay between the dispensing of hyperpolarized gas and injection of HpXe, polarization levels of at least 25% can be expected for the injection solution (5). The concentration of HpXe after i.v. injection is more difficult to estimate because the bolus will be diluted by the ratio between the cardiac output and the injection rate (16). Furthermore, when passing the heart, a mixing of the Xe carrier with blood will occur, which has both a shorter T1 (3) and a lower solubility for Xe than the carrier. As a first approximation, one may consider the case of injecting a bolus with 25% polarization of enriched ^{129}Xe, and ignore relaxation and dilution of the bolus after injection.

The Ostwald solubility coefficient of Xe in, for example, perfluorcarbons is 1.2 (24), i.e., half of the solubility in ethanol. The bolus concentration would therefore be about 40 mM. Assuming the bolus being imaged with a scanner capable of gradient strengths of about 40 mT/m, it should be possible to acquire 64×64 matrix EPI images with $2 \times 2\,mm^2$ in-plane resolution within 70–80 ms. Based on the measured SNR from our experiments, we estimate that the SNR of such an image would result in usable angiograms (SNR about 20). This estimation is based on the assumptions that: a) Xe can be polarized to levels of at least 25%; b) isotopically enriched ^{129}Xe is used; c) the vessel diameters are >2 mm; and d) the Xe is solved in a carrier with a solubility of 1.2 or better. Admittedly, bolus dilution and polarization loss due to T1 relaxation after injection will diminish SNR and thus call for further increased polarization levels, and/or decreased spatial and temporal image resolution. Clearly, the usefulness of HpXe and the single-shot EPI technique as demonstrated in this work, will depend on whether biocompatible carriers with long relaxation times are available.

Conclusions: Using EPI acquisition, our experiments demonstrated that HpXe MRA images with 32×32 matrix could be acquired with $3 \times 3\,mm^2$ in-plane resolution in less than 50 ms. Despite the modest polarization level ($<3\%$) used in the present study, the image SNR was high (>70). Al-

though several technical issues remain to be improved, the experiments hold promise for the future use of HpXe as an MRA contrast agent in combination with ultrafast imaging for studies of, e.g., vessels subjected to internal motion.

REFERENCES

1. Albert M. S., Balamore D., Kacher D. F., Venkatesh A. K. & Jolesz F. A.: Hyperpolarized ^{129}Xe T1 in oxygenated and deoxygenated blood. NMR Biomed. 13 (2000), 407.
2. Albert M. S., Cates G. D., Driehuys B. et al.: Biological magnetic resonance imaging using laser-polarized ^{129}Xe. Nature 370 (1994), 199.
3. Albert M. S., Schepkin V. D. & Budinger T. F.: Measurement of ^{129}Xe T1 in blood to explore the feasibility of hyperpolarized ^{129}Xe MRI. J. Comput. Assist. Tomogr. 19 (1995), 975.
4. Chawla M. S., Chen X. J., Cofer G. P. et al.: Hyperpolarized ^{3}He microspheres as a novel vascular signal source for MRI. Magn. Reson. Med. 43 (2000), 440.
5. Driehuys B., Cates G. D., Miron E., Sauer K., Walter D. K. & Happer W.: High-volume production of laser-polarized ^{129}Xe. Appl. Phys. Lett. 69 (1996), 1668.
6. Duhamel G., Choquet P., Leviel J. L. et al.: *In vivo* ^{129}Xe NMR in rat brain during intra-arterial injection of hyperpolarized ^{129}Xe dissolved in a lipid emulsion. C. R. Acad. Sci. III 323 (2000), 529.
7. Durand E., Guillot G., Darrasse L. et al.: CPMG measurements and ultrafast imaging in human lungs with hyperpolarized helium-3 at low field (0.1 T). Magn. Reson. Med. 47 (2002), 75.
8. Edelstein W. A., Glover G. H., Hardy C. J. & Redington R. W.: The intrinsic signal-to-noise ratio in NMR imaging. Magn. Reson. Med. 3 (1986), 604.
9. Gao J. H., Lemen L., Xiong J., Patyal B. & Fox P. T.: Magnetization and diffusion effects in NMR imaging of hyperpolarized substances. Magn. Reson. Med. 37 (1997), 153.
10. Goodson B. M., Song Y., Taylor R. E. et al.: *In vivo* NMR and MRI using injection delivery of laser-polarized xenon. Proc. Natl. Acad. Sci. USA 94 (1997), 14725.
11. Gudbjartsson H. & Patz S.: The Rician distribution of noisy MRI data. Magn. Reson. Med. 34 (1995), 910.
12. Himm J. F.: The solubility of xenon in simple organic solvents and in aqueous amino acid solutions. Thesis, Michigan State University 1986.
13. Kauczor H. U., Hofmann D., Kreitner K. F. et al.: Normal and abnormal pulmonary ventilation. Visualization at hyperpolarized He-3 MR imaging. Radiology 201 (1996), 564.
14. Lavini C., Payne G. S., Leach M. O. & Bifone A.: Intravenous delivery of hyperpolarized ^{129}Xe. A compartmental model. NMR Biomed. 13 (2000), 238.
15. Macfall J. R., Charles H. C., Black R. D. et al.: Human lung air spaces. Potential for MR imaging with hyperpolarized He-3. Radiology 200 (1996), 553.
16. Maki J. H., Chenevert T. L. & Prince M. R.: Three-dimensional contrast-enhanced MR angiography. Top. Magn. Reson. Imaging 8 (1996), 322.
17. Middleton H., Black R. D., Saam B. et al.: MR imaging with hyperpolarized ^{3}He gas. Magn. Reson. Med. 33 (1995), 271.
18. Möller H. E., Chawla M. S., Chen X. J. et al.: Magnetic resonance angiography with hyperpolarized ^{129}Xe dissolved in a lipid emulsion. Magn. Reson. Med. 41 (1999), 1058.
19. Saam B., Yablonskiy D. A., Gierada D. S. & Conradi M. S.: Rapid imaging of hyperpolarized gas using EPI. Magn. Reson. Med. 42 (1999), 507.
20. Swanson S. D., Rosen M. S., Agranoff B. W., Coulter K. P., Welsh R. C. & Chupp T. E.: Brain MRI with laser-polarized ^{129}Xe. Magn. Reson. Med. 38 (1997), 695.
21. Venkatesh A. K., Zhao L., Balamore D., Jolesz F. A. & Albert M. S.: Evaluation of carrier agents for hyperpolarized xenon MRI. NMR Biomed. 13 (2000), 245.
22. Viallon M., Berthezene Y., Callot V. et al.: Dynamic imaging of hyperpolarized ^{3}He distribution in rat lungs using interleaved-spiral scans. NMR Biomed. 13 (2000), 207.
23. Wilson G. J., Santyr G. E., Anderson M. E. & Deluca P. M. Jr: T2 of ^{129}Xe in rat tissue homogenates and blood at 9.4 T. Proc. Ann. Meeting ISMRM 1999, p. 2102.
24. Wolber J., Rowland I. J., Leach M. O. & Bifone A.: Perfluorocarbon emulsions as intravenous delivery media for hyperpolarized xenon. Magn. Reson. Med. 41 (1999), 442.

Paper II

Hyperpolarized ^{13}C MR angiography using trueFISP

Jonas Svensson[1*], Sven Månsson[2], Edvin Johansson[3],
J. Stefan Petersson[4], Lars E. Olsson[1]

[1] Dept. of Radiation Physics, Malmö University Hospital, Sweden
[2] Dept. of Experimental Research, Malmö University Hospital, Sweden
[3] Dept. of Radiation Physics, Lund University Hospital, Sweden
[4] Amersham Health R&D, Medeon, Malmö, Sweden

[*]Correspondence to:

Jonas Svensson
Department of Radiation Physics
Malmö University Hospital
SE–205 02 Malmö, Sweden
Telephone: +46 (0)40 33 31 59, Telefax: +46 (0)40 96 31 85
E-mail: jonas.svensson@rfa.mas.lu.se

Abstract

A ^{13}C-enriched water-soluble molecule, bis-1,1-(hydroxymethyl)-1-^{13}C-cyclopropane-D_8 with ^{13}C concentration ~200 mM, was hyperpolarized to ~15% using dynamic nuclear polarization, and was used as a contrast medium (CM) for contrast-enhanced magnetic resonance angiography. MR angiograms with high signal-to-noise ratio (SNR) were acquired after injection of the CM in live rats.

The long relaxation times of the CM (*in vitro*: $T_1 \approx 82$ s, $T_2 \approx 18$ s, *in vivo*: $T_1 \approx 40$ s, $T_2 \approx 2$ s) were utilized with a trueFISP pulse sequence. It was shown both theoretically and experimentally that the optimal flip angle was 180°. Contrast-enhanced MR angiography was performed in four anaesthetized live rats after intravenous injection of 3 ml of the CM. In two animals, the angiograms covered the thoracic/abdominal region and in the two others, the head-neck region was covered. Fifteen consecutive images were acquired in each experiment with a flip-back pulse at the end of each image acquisition.

In the angiograms, the *vena cava* (SNR ≈ 240), the aorta, the renal arteries, the carotid arteries (SNR ≈ 75), the jugular veins, and several other vessels were visible. The cardiac and pulmonary regions were highly enhanced (SNR in the heart ≈ 500). Magnetization was preserved from one image acquisition to the next with the flip-back technique (SNR in the heart ≈10 in the 15th image).

Keywords: ^{13}C, hyperpolarized, angiography, contrast medium.

Introduction

The most widespread technique for MR angiography (MRA) today is to use an intravenous injection of a T_1-shortening contrast medium (CM) in combination with T_1-weighted pulse sequences (1, 2). The imaging times for this contrast-enhanced (CE) MRA technique is substantially shortened as compared with techniques such as time-of-flight and phase contrast, and it is relatively insensitive to variations in blood flow velocity. CE-MRA has consequently increased the clinical impact of MRA. An interesting possibility to further increase the signal-to-noise ratios (SNR) and contrast-to-noise ratios (CNR) in CE-MRA would be to use a hyperpolarized (HP) contrast medium.

It has been demonstrated that certain noble gases (^{3}He, ^{129}Xe) can be hyperpolarized to a much higher level (> 10%) than that of thermal polarization of ^{1}H at clinical magnetic fields (~0.0005%). This high degree of polarization compensates for the low spin density of the gases *in vivo*, and they (mostly ^{3}He) have been used to image airways and lungs (3–5). HP ^{3}He and ^{129}Xe have also been proposed for vascular imaging. Helium has low solubility in blood, but it can be delivered to the vascular system using encapsulation techniques (6–9). Xenon, on the other hand, is directly soluble in blood, and inhalation of the gas is one possibility to administer HP Xenon in the human vascular system (10–12). Xenon can also be dissolved in a biocompatible carrier (13–16) to be delivered through intravenous injection. However, even if the hyperpolarized gases could be efficiently administered to the blood, the inherently low concentration of a gas makes ^{3}He and ^{129}Xe unsuitable as CM for CE-MRA.

A high vascular concentration of a hyperpolarized CM can be obtained if ^{13}C as part of a water-soluble molecule is polarized, instead of ^{129}Xe and ^{3}He. Earlier, we have presented two different techniques for hyperpolarizing ^{13}C in such molecules and used them for imaging. These polarization techniques are different from the ones used to hyperpolarize noble gases, and are 1) parahydrogen-induced polarization (PHIP) (17) and 2) dynamic nuclear polarization (DNP) (18). The method used in this paper, DNP, has been used earlier to improve the sensitivity of *in vitro* NMR (19) and for the production of polarized targets in neutron scattering experiments (20). The molecule used here can currently be polarized to ~15% with a concentration of 200 mM in water. The high degree of polarization, together with the high

concentration, makes this substance promising as an MRA contrast medium.

Imaging of HP spins requires a different pulse sequence approach than conventional MR imaging with thermally polarized ^{1}H. For noble gas imaging, a fast low angle shot (FLASH) pulse sequence with small flip angle excitations is commonly used. A small fraction of the hyperpolarized non-renewable longitudinal magnetization is then utilized in each phase-encoding step and remaining transverse magnetization is spoiled between each excitation. Consequently, the FLASH sequence does not take advantage of long T_2 relaxation times. A better utilization of the available magnetization is obtained if the transverse magnetization is recycled from one repetition to the next, known in the literature as steady-state free precession (SSFP). In this paper one such SSFP sequence is studied — the true fast imaging with steady-state precession (trueFISP), also called balanced fast field echo (FFE) — together with a CM having long ^{13}C relaxation times. With this technique, the long T_2 can be utilized, and images with a much higher SNR than is possible with a FLASH type pulse sequence can be acquired (21). The existing signal expressions used for description of the trueFISP pulse sequence are not applicable for the imaging of HP spins, since imaging must take place during a HP non-equilibrium state of the magnetization. However, if the relaxation times of the spins are long compared with the time scale of the imaging, it is still possible to use the trueFISP pulse sequence.

The aim of this study was to use a HP ^{13}C-based substance as a CM for obtaining MR angiograms with high SNR. The angiograms were obtained after intravenous injection of the CM in live, anesthetized rats. A trueFISP pulse sequence was chosen to utilize the long T_2 of the CM. The behavior of the pulse sequence for imaging of HP spins was evaluated.

Theory

Using trueFISP for imaging of hyperpolarized spins

As described by Oppelt *et al.* (22), the trueFISP pulse sequence (originally called FISP) has fully balanced gradient moments and alternating +/– θ excitation pulses. The gradient scheme is symmetric over a repetition time (TR), and the time of the echo (TE) is equal to TR/2.

The evolution of the magnetization for a short TR pulse sequence is usually rather complex. In the trueFISP pulse sequence, however, the balancing

of the gradient moments prior to each excitation pulse ideally yields zero dephasing over a TR, and no higher order echoes will be created (23). Hence, if dephasing effects can be neglected (which apart from gradient balancing also requires a very homogeneous static magnetic field and/or very short TR), the magnetization can be described by one single magnetization vector M. The evolution of M is easily followed during a pulse train of alternating RF pulses. For thermally polarized spins, the longitudinal magnetization is recovering through T_1 relaxation between each RF pulse, and M will oscillate towards a coherent steady state with increasing number of RF pulses. The oscillation is greatly reduced if the pulse train starts with a $\theta/2$-pulse (Figure 1) (24). For HP spins, however, the effect of T_1 relaxation is the opposite, and instead of reaching a steady state, the magnetization eventually decays to the thermal equilibrium value (Figure 1).

This requires a different acquisition approach when imaging HP spins. In general, it is preferable to acquire the image during steady state, because signal modulations during *k*-space encoding may result in image artifacts (25, 26). However, if the HP spins have long relaxation times when compared with the acquisition time, the signal variation during the approach to steady state (i.e., virtually zero) will be small as long as the $\theta/2$ pre-pulse is used. Therefore, it is possible to acquire the image during this "pseudo steady state" without risk of severe artifacts.

The existing signal equation for trueFISP (22) is only valid for thermally polarized spins at steady state. An expression valid for a signal acquired from HP spins before the steady state is reached must include the number of RF pulses experienced by the spins. The derivation of such an equation is performed below, for on-resonance spins:

The magnitude $|\boldsymbol{M}_n|$ of the magnetization vector after the n-th θ pulse can be described by its components M_y and M_z:

$$\left|\boldsymbol{M}_n\right| = \left(M_{z,n}^2 + M_{y,n}^2\right)^{1/2}. \qquad [1]$$

The RF pulses, having alternating phase, flip the magnetization back and forth an angle $\pm\,\theta$. If the relaxation times are long as compared with the imaging time, the angle of $\boldsymbol{M}$ is approximately constant and equal to $\theta/2$, relative to the direction of the static magnetic field. Then, the components of $\boldsymbol{M_n}$ decay by $E_1 = \exp(-\mathrm{TR}/T_1)$ and $E_2 = \exp(-\mathrm{TR}/T_2)$ from one RF pulse to the next:

$$M_{z,n} = E_1 M_{z,n-1}$$
$$M_{y,n} = E_2 M_{y,n-1} \,. \qquad [2]$$

Insertion of Eq. [2], together with $M_{z,n} = |\boldsymbol{M}_n| \cos(\theta/2)$ and $M_{y,n} = |\boldsymbol{M}_n| \sin(\theta/2)$, into Eq. [1] yields:

$$M_{y,n} = \sin\frac{\theta}{2}\left(\left(E_1 |\boldsymbol{M}_{n-1}| \cos\frac{\theta}{2}\right)^2 + \left(E_2 |\boldsymbol{M}_{n-1}| \sin\frac{\theta}{2}\right)^2\right)^{1/2}. \qquad [3]$$

By using the principle of induction and assuming that the initially available magnetization is $M_{z,0}$, Eq. [3] may be rewritten according to:

$$M_{y,n} = M_{z,0} \sin\frac{\theta}{2}\left(\left(E_1 \cos\frac{\theta}{2}\right)^2 + \left(E_2 \sin\frac{\theta}{2}\right)^2\right)^{n/2}. \qquad [4]$$

With finite relaxation times, the angle of $\boldsymbol{M}$ will differ slightly from $\theta/2$, which will introduce an error in Eq. [4], increasing with increasing n. With a TR of 3.6 ms (as used in the experiments), this error after 256 RF pulses is < 2% for T_2 values above 200 ms.

The signal in the reconstructed image is proportional to the signal in the central *k*-space line. If linear phase-encoding is used with m encoding steps, the signal from the HP spins in the image is thus found by evaluating Eq. [4] for $M_{y,m/2}$. If T_1 and T_2 are large as compared with $n \cdot$TR, the expression can be approximated by $M_{y,n} = M_{z,0} \sin(\theta/2)$, yielding an optimal flip angle of 180°. This can be compared with the optimal flip angle in the thermal steady-state signal expression for trueFISP (22), which is always ≤ 90°.

It is of interest to compare the signal obtained from a trueFISP pulse sequence with the corresponding signal from a FLASH pulse sequence, in which all transverse magnetization is assumed as being spoiled prior to each RF pulse: immediately after the n-th RF pulse, the available longitudinal magnetization is described by $M_{z,n} = E_1 M_{z,n-1} \cos\theta$, and $\tan\theta = M_{y,n} / M_{z,n}$. This leads to the signal equation for the FLASH pulse sequence in the case of HP spins:

$$M_{y,n} = M_{z,0} \sin\theta \left(E_1 \cos\theta\right)^{n-1}. \qquad [5]$$

Methods

Polarization procedure

The contrast medium used in the present work combines a high concentration of the NMR active nucleus with a high degree of polarization and long relaxation times. The molecule used as a contrast agent, bis-1,1-(hydroxymethyl)-1-^{13}C-cyclopropane-D_8, is a compound with good properties for the DNP polarization method. It is highly soluble in water, has a low toxicity, and it is biologically stable on the time scale of the imaging experiment. Long relaxation times of the single ^{13}C nucleus are obtained, owing to the molecular structure and the deuteration.

The paramagnetic agent needed for the DNP process, the triarylmethyl-radical tris (8-carboxy-2,2,6,6-tetra-(hydroethyl)benzo[1,2-d:4,5-d′]-bis(1,3)dithiole-4-yl) methyl sodium salt (27), dissolves readily at a concentration of 15 mM in the contrast agent. Beads of 1–2-mm diameters were made from this solution by forming droplets that were frozen in liquid nitrogen. Approximately 100 mg was transferred into a small cup under liquid nitrogen. The cup had been made from thin-walled, 0.1-mm, Kel-F and was placed in a long Teflon tube. The Teflon tube was inserted into a pumped helium bath (1.3 K) and a magnetic field of 3.35 T. The sample was irradiated for a time of at least one hour (polarization time constant approx. 3600 s) at a microwave frequency of 93.925 GHz. The ^{13}C nuclear polarization thereby approached 20% in the solid state through the thermal mixing effect. When the solid sample had been polarized, it was raised approximately 10 cm from the magnetic center out of the liquid helium bath, while still in high magnetic field and cold helium gas. A Teflon stick then tightly embraced the sample cup. The Teflon stick had two thin Teflon tubes at the center allowing hot water (~95° C) to be injected into the sample cup and the dissolved material to leave the cup and fill a syringe with 3–5 ml of the HP solution. In the syringe, the concentration of the contrast agent was approx. 200 mM, with a polarization of approx. 15%. The concentration of the paramagnetic agent was 0.1 mM. The temperature and pH of the solution were ~37° C and ~7, respectively.

MR scanner and pulse sequences

All imaging experiments were performed using a 2.35 T animal MR scanner (Biospec 24/30, Bruker Biospin, Ettlingen, Germany). A ^{13}C/^{1}H double-tuned birdcage coil was used.

A trueFISP pulse sequence was implemented on the scanner (TE/TR = 1.8/3.6 ms, BW = 80 kHz, FOV = 70×70 mm^2 and matrix = 64×64, read oversampling was used). All images were acquired as projection images without a slice gradient.

A $\theta/2$ pre-pulse pulse was applied at a time TR/2 before the first θ pulse, as described in the theory section. At a time TR/2 after the last θ pulse in each image acquisition, a $\theta/2$ flip-back pulse was applied in order to store the magnetization in the longitudinal direction for further imaging. Following the flip-back pulse, a spoiling gradient was applied to destroy any remaining transverse magnetization. Images could be acquired consecutively, separated in time by an arbitrary time gap.

For comparison, a standard FLASH pulse sequence was also used in the phantom experiments. The parameters of this sequence were TE/TR = 1.8/15 ms, BW = 80 kHz, matrix = 64×64 (read oversampling was used) and FOV = 70×70 mm^2. No slice selection was used.

In vitro *experiments*

Eight polarizations were used to determine the flip angle dependence of the trueFISP pulse sequence. The contrast medium from each polarization was dissolved in water to 20 ml (concentration $\approx$ 40 mM) and evenly distributed to five 5-ml syringes. The syringes were then imaged one at a time using the trueFISP pulse sequence. The duration between the injection of hot water to dissolve the frozen CM and the first image acquisition was about 0.5 min. The first and the last syringe in each polarization batch were always imaged with the same flip angle ($\theta = 70°$). These images were used for estimation of the T_1 of the contrast medium by assuming a mono-exponential T_1 decay between the two acquisitions. The other three acquisitions from each batch were acquired with flip angles ranging from 10° to 180°. The SNR in the images were evaluated by dividing the signal mean in a region of interest (ROI) over the syringe by the signal mean in a ROI over an area containing only noise. For each batch, the SNR in the images were corrected for T_1 decay. To compensate for differences in polarization between the different batches, the measured SNR from the different batches were also normalized using the acquisition with $\theta = 70°$. For comparison, two polarizations were used to acquire corresponding SNR values with the FLASH pulse sequence.

Two experiments were performed for validation of the flip-back concept and for estimation of the T_2 of the substance in water. Immediately after each polarization, a syringe was filled with 5 ml of the CM, and 15 con-

secutive trueFISP images were acquired using $\theta = 180°$. The time gap (end of one image to start of next) between two images was approximately 20 ms. In the first experiment the phase-encoding gradients were turned off, and the efficacy of the flip-back pulse was studied by observing the signal drop during acquisition. In the second experiment, the phase encoding was turned on, and an approximate T_2 value was calculated by fitting a mono-exponential function to the signal in a large ROI placed over the syringe in each image.

In vivo *experiments*

A series of *in vivo* experiments were performed using four male Wistar rats (280–440 g). All the experiments were approved by the local ethical committee (*Malmö/Lunds djurförsöksetiska nämnd;* appl. no. M1–01). The animals were anaesthetized with a mixture of tiletamine/zolazepam (Zoletil® 50 vet., Boehringer Ingelheim, Copenhagen, Denmark) and xylazine (Rompun® vet., Bayer, Leverkusen, Germany). In all the experiments 3–3.5 ml of the hyperpolarized ^{13}C-based CM (concentration ~200 mM, dissolved in water) was manually injected in the tail vein of the animal with an injection rate of approximately 0.5 ml/s. Image acquisition started immediately after the end of the injection. The trueFISP pulse sequence described above was used in all the experiments. The flip angle was set to 180°. Using the flip-back concept, a series of 15 consecutive images was acquired, with a time gap of 20 ms. Two animals were imaged with a FOV covering the thoracic and the abdominal region. The other two animals were imaged with the FOV covering the head-neck area.

The images were evaluated by means of SNR calculated from the mean signal in a ROI in the first image, divided by the mean noise value in an ROI drawn outside the animal in the last image of the series. The last image has a greatly reduced ^{13}C signal as compared with the first image and was chosen for the noise measurement to minimize signal contamination from image artifacts.

To estimate the T_2 of the ^{13}C-based CM *in vivo*, the total signal in a large ROI covering the whole image was measured in all images of the series covering the abdomen. The *in vivo* T_1 value had been measured to be 38 s in separate experiments (28).

Results

In vitro *experiments*

The T_1 for the ^{13}C substance in water was estimated at 82 ± 6 s (mean result from eight polarization batches). The experiment with 15 consecutively acquired images without phase encoding showed that the flip-back pulse preserves the magnetization from one image to the next (Figure 2). From the corresponding experiment with phase encoding turned on (Figure 3), the apparent T_2 was estimated at 18 s. The relaxation times were put into Eq. [4]. The outer parenthesis in Eq. [4] then becomes close to 1, and with $n = 64/2$, the expression in practice reduces to $\sin(\theta/2)$. The signal thus increases with increasing flip angle, with a maximum at 180° (Figure 4). The measured signal values agree well with the predicted theoretical values.

For the corresponding FLASH sequence, the optimal flip angle is much smaller, approximately 10° (Figure 4). For flip angles larger than 30° the signal is practically zero. With the present sequence parameters, the maximum achievable signal from the two sequences theoretically differs by a factor of nine. This was also was confirmed experimentally.

In vivo *experiments*

The vena cava, aortic arc, lower part of the carotid arteries, aorta and renal arteries were visible in the first angiogram of a series of 15 images covering the thoracic and abdominal area (Figure 5a). SNR in the *vena cava* was 240. The cardiac and pulmonary areas were also highly enhanced, with an SNR in the cardiac region of 490. Using the flip-back concept, it was possible to preserve signal from one image acquisition to the next. Figure 5b shows the fourth image of the series, and SNR in the cardiac region and the *vena cava,* respectively, was 260 and 85. In the 15th and last image, the corresponding cardiac SNR value was 13. In the equally acquired image series of the second animal, the cardiac SNR values in the first and last image were 540 and 9.

Some minor image artifacts were visible in the phase-encoding direction around the cardiac region. These artifacts probably originate from the pulsatile and complex flow of the CM in the heart. However, due to the short TE and TR of the pulse sequence, these effects were small.

To estimate the T_2 of the ^{13}C-based CM *in vivo*, the total signal in a large ROI covering the whole image was measured in all the images of the first series (Figure 3). The signal drop in this *in vivo* situation is due to T_2, but

also to several other sources such as flow and motion. A "worst-case" T_2 value can still be calculated, and from the signal decay in Figure 3 it was estimated at 1.3 s.

In the angiograms covering the head-neck area, the common carotid arteries and the external jugular veins, along with several other vessels, are clearly discernible (Figure 6). From a small signal ROI positioned in the upper part of each carotid, SNR was calculated to be 74 and 76, respectively. Apart from the vascular enhancement, tissues outside the main vessels are also enhanced, indicating that the CM leaks to the extravascular space.

Discussion

We have demonstrated that it is possible to hyperpolarize ^{13}C as part of a water-soluble molecule and use it as a contrast medium for contrast-enhanced MR angiography. The high polarization level, together with the high concentration of the substance, made it possible to acquire angiograms with a high SNR (SNR $\approx$ 500 in the cardiac region) after intravenous injection in live rats.

The long relaxation times of the CM were utilized with a trueFISP pulse sequence. The use of a trueFISP pulse sequence for imaging HP spins differs from imaging thermally polarized spins. Imaging must be performed before a steady state is reached, and it is therefore favorable to use flip angles larger than 90° if the T_2 of the HP substance to be imaged is long. It was shown that the maximum achievable signal from the trueFISP pulse sequence with the current parameters and for the current HP ^{13}C-based CM was a factor nine higher than the maximum achievable signal from a corresponding FLASH pulse sequence (both sequences using linear phase-encoding order).

The signal decay during image acquisition is a function of both T_1 and T_2 relaxation (Eq. [4]). For small flip angles the magnetization is mostly directed longitudinally, and signal decay is dominated by T_1 relaxation. For larger flip angles the T_2 relaxation time is the dominating source of signal decay. The optimal flip angle depends on both the relaxation times and the number of RF pulses. For long T_2 relaxation times and short acquisition times, as in the experiments performed here, the optimal flip angle is close to 180°. If longer acquisition times are to be used (e.g., for 3D imaging) or if it is important to keep a uniform signal over several image acquisitions, it is preferable to use a smaller flip angle, because the slower T_1 relaxation preserves magnetization better than the faster T_2 relaxation.

The T_2 of the ^{13}C-based CM is very long. In this study, the apparent T_2 relaxation time was estimated at 18 s in water and 1.3 s *in vivo* in rats. Previously, the T_2 relaxation has been measured *in vitro* to be approximately 4 s in human blood (28). The apparent T_2 relaxation time is composed not only of pure T_2 relaxation, but it also contains signal losses from other sources, including non-perfect flip-back of the magnetization between images. As shown in the *in vitro* experiment (Figure 2), these losses were, however, small. The trueFISP pulse sequence relies on preserved phase coherence from one pulse to the next, and all effects the causing a non-perfect phase rewinding degrade the signal. One such effect is spins being off resonance. We believe this to be the cause of the weak signal oscillation seen in Figure 2. Another effect is flow/motion. However, the pulse sequence design is such that the complete balancing of the readout gradient makes it first-order flow-compensating over a whole TR. Even though the sequence is not flow compensated at the center of the echo (i.e., at TE), a constant flow in the readout direction will be properly rewound before the next pulse, and will not disturb the phase coherence. The same is true of the slice selection gradient, if it is used. In the experiments performed here, the images were acquired as projection images without slice-selection gradients. The phase-encoding gradients, on the other hand, are not flow compensated. All kinds of flow/motion in the phase-encoding direction, together with flow of higher orders in the readout direction, could therefore cause dephasing problems and signal degradation.

The trueFISP pulse sequence is normally very sensitive to magnetic field inhomogeneities. The net dephasing over one TR due to field inhomogeneity is proportional to the gyromagnetic ratio, γ, of the nucleus being imaged. Because $\gamma_{^{13}C}/\gamma_{^{1}H} \approx 1/4$, these effects are reduced by the same factor for ^{13}C compared with ^{1}H. Furthermore, if the trueFISP pulse sequence is used with $\theta = 180°$, starting with a $\theta/2$ prepulse, it becomes similar to a single-shot rapid acquisition with relaxation enhancement (RARE) pulse sequence (29). RARE is not sensitive to field inhomogeneities, and accordingly the use of a 180° flip angle in the trueFISP pulse sequence makes it behave similar to the RARE sequence in this respect. A different behavior of the trueFISP and the RARE sequences can be expected for moving spins, though, due to the different gradient scheme, as discussed above.

To minimize any kind of dephasing effects, it is important to keep the TR of the pulse sequence short. The gradient strength needed to generate an image with a certain FOV for a given TR is dependent on the nuclei being imaged — the lower the γ, the stronger gradients needed. Hence, even if the

low γ of ^{13}C reduces the sensitivity to field inhomogeneities, it could also prolong the shortest usable TR or increase the smallest possible FOV.

The specific absorption rate (SAR) could limit the use of large flip angles clinically. Large flip angles, together with short TR, lead to a large RF deposition that could exceed allowed SAR levels. One way to reduce such problems is to simply use smaller flip angles. Another way could be to acquire several echoes between each excitation pulse (30).

The obtainable SNR from the hyperpolarized ^{13}C CM can be compared with what is currently possible with conventional ^{1}H-based techniques. The product of the polarization degree, the concentration, and the gyromagnetic ratio of the nucleus used gives an indication of the achievable SNR during a given imaging sequence. The present ^{13}C-based CM can routinely be polarized to about 15%, and the γ of ^{13}C is $\approx$10.7 MHz T^{-1}. Assuming a vascular CM concentration of 10 mM in the vessel of interest after intravenous injection in a patient, and that polarization losses are small between injection and imaging, this product will be the same order of magnitude as for fully relaxed blood in a 1.5 T clinical scanner (polarization $\approx 5 \cdot 10^{-6}$, ^{1}H concentration $\approx$ 80 M, and $\gamma \approx$ 42.6 MHz T^{-1}). It is also likely that the polarization process can be developed further so that the polarization and the concentration of the ^{13}C-based CM is increased enough to yield an additional improvement of the SNR by at least one order of magnitude.

Another important difference between ^{1}H imaging and imaging of hyperpolarized nuclei is the dramatic increase in CNR. Signal will only be present where the CM is present, and as long as it stays in the vascular space, enhancement of surrounding tissue will be minimal. This could be utilized for simplified image protocols. For example, the 2D projection images acquired here are similar to a single view of the maximum intensity projection (MIP) angiograms commonly used in ^{1}H CE-MRA. The difference is that these 2D images are acquired very fast, whereas in ^{1}H imaging a time consuming 3D acquisition followed by MIP reconstruction is required. In the former case however, information from multiple view angles will not be available.

This study focused on using HP ^{13}C as a contrast medium for MR angiography. Another challenging task would be to use HP ^{13}C for perfusion studies. The simple relationship between signal and tracer concentration makes HP ^{13}C promising for quantification purposes.

Conclusion

MR angiograms with high SNR were obtained in live rats after intravenous injection of a hyperpolarized ^{13}C-based contrast medium. The long relaxation times of the CM was utilized with a trueFISP pulse sequence, and with the current sequence parameters it was possible to gain a factor nine in signal as compared with the maximum obtainable signal from a corresponding FLASH sequence. This new class of CM may add value to conventional contrast-enhanced MR angiography.

References

1. Maki JH, Chenevert TL, Prince MR. Three-dimensional contrast-enhanced MR angiography. *Top Magn Reson Imaging* 1996;8:322–344.
2. Prince MR, Yucel EK, Kaufman JA, Harrison DC, Geller SC. Dynamic gadolinium-enhanced three-dimensional abdominal MR arteriography. *J Magn Reson Imaging* 1993;3:877–881.
3. MacFall JR, Charles HC, Black RD, Middleton H, Swartz JC, Saam B, Driehuys B, Erickson C, Happer W, Cates GD, Johnson GA, Ravin CE. Human lung air spaces: potential for MR imaging with hyperpolarized He-3. *Radiology* 1996;200:553–558.
4. Salerno M, Altes TA, Mugler JP 3, Nakatsu M, Hatabu H, de Lange EE. Hyperpolarized noble gas MR imaging of the lung: potential clinical applications. *Eur J Radiol* 2001;40:33–44.
5. Salerno M, de Lange EE, Altes TA, Truwit JD, Brookeman JR, Mugler JP 3. Emphysema: hyperpolarized helium-3 diffusion MR imaging of the lungs compared with spirometric indexes—initial experience. *Radiology* 2002;222:252–260.
6. Callot V, Canet E, Brochot J, Berthezene Y, Viallon M, Humblot H, Briguet A, Tournier H, Cremillieux Y. Vascular and perfusion imaging using encapsulated laser-polarized helium. *MAGMA* 2001;12:16–22.
7. Callot V, Canet E, Brochot J, Viallon M, Humblot H, Briguet A, Tournier H, Cremillieux Y. MR perfusion imaging using encapsulated laser-polarized ^{3}He. *Magn Reson Med* 2001;46:535–540.
8. Chawla MS, Chen XJ, Cofer GP, Hedlund LW, Kerby MB, Ottoboni TB, Johnson GA. Hyperpolarized ^{3}He microspheres as a novel vascular signal source for MRI. *Magn Reson Med* 2000;43:440–445.

9. Chawla MS, Chen XJ, Möller HE, Cofer GP, Wheeler CT, Hedlund LW, Johnson GA. *In vivo* magnetic resonance vascular imaging using laser-polarized ^{3}He microbubbles. *Proc Natl Acad Sci U S A* 1998;95:10832–10835.

10. Mugler JP 3, Driehuys B, Brookeman JR, Cates GD, Berr SS, Bryant RG, Daniel TM, de Lange EE, Downs JH 3, Erickson CJ, Happer W, Hinton DP, Kassel NF, Maier T, Phillips CD, Saam BT, Sauer KL, Wagshul ME. MR imaging and spectroscopy using hyperpolarized ^{129}Xe gas: preliminary human results. *Magn Reson Med* 1997;37:809–815.

11. Swanson SD, Rosen MS, Agranoff BW, Coulter KP, Welsh RC, Chupp TE. Brain MRI with laser-polarized ^{129}Xe. *Magn Reson Med* 1997;38:695–698.

12. Wagshul ME, Button TM, Li HF, Liang Z, Springer CS, Zhong K, Wishnia A. *In vivo* MR imaging and spectroscopy using hyperpolarized ^{129}Xe. *Magn Reson Med* 1996;36:183–191.

13. Duhamel G, Choquet P, Grillon E, Lamalle L, Leviel JL, Ziegler A, Constantinesco A. Xenon-129 MR imaging and spectroscopy of rat brain using arterial delivery of hyperpolarized xenon in a lipid emulsion. *Magn Reson Med* 2001;46:208–212.

14. Möller HE, Chawla MS, Chen XJ, Driehuys B, Hedlund LW, Wheeler CT, Johnson GA. Magnetic resonance angiography with hyperpolarized ^{129}Xe dissolved in a lipid emulsion. *Magn Reson Med* 1999;41:1058–1064.

15. Wolber J, Rowland IJ, Leach MO, Bifone A. Perfluorocarbon emulsions as intravenous delivery media for hyperpolarized xenon. *Magn Reson Med* 1999;41:442–449.

16. Bifone A, Song YQ, Seydoux R, Taylor RE, Goodson BM, Pietrass T, Budinger TF, Navon G, Pines A. NMR of laser-polarized xenon in human blood. *Proc Natl Acad Sci U S A* 1996;93:12932–12936.

17. Golman K, Axelsson O, Johannesson H, Månsson S, Olofsson C, Petersson JS. Parahydrogen-induced polarization in imaging: subsecond (13)C angiography. *Magn Reson Med* 2001;46:1–5.

18. Golman K, Ardenkjær-Larsen JH, Svensson J, Axelsson O, Hansson G, Hansson L, Johannesson H, Leunbach I, Månsson S, Petersson JS, Pettersson G, Servin R, Wistrand LG. ^{13}C-angiography. Proc Contrast Media Research, Scientific meeting, Capri, Italy 2001.

19. Hall DA, Maus DC, Gerfen GJ, Inati SJ, Becerra LR, Dahlquist FW, Griffin RG. Polarization-Enhanced NMR Spectroscopy of Biomolecules in Frozen Solution. *Science* 1997;276:930–932.

20. de Boer W, Borghini M, Morimoto K, Niinikoski TO, Udo F. Dynamic Polarization of Protons, Deuterons, and Carbon-13 Nuclei: Thermal Contact Between Nuclear Spins and an Electron Spin-Spin Interaction Reservoir. *Journal of Low Temperature Physics* 1974;15:249–267.

21. Svensson J, Månsson S, Petersson JS, Olsson LE. Hyperpolarized ^{13}C MR angiography using trueFISP. Proc International Society for Magnetic Resonance in Medicine, 10th Scientific Meeting, p 2010, Honolulu, USA 2002.

22. Oppelt A, Graumann R, Barfuss H, Fischer H, Hartl W, Schajor W. FISP—a new fast MRI sequence. *Electromedica* 1986;54:15–18.

23. Hennig J. Echoes—How to Generate, Recognize, Use or Avoid them in MR-Imaging Sequences. Part II: Echoes in imaging sequences. *Concepts Magnet Reson* 1991;3:179–192.

24. Deimling M, Heid O. Magnetization Prepared True FISP Imaging. Proc Society of Magnetic Resonance, Scientific meeting, p 495, San Fransisco 1994.

25. Listerud J, Einstein S, Outwater E, Kressel HY. First principles of fast spin echo. *Magn Reson Q* 1992;8:199–244.

26. Svensson J, Petersson JS, Stahlberg F, Larsson EM, Leander P, Olsson LE. Image artifacts due to a time-varying contrast medium concentration in 3D contrast-enhanced MRA. *J Magn Reson Imaging* 1999;10:919–928.

27. US Patent 6013810 2000.

28. Svensson J. Contrast-Enhanced Magnetic Resonance Angiography — Development and Optimization of Techniques for Paramagnetic and Hyperpolarized contrast media, PhD Thesis. Malmö, Sweden: Lund University; 2002.

29. Hennig J, Nauerth A, Friedburg H. RARE imaging: a fast imaging method for clinical MR. *Magn Reson Med* 1986;3:823–833.

30. Herzka DA, Kellman P, Aletras AH, Guttman MA, McVeigh ER. Multishot EPI-SSFP in the heart. *Magn Reson Med* 2002;47:655–664.

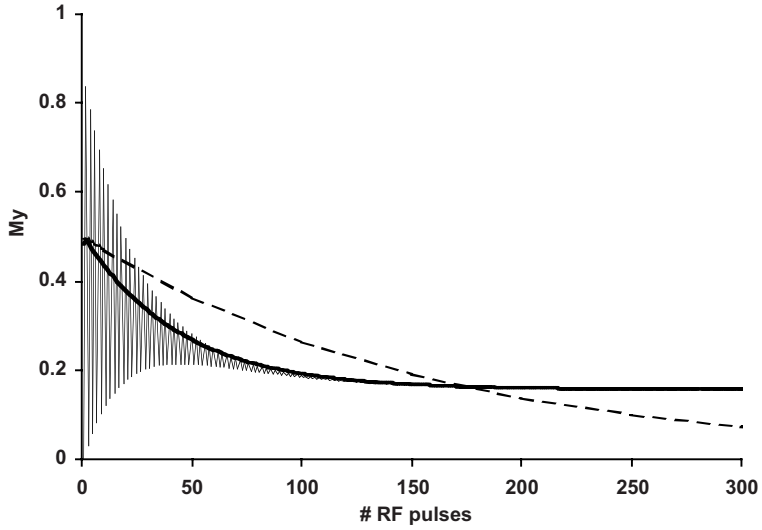

Figure 1. Simulation of transverse magnetization at TE during a trueFISP pulse train assuming thermally polarized spins without (thin line) and with (thick line) a $\theta/2$ pre-pulse. The number of pulses required to reach steady state is the same in both cases, but oscillation is greatly reduced if a pre-pulse is used. T_1/T_2 = 1200/150 ms (blood), TE/TR = 5/10 ms, θ = 60°. For hyperpolarized spins (T_1/T_2 = 5000/500 ms) no steady state is reached, instead, the magnetization eventually decays to the thermal equilibrium value (dashed line). The thermally and hyperpolarized curves are normalized to have equal amplitudes after RF-pulse #1.

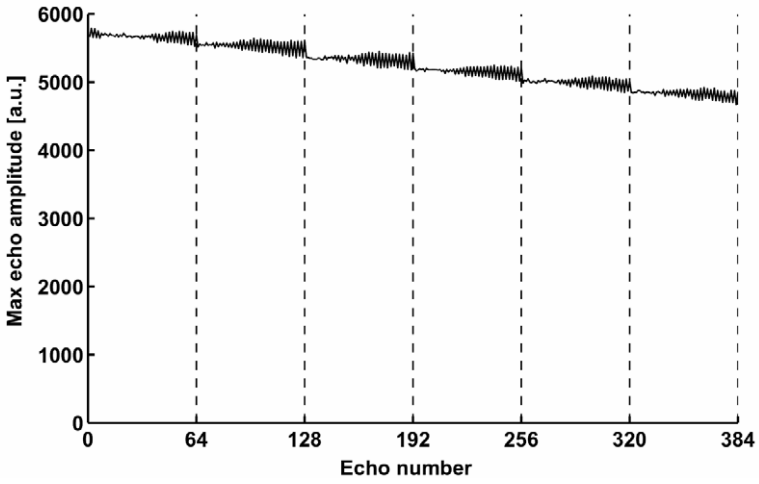

Figure 2. The maximum echo amplitude from each phase-encoding step in an experiment with 15 consecutively acquired images. Data from the first 6 images are shown. The experiment was performed without phase-encoding gradients to study the efficacy of the flip-back pulse. Each image acquisition consists of 64 phase-encoding steps, preceded by a $\theta/2$ preparation pulse, and ended by a $\theta/2$ flip-back pulse to store the magnetization in the longitudinal direction. Dashed lines indicate the position of the flip-back pulses. The magnetization is well preserved from one image acquisition to the next.

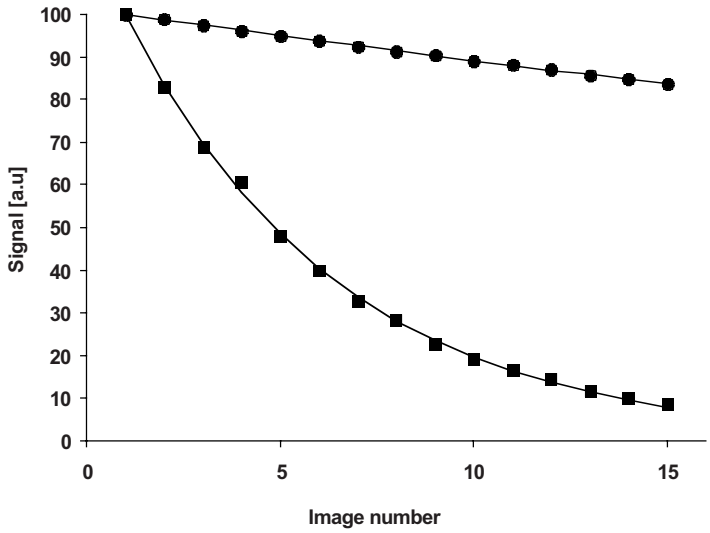

Figure 3. Signal variation in 15 consecutively acquired images using the flip-back technique and $\theta = 180°$ for HP ^{13}C in water (circles) and *in vivo* (squares). Signal is preserved from one image to the next, but decays faster *in vivo* than in the water. Assuming that no magnetization is lost in the flip-back process or between image acquisitions, the signal drop reflects the T_2 relaxation. The lines in the figure are mono-exponential fits to the measured values, yielding $T_2 \approx 18$ s for the ^{13}C molecule in water, and $T_2 \approx 1.3$ s *in vivo*.

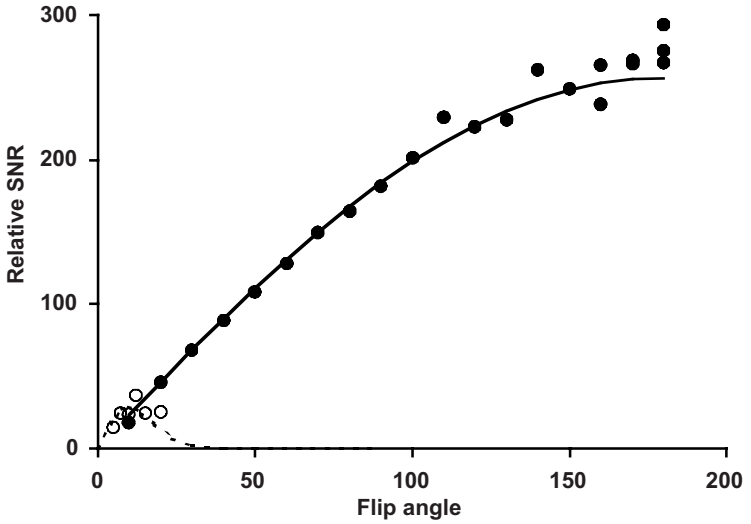

Figure 4. Flip angle dependence for the trueFISP pulse sequence and the hyperpolarized ^{13}C-based contrast medium. Measured values (●) and theoretical values calculated using Eq. [4] (solid line) agree very well. The optimal flip angle is 180°. The two data sets are normalized at 70°. For comparison, the corresponding calculated (dashed line) and measured values (○) for a FLASH pulse sequence are also plotted.

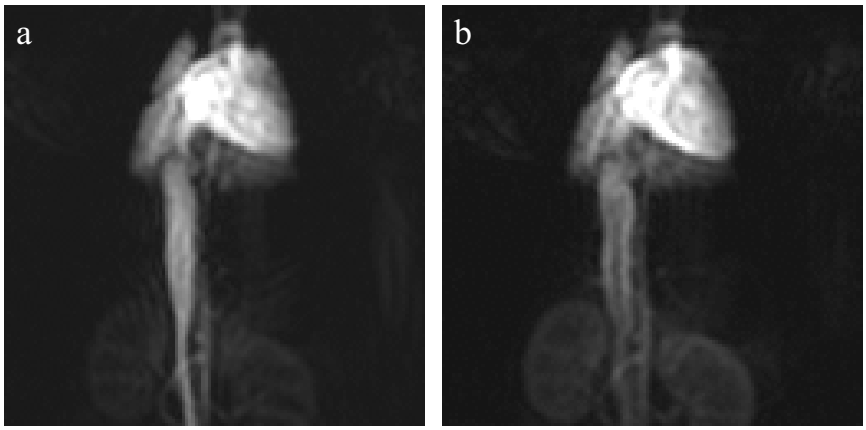

Figure 5. Series of angiograms covering the thoracic and abdominal area, acquired immediately after intravenous injections of 3 ml hyperpolarized ^{13}C CM. The first image in the series (a) visualizes several of the main vessels in the area. Using a flip-back pulse between image acquisitions, steady-state magnetization could be preserved, and signal remains high in subsequently acquired images. (b) is the fourth image from the same image series.

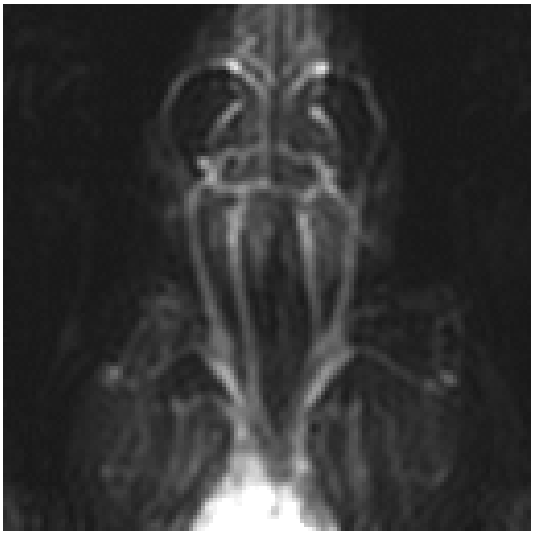

Figure 6. The first image in a series of angiograms covering the head-neck area, acquired using the same technique as for the thoracic-abdominal angiograms in Figure 5. Several of the major vessels are clearly discernible, but there is also some enhancement of other tissue, indicating a leakage of the ^{13}C CM into the extravascular space.

Paper III

FULL PAPERS

Magnetic Resonance in Medicine 48:223–232 (2002)

Quantitative Measurement of Regional Lung Ventilation Using ^{3}He MRI

Anselm J. Deninger,[1] Sven Månsson,[2*] J. Stefan Petersson,[1] Göran Pettersson,[1] Peter Magnusson,[1] Jonas Svensson,[3] Björn Fridlund,[1] Georg Hansson,[1] Ingrid Erjefeldt,[1] Per Wollmer,[4] and Klaes Golman[1]

A new strategy for a quantitative measurement of regional pulmonary ventilation using hyperpolarized helium-3 (^{3}He) MRI has been developed. The method employs the build-up of the signal intensity after a variable number of ^{3}He breaths. A mathematical model of the signal dynamics is presented, from which the local ventilation, defined as the fraction of gas exchanged per breath within a given volume, is calculated. The model was used to create ventilation maps of coronal slices of guinea pig lungs. Ventilation values very close to 1 were found in the trachea and the major airways. In the lung parenchyma, regions adjacent to the hilum showed values of 0.6–0.8, whereas 0.2–0.4 was measured in peripheral regions. Monte Carlo simulations were used to investigate the accuracy of the method and its limitations. The simulations revealed that, at presently attainable signal-to-noise ratios, the ventilation parameter can be determined with a relative uncertainty of <5% over a wide range of values. Magn Reson Med 48:223–232, 2002. © 2002 Wiley-Liss, Inc.

Key words: hyperpolarized gas MRI; functional MRI; helium-3; MRI of lungs; regional pulmonary ventilation

The measurement of regional pulmonary ventilation is of major importance in studies of lung physiology and investigations of lung disease. It is well known that ventilation deficiencies are symptomatic in many obstructive or restrictive pulmonary diseases. Established techniques for studies of the regional distribution of ventilation are based on measurement of the delivery (wash-in) or the clearance rate (wash-out) of radioactive gases with a long half-life, e.g. ^{133}Xe (1). With short-lived radioactive gases, such as ^{81m}Kr or ^{19}Ne, regional ventilation can be studied during continuous inhalation of the gas (2,3). Qualitative information about regional ventilation can also be obtained with radioactive aerosols (4). However, the temporal resolution of these techniques is on the order of 10 min. A better temporal resolution has been obtained using X-ray CT with xenon gas as a contrast agent (5–7). In those studies, information about regional pulmonary ventilation is obtained either from the subtraction of xenon enhanced and unenhanced images, or from sampling regional tracer delivery or clearance followed by mathematical analysis of the concentration–time curves. However, apart from limitations in spatial resolution or sensitivity, these methods involve exposing the subject to ionizing radiation during the examination.

The advent of hyperpolarized ^{3}He MRI opened the possibility to visualize ventilated airspaces of the lungs in a noninvasive way. Morphological studies have demonstrated pronounced differences in the signal distribution between healthy and diseased lungs (8–11). Irregular signal patterns observed, e.g., in asthmatic or emphysematous lungs have enabled the qualitative identification of local ventilation deficiencies. In addition, rapid imaging of the lungs allowed a dynamic visualization of gas flow patterns, permitting an investigation of inspiration and expiration processes with subsecond temporal resolution. Such studies have been carried out using FLASH (12), EPI (13), or spiral sampling techniques (14), the latter being particularly advantageous in terms of temporal resolution.

In addition to spin-density imaging, the spin-lattice relaxation time T_1 of ^{3}He in the lungs can be exploited to quantify the intrapulmonary oxygen partial pressure p_{O2} (15–18). The distribution of oxygen present immediately after an inspiration of air is, at first approximation, determined by ventilation-dependent oxygen delivery. Oxygen-sensitive ^{3}He-MRI techniques therefore provide insights about regional lung ventilation.

In the present investigation, a quantitative MRI-based technique for the determination of lung ventilation is presented. The signal development after wash-in of the contrast medium, hyperpolarized ^{3}He, is described in a mathematical model, which introduces a regional ventilation parameter. This approach permits a rapid and accurate evaluation of pulmonary ventilation. Results are presented as parametric images, allowing regional quantification of pulmonary ventilation on a pixel-by-pixel basis.

THEORY

The concept of the method is sketched in Fig. 1. Several breathing cycles are performed, each cycle consisting of a constant number of N air breaths, followed by a variable number of n pure ^{3}He breaths. The time interval between two consecutive breaths is τ. A single image is taken immediately after the last ^{3}He inspiration of each ^{3}He-breath-

[1]Amersham Health R&D, Medeon, SE – 205 12 Malmö, Sweden.

[2]Department of Experimental Research, Malmö University Hospital, SE – 205 02 Malmö, Sweden.

[3]Department of Radiation Physics, Malmö University Hospital, SE – 205 02 Malmö, Sweden.

[4]Department of Clinical Physiology, Malmö University Hospital, SE – 205 02 Malmö, Sweden.

*Correspondence to: Sven Månsson, Dept. of Experimental Research, Malmö University Hospital, SE – 205 02 Malmö, Sweden.

Received 11 December 2001; revised 25 February 2002; accepted 9 March 2002.

DOI 10.1002/mrm.10206

Published online in Wiley InterScience (www.interscience.wiley.com).

© 2002 Wiley-Liss, Inc.

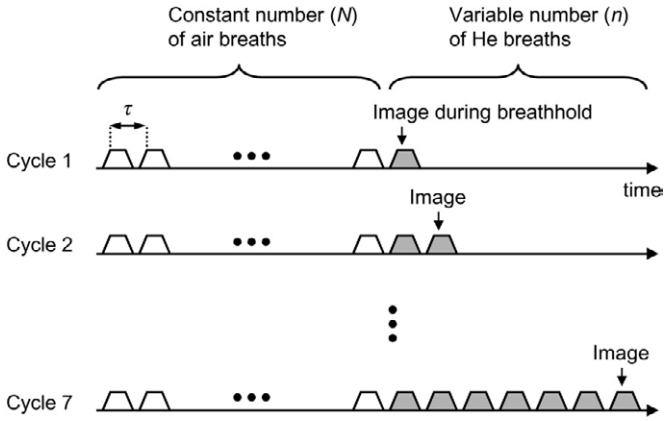

FIG. 1. Sketch of the breathing cycles used in the experiment. Each cycle consists of a constant number of N air breaths, followed by an increasing number of $n = 1, 2, 3, \ldots, 7$ helium breaths. Imaging is performed during inspiratory apnea after the last ^{3}He breath of a cycle.

ing interval. Since only one image per cycle is acquired, RF depolarization of ^{3}He need not be considered in the following derivation.

Our model treats ventilation as a discontinuous, cyclic process, similar to the approach by Möller et al. (18). During each ^{3}He inspiration, a fraction r of a given volume element is replaced by fresh ^{3}He gas, and a fraction q contains gas remaining from previous inspirations.

We accordingly define the ratios r and q:

$$r = \frac{V_{fr}}{V_{fr} + V_{old}}$$

$$q = \frac{V_{old}}{V_{fr} + V_{old}} \qquad [1]$$

where V_{old} and V_{fr} denote the volumes of old and fresh gas within the volume element, respectively. Certainly, $q = 1 - r$. Dead space gas is, to a first approximation, included in the fraction q.

We assume that breaths are identical, which is well fulfilled during mechanical respiration as employed in this study. The parameter r then gives the per-breath gas exchange ratio, which is used as a measure of lung ventilation. A novel approach of the presented model is to treat q and r as locally variable parameters, which allows an assessment of lung ventilation on a submillimeter scale.

After the j-th inspiration of ^{3}He in cycle n, the available nuclear magnetization $M(j, n)$ of ^{3}He within a given volume element consists of (i) the magnetization M_{new} of the fraction $(1–q)$ of fresh ^{3}He, and (ii) the magnetization of the fraction q of ^{3}He remaining from previous breaths of the same cycle (for $j \geq 2$). Fraction (i) is subject to spin-lattice relaxation in the external reservoir, $T_{1,\mathrm{ext}}$, which mainly results from surface relaxation (19,20) and field gradient relaxation (21,22). Fraction (ii), by contrast, is affected by oxygen-induced relaxation in the lung, $T_{1,\mathrm{O2}}$, during the interval τ. Other relaxation mechanisms, such as ^{3}He dipolar relaxation (23) and surface relaxation within the lung (16) play an insignificant role only and are neglected here.

Thus, the net magnetization $M(j, n)$ in the volume of interest can be written recursively:

$$M(j,n) = M_{new}(n) \cdot (1 - q) \cdot \exp(-[j-1]\tau/T_{1,ext}) + M(j-1,n) \cdot q \cdot \exp(-\tau/T_{1,O2}) \qquad [2]$$

with a start value $M(0, n) \equiv 0$ and an exponentially decreasing "reservoir magnetization" $M_{\mathrm{new}}(n)$

$$M_{new}(n) = C \exp\left(-b(n)\frac{\tau}{T_{1,ext}}\right)$$

$$b(n) = (n-1) \cdot N + \sum_{i=1}^{n-1} i = (n-1)(N + n/2). \qquad [3]$$

Here, b counts the total number of inspirations between the first ^{3}He breath of cycle 1 and the first ^{3}He breath of cycle n, and C is a proportionality factor.

Oxygen-induced relaxation within the lungs is caused by dipolar coupling between electronic spins of O_2 and the nuclear spins of ^{3}He (24). The inverse of $T_{1,\mathrm{O2}}$ is proportional to the oxygen partial pressure p_{O2}. When the inspiratory gas is switched from air to ^{3}He, oxygen present in the lungs is washed out. After j inspirations of ^{3}He, p_{O2} has decreased to:

$$p_{O2}(j) = p_0 q^j. \qquad [4]$$

p_0 denotes the oxygen partial pressure present within the volume element prior to the first ^{3}He breath of a cycle. For simplicity, we neglect the uptake of oxygen into the blood, which will be justified by calculations presented below. The oxygen-induced relaxation time of ^{3}He after

breath j, denoted $T_{1,O2}(j)$, is in this approximation only influenced by the wash-out of p_{O2} and given by:

$$T_{1,O2}(j) = \xi / p_{O2}(j) = \xi / (p_0 q^j). \quad [5]$$

ξ is a proportionality factor that has a value of approximately 2.6 bar · s at body temperature (24).

For abbreviation, we define $E \equiv \exp(-\tau / T_{1,ext})$. Inserting Eqs. [3] and [5] into Eq. [2] yields:

$$M(j,n) = CE^{(n-1)(N+n/2)}E^{j-1}(1-q) + qM(j-1,n)\exp\left(-\frac{p_0 q^{j-1}\tau}{\xi}\right). \quad [6]$$

Equation [6] can be rearranged to explicitly express the signal intensity $S(n)$, which is proportional to the magnetization $M(n, n)$ of the imaged breath:

$$S(n) = const \cdot E^{(n-1)(N+n/2)} \times (1-q)\sum_{k=0}^{n-1}\left(E^{n-k-1}q^k\exp\left(-\frac{p_0\tau q^{n-k-1}}{\xi}\sum_{i=0}^{j}q^i\right)\right). \quad [7]$$

Elimination of the inner sum in Eq. [7] gives the final expression for the MR signal of the considered volume element after the n-th ^{3}He inspiration:

$$S(n) = const \cdot E^{(n-1)(N+n/2)} \times (1-q)\sum_{k=0}^{n-1}\left(E^{n-k-1}q^k\exp\left(-\frac{p_0\tau q^{n-k}(1-q^k)}{\xi \quad 1-q}\right)\right). \quad [8]$$

A nonlinear least-squares fit of the signal intensities of the n images to Eq. [8] is used to compute the ratio q and thus the ventilation parameter $r = (1 - q)$.

MATERIALS AND METHODS

Polarization and Administration of ^{3}He

^{3}He was polarized using spin-exchange optical pumping, which has been described in detail elsewhere (25,26). In a prototype commercial polarizer (IGI 9600 helium polarizer, Amersham Health, Durham, NC), a gas quantity of 1.1 bar · liter was polarized to 30–40% within 10–15 hr.

The polarized gas was transferred into a plastic bag (volume 300 ml, Tedlar®; Jensen Inert, Coral Springs, FL), which was connected to an in-house-built respirator. Via a switch valve, the computer-controlled respirator was capable of administering either air or hyperpolarized ^{3}He to the animal. The plastic bag containing ^{3}He was placed within a rigid cylinder and positioned 0.5 m outside the magnet. To expel the polarized gas, the cylinder was pressurized with argon. The computer control also served to trigger the MR imaging sequence, i.e., to synchronize gas delivery and imaging. The reproducibility of administered gas volumes was tested in separate experiments and was better than 2%.

Animal Preparation

All experiments were approved by the local ethical committee (Malmö/Lunds djurförsöksetiska nämnd; appl. no. M283-00). Four Albino guinea pigs (male, 350–400 g; breeder: M&B, Ry, Denmark) were anesthetized with a mixture of tiletamine/zolazepam (Zoletil® 50 vet., Boehringer Ingelheim, Copenhagen, Denmark) and xylazine (Rompun® vet., Bayer, Leverkusen, Germany) intraperitoneally and butorphanol (Torbugesic®; Fort Dodge Animal Health, Fort Dodge, IA) intramuscularly. The left jugular vein and the right carotid artery were catheterized for intravenous administration of anesthesia and a neuromuscular blocking agent (pancuronium, Pavulon®; Organon Teknika, Boxtel, the Netherlands), and for measurement of arterial blood pressure. After tracheal intubation, the animals were placed in the MR scanner in supine position and ventilated by the respirator mentioned above. During the experiment, body temperature, blood pressure, inspiratory pressure, and tidal volume were monitored continuously. The breathing rate was set to 40 breaths/min (τ = 1.5 sec). The inspiratory pressure was 12 mbar and the tidal volume 0.7–0.8 ml per 100 g body weight. Inspiration and expiration times were 0.5 sec and 1.0 sec, respectively. N = 20 air breaths were administered per breathing cycle for equilibration, followed by n = {1, 2, …, 7} ^{3}He breaths. Immediately after the last ^{3}He inspiration of each cycle, imaging was performed during a 2-sec breathhold period.

Imaging

All experiments were performed on a 2.35 T scanner (BioSpec, Bruker Medical, Ettlingen, Germany) using a dual-frequency birdcage RF coil (Bruker Medical) with 72 mm diameter, operating at the Larmor frequencies of ^{1}H (100.1 MHz) and ^{3}He (76.3 MHz). Coronal, sagittal, and axial proton scout images were acquired for proper localization of the ^{3}He images.

^{3}He imaging of a single, coronal slice of the lungs was performed using a gradient echo sequence with TR = 15 ms, TE = 2 ms, flip angle ≈ 15°, field of view = 60 × 50 mm^2, slice thickness 5 mm, acquisition matrix 64 × 64. Before and after the air/He cycles sketched in Fig. 1, ^{3}He reference images were obtained in order to monitor the T_1 relaxation of the hyperpolarized gas in the plastic bag.

Data Analysis

Data analysis was carried out using software implemented in MATLAB (MathWorks, Natick, MA). In a first step, the external relaxation time $T_{1,ext}$ was computed from the decay of the average image intensity of the reference images. Then, a pixel-by-pixel least-squares fit of Eq. [8] was performed to calculate the ventilation parameter r. Noise pixels were excluded by selecting a threshold SNR of 10 in the first image (n = 1, i.e. the image with the lowest signal intensity). Throughout the work, the SNR of a pixel was computed by dividing the pixel intensity by the noise level, which was estimated from the mean background signal S_{back} using the simple relation (27):

$$\text{noise} = \sqrt{2/\pi}S_{back}. \quad [9]$$

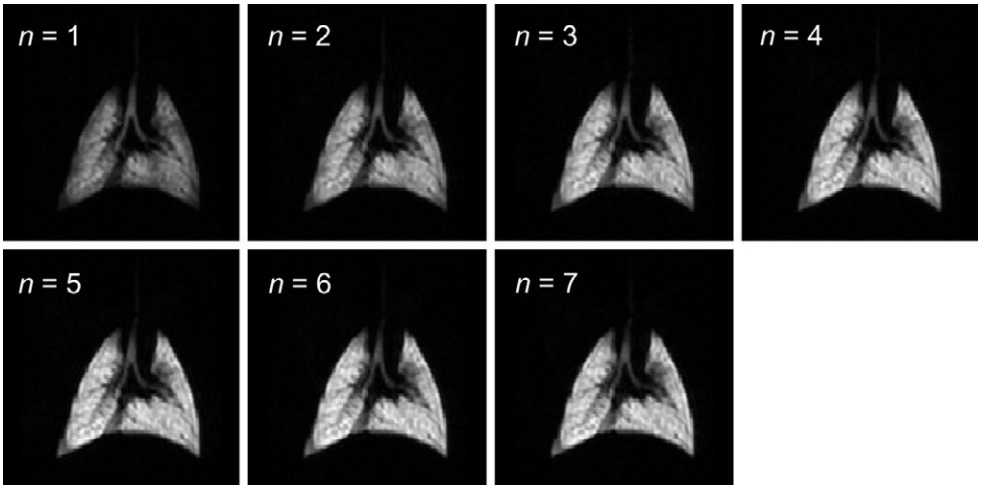

FIG. 2. Coronal ^{3}He images of a guinea pig's lungs, acquired after n helium breaths. Voxel size is 0.9 × 0.8 × 5 mm^3.

For the oxygen partial pressure, an input value of p_0 = 135 mbar was used in the fit, employing the result of an oxygen measurement in guinea pig lungs published by Möller et al. (18).

In order to test less ^{3}He-consuming variants of the experiment, additional data analysis was performed within a reduced subset of images. Apart from the entire series (images after cycles with {1…7} He breaths), only those images acquired after {1…5} and {1, 2, 5} breaths were analyzed in a representative animal (#3).

Simulation of Input Parameter Sensitivity

In order to investigate the influence of errors in the input parameters p_0 and $T_{1,\mathrm{ext}}$, simulated noiseless signal intensities were generated according to Eq. [8] using a simulation program implemented in Delphi 5.0 (Borland Software Corp., Scotts Valley, CA). Signal intensities were simulated with p_0 ranging from 0–200 mbar and $T_{1,\mathrm{ext}}$ ranging from 5–100 min. The ventilation parameter r was calculated from the simulated intensities using fixed values of p_0 = 135 mbar and $T_{1,\mathrm{ext}}$ = 30 min, and the result was compared with the actual value of r used for generation of the simulated intensities.

Simulation of Noise Sensitivity

Monte Carlo (MC) simulations of the signal dynamics (Eq. [8]) were performed to test the accuracy of the measurement method. Pixel intensities were computed as a function of r and the SNR of the first image using fixed values for the parameters p_0 and $T_{1,\mathrm{ext}}$. The intensities were subsequently obscured by noise, assuming a Gaussian distribution of intensities around the true value (27,28). For each combination of input r and SNR, the simulation was repeated 1000 times and the standard deviation Δr of the resulting distribution of r was calculated and used to quantify the uncertainty of the ventilation parameter.

In addition, the ^{3}He-saving experiments using a reduced number of breathing cycles were simulated. Cycles with {1…7}, {1…6}, {1…5}, {1…4}, and {1…3} He images, as well as combinations of images acquired after {1, 2, 4}, {1, 2, 5}, or {1, 3, 5} He breaths were evaluated. Of all possible combinations of three air/^{3}He cycles, only combinations starting with n = 1 were included, in order to minimize the total ^{3}He consumption.

RESULTS

Imaging

In all animals, lung images with typical SNR values ranging from 50 (first image, 1 He breath) to 85 (last image, 7 He breaths) were obtained. A representative set of spin density images (animal 1) acquired after n He breaths (n = 1…7) is shown in Fig. 2. Apart from the lungs, the trachea and the main bronchi are visible in the selected slice. The external relaxation time $T_{1,\mathrm{ext}}$ was computed from reference images (not shown) acquired before and after the ventilation measurement, yielding values between 20–30 min.

Typical signal intensities measured in regions within highly, moderately, and poorly ventilated lung areas are plotted as a function of n in Fig. 3. In the example, ventilation parameters of r = 0.77 (pixel next to the hilum), r = 0.48, (pixel in central lung region), and r = 0.16 (pixel in peripheral region) were determined.

Maps of the ventilation parameter r in two different animals (1 and 3) are shown in Fig. 4. Values of r very close to 1 are found in the trachea and the major airways, indicating a complete renewal of gas per breath in these regions.

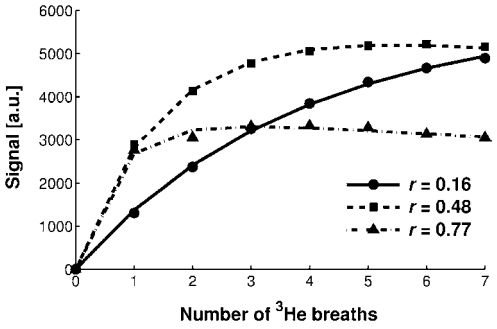

FIG. 3. Typical signal evolution in lung regions with high ($r = 0.77$), intermediate ($r = 0.48$), and low ($r = 0.16$) ventilation values. The symbols represent the signal intensities in the ^{3}He images and the lines show a least squares fit of Eq. [8] to the data. Error bars, corresponding to the noise level in the images, are smaller than the graphical display of data points.

In the left lung of animal 1, the third bifurcation of the airways is discernible in the parametric image by its high ventilation values, although it is barely identified in the original spin density image (Fig. 2).

In central lung areas, regions close to the hilum still exhibit large r-values ($r \approx 0.55-0.75$). In peripheral areas, values are considerably lower ($r \approx 0.20-0.40$). The lowest ventilation parameters were measured in the edges of the lungs, where results of $r \approx 0.15-0.25$ were obtained.

The data of four animals are summarized in the form of histograms of r (Fig. 5). In all histograms, a central peak is observed, corresponding to ventilation values (mean ± SD) of 0.47 ± 0.15, 0.45 ± 0.07, 0.45 ± 0.12, and 0.46 ± 0.10 in animals 1–4, respectively. Values of r close to 1 in the trachea pixels give rise to a second peak at the upper border of the histograms.

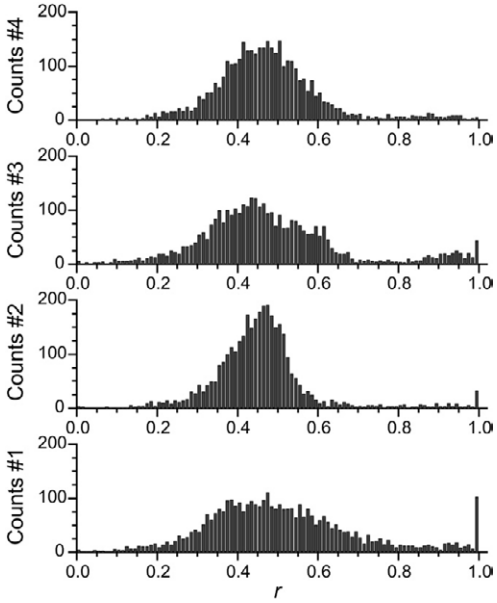

FIG. 5. Histograms of the ventilation parameter r in animals 1–4.

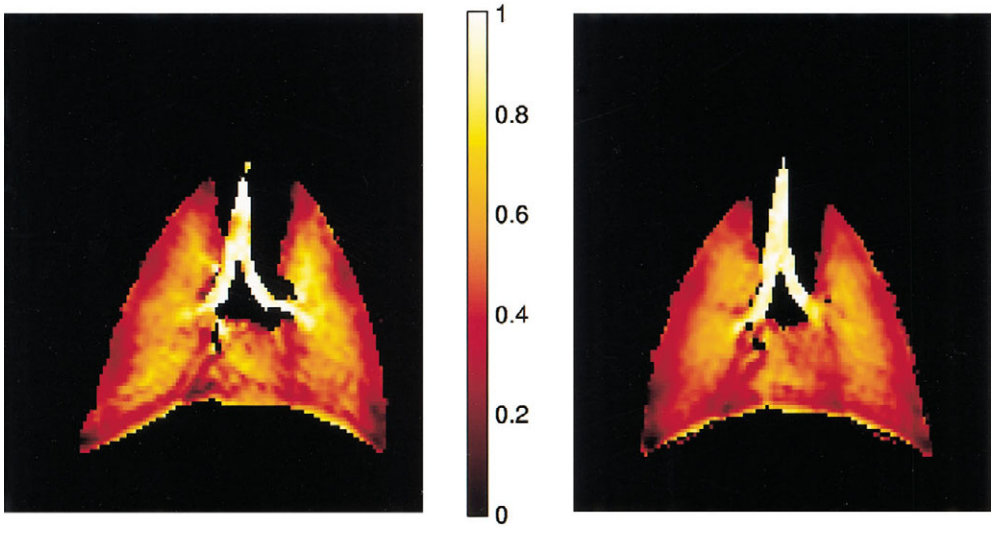

FIG. 4. Parametric map of the ventilation parameter r in animals 1 (left) and 3 (right).

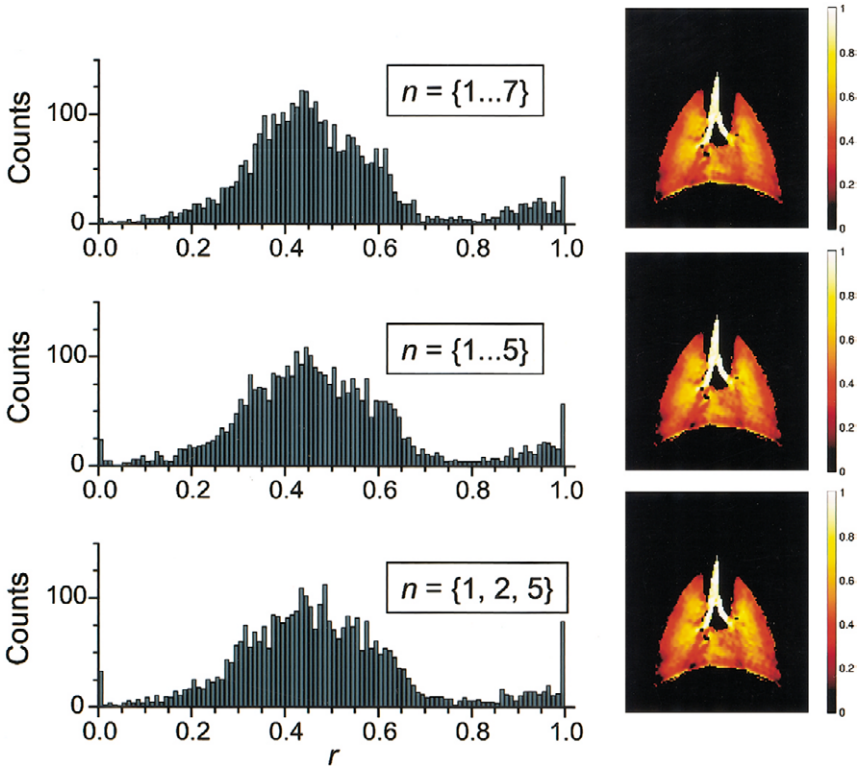

FIG. 6. Histograms and parametric maps of the ventilation parameter r in animal 3, computed from the analysis of the entire dataset (n = {1…7}) and from a reduced set of images (n = {1…5} and n = {1, 2, 5}).

Figure 6 presents parametric maps and histograms of r, computed from a reduced number of images of animal 3. A comparison of the distributions shows that the accuracy of measurement decreases only marginally for the {1…5} and {1, 2, 5} dataset: the mean value of the central peak is 0.45 in all three histograms, the SD increases slightly (values of 0.14 for both {1…5} and {1, 2, 5}). The highest impact of the reduced number of images on the accuracy of the fit is found for extreme values of r, as seen from the increase of the peaks at $r \approx 0$ and $r \approx 1$.

Simulation of Input Parameter Sensitivity

The influence of errors in the input parameter p_0 is depicted in Fig. 7a. Shown is the relative error of the ventilation parameter, $(r_{\text{output}} - r_{\text{input}})/r_{\text{output}}$, as a function of input p_0, where r_{input} is the ventilation value used for synthesis of simulated data (see labels) and r_{output} is the ventilation value obtained from data analysis. The simulation shows that the pulmonary oxygen partial pressure has only a minor effect on the signal dynamics. The largest influence is seen for slow gas replacement (low r-values).

In Fig. 7b, the relative error of the resulting value of r is plotted as a function of the input $T_{1,\text{ext}}$. Note that the influence of ^{3}He relaxation in the reservoir is much more critical than the effect of p_{O2}. Again, the largest influence is found for low r-values.

Simulation of Noise Sensitivity

MC simulations were carried out to test the robustness of the method in the case of noisy data. In Fig. 8a, the SNR of the first image was varied. The plot shows the standard deviation Δr of the resulting normal distributions of r as a function of the input SNR of the simulation. As expected, the accuracy of measurement increases with high SNR values. The solid line is a fit curve, using a reciprocal function:

$$\Delta r = (\text{SNR})^{-\zeta}. \qquad [10]$$

The fit yields $\zeta = 0.99(5)$, revealing an inverse proportionality between the error of r and the SNR.

In Fig. 8b, experiments with a reduced number of air/^{3}He cycles were simulated. Standard deviations Δr are plotted as a function of the number of ^{3}He images used in the analysis. The accuracy of r increases with the number

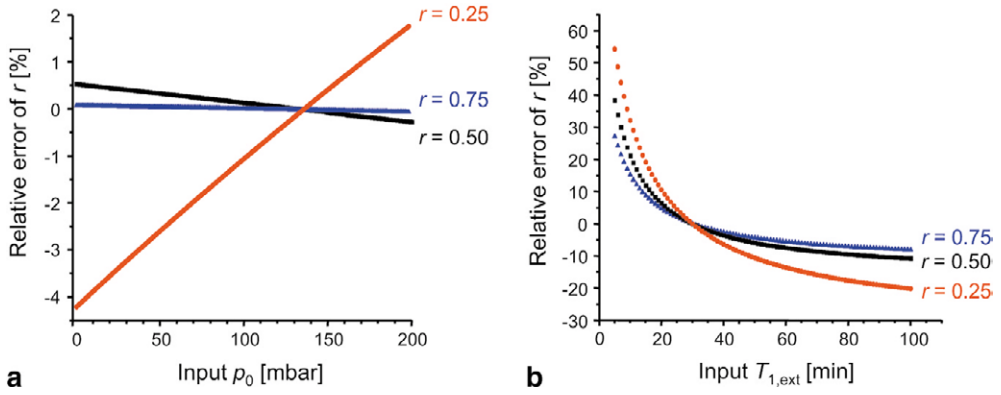

FIG. 7. Results of simulations illustrating the influence of input parameters on the fit of Eq. [8]. Shown is the relative error $\Delta r/r$, (**a**) for data generated with different oxygen partial pressures p_0, but analyzed with a fixed value of p_0 = 135 mbar; (**b**) for data generated with different relaxation times $T_{1,ext}$ of ^{3}He in the reservoir during the experiment, but analyzed with $T_{1,ext}$ = 30 min. Note the different scale of the ordinate in **a** and **b**. [Color figure can be viewed in the online issue, which is available at www.interscience.wiley.com.]

of images available for the fit, yet the benefit of including the $n = 6$ and $n = 7$ images in the analysis is relatively small. As in the case of real data (Fig. 6), a combination of {1, 2, 5} He breaths yields almost as accurate a result as the complete {1, 2, 3, 4, 5} set.

In an actual lung image, the SNR is low in poorly ventilated areas, i.e., ventilation and SNR are correlated. In order to test the accuracy of the computation under such conditions, the MC simulation was repeated with increasing SNR levels for increasing values of r. The result of a simulation where the SNR in the first image was scaled linearly from 0–65 over the full range of r ($0.005 < r < 0.995$) is summarized in Fig. 9. As in the actual image analysis, data with SNR < 10 (for $n = 1$) were not included in the computation. In the simulation, this cutoff criterion suppresses all values of $r < 0.15$, which is observed in the guinea pig data also (cf. Fig. 5). Figure 9 shows that the uncertainty Δr is <0.02 for a wide range of r-values. Viewed differently, the relative error (Δr / r) is less than 5% for $r \geq 0.3$.

DISCUSSION

The method of measurement presented here computes a regional ventilation parameter from the build-up of the hyperpolarized ^{3}He signal after a varying number of

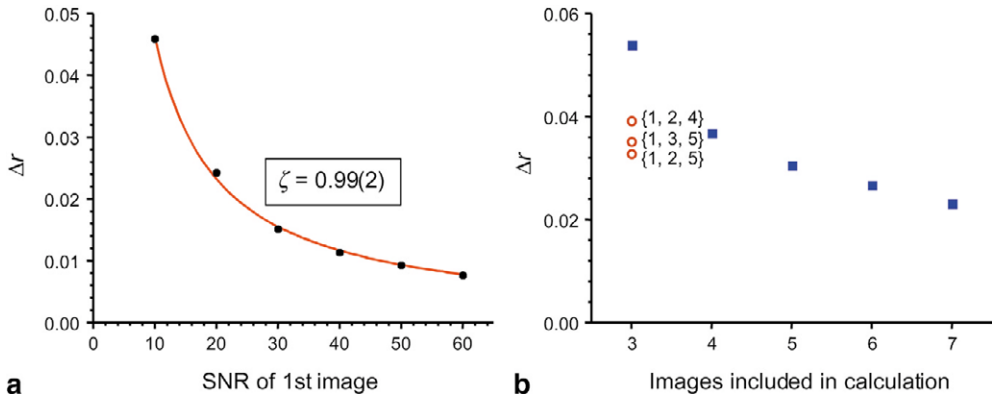

FIG. 8. Monte Carlo simulations of the ventilation measurement. The standard deviation Δr of the distribution of calculated r-values is plotted vs. (**a**) the SNR, (**b**) the number of images included in the fit of Eq. [8] (at fixed SNR of 20 in the first image). Values of $r = 0.50$, p_0 = 135 mbar and $T_{1,ext}$ = 30 min were used in the computation. In **b**, the squares refer to images acquired after {1…3} to {1…7} helium breaths, whereas the circles represent computations using only {1, 2, 4}, {1, 2, 5}, and {1, 3, 5} helium breaths, respectively. [Color figure can be viewed in the online issue, which is available at www.interscience.wiley.com.]

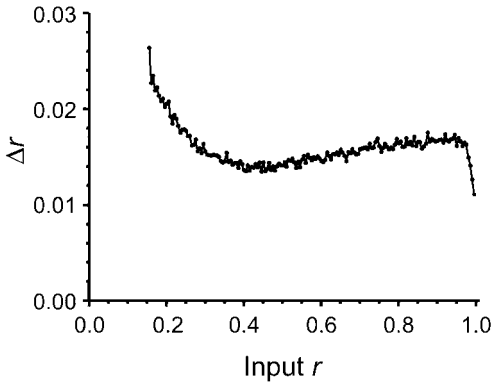

FIG. 9. Monte Carlo simulations of the ventilation measurement for different values of r. The standard deviation Δr of output r values is plotted as a function of the input r. The SNR is scaled linearly with the input r. Data with an SNR below 10 in the first "image" are omitted from analysis. Simulation parameters were $p_0 = 135$ mbar, $T_{1,ext} = 30$ min, image set = {1…7}.

wash-in breaths. After a ^{3}He breathing period, normal breathing conditions are restored by ventilating the animal with $N = 20$ air breaths. It is reasonable to believe that this number is sufficient to wash out all remaining helium gas and reestablish steady-state conditions: a recent publication (18) showed that alveolar gas composition in guinea pigs reached a steady state after 15 breaths of a new gas admixture.

Images were acquired during inspiratory apnea, i.e., at a fixed phase of the breathing cycle. The mathematical model assumes that within a given lung region a fraction r of the gas content is replaced after each inspiration, while another fraction q either remains in place or is transferred to a dead space region and back again from one breath to the next. The latter is certainly a simplification, as, e.g., the gas composition within the dead space region, and in particular the oxygen partial pressure, may change due to mixing with gas from another region. However, as proved by simulations of input parameter sensitivity (Fig. 7a), the influence of the oxygen partial pressure on the signal dynamics is weak. Consequently, it is justified to treat gas transported to and from dead space regions as "gas containing no fresh ^{3}He", i.e., to include any dead space effects in the fraction q of Eq. [1].

We note that the ventilation analysis is independent of absolute image intensity values as long as the intensity is sufficiently greater than the noise level. This means that the analysis is also independent of B_1 field inhomogeneities. This is a considerable advantage in functional ^{3}He MRI, as limitations of the RF coil homogeneity have been held responsible for signal voids in lung images (8), which can only be distinguished from true ventilation deficiencies by the experienced eye.

The model of the signal dynamics considers relaxation of ^{3}He due to the presence of oxygen in the lungs, as well as relaxation of ^{3}He in the reservoir during the experiment. While the latter can be computed from reference images, an assumption has to be made concerning the initial pulmonary oxygen partial pressure. We use a global value of $p_0 = 135$ mbar. This approximation certainly does not hold everywhere within the lungs. If additional images were acquired, a map of p_0 could be generated and included in the ventilation calculation. However, computer simulations (Fig. 7a) have shown that the error introduced by a deviation from the actual oxygen pressure is small: even at regional p_0-variations of 30 mbar, as found in human lungs (17), the relative error of r would be about 1.5% for low ventilation values ($r = 0.25$) and less than 0.5% for larger ventilation values ($r > 0.5$). Hence, the accuracy of the ventilation parameter is hardly affected by an incorrect estimate of the oxygen partial pressure and it is justified to approximate p_0 by a spatially constant value.

Furthermore, it seems legitimate to neglect the uptake of oxygen into the blood in this model. The mean value of $r \approx 0.45$ found in the histograms (Fig. 5) implies that, after one full helium breath, the oxygen concentration within the analyzed voxels has decreased to 55% of its initial value. Thus, oxygen is washed out at a rate of:

$$\frac{\Delta p_{O2}}{\Delta t} \approx \frac{(1 - 0.55) \cdot 135\text{mbar}}{1.5\text{s}} = 40.5\text{mbar/s} \quad [11]$$

which is about an order of magnitude larger than the oxygen uptake of guinea pigs under hypoxic conditions, as measured by Möller et al. (18).

On the other hand, the simulations show that "external" relaxation of the polarized gas has to be accounted for (Fig. 7b). If the $T_{1,ext}$ value used in the analysis differs from the "true" value by 5 min, the resulting relative error is 2–5%, depending on the value of r. Monitoring the helium polarization, for instance, by reference images acquired prior to and after the actual experiment, is thus important in these studies. In the present examination, $T_{1,ext}$ was limited to 20–30 min, due to the combined effects of surface relaxation within the plastic bag and magnetic field gradient-induced relaxation. The volume of the tube connecting the bag to the animal was small (a fraction of a ml) and the relaxation within this volume was thus ignored.

The parametric images (Fig. 4) show physiologically plausible values of the ventilation parameter. As expected, the gas is completely replaced in the trachea and the first bronchi after each inspiration. In peripheral areas of the lungs, values of $r \approx 0.3$ indicate that the gas admixture consists mainly of residual gas, which undergoes slow replacement only. However, the analysis does not work in the region of the diaphragm. Even though images are acquired in exactly the same phase of the breathing cycle, and despite the good reproducibility of tidal volumes guaranteed by the respirator, the position of the diaphragm can be expected to vary slightly between different images. Consequently, signal intensities will fluctuate in voxels close to the diaphragm; hence, the analysis will fail to deliver realistic results. The situation is thus similar to oxygen-sensitive ^{3}He-MRI, where unreliable values have been reported in regions containing a projection of the diaphragm (17). These voxels could be excluded by choosing a higher SNR threshold in the analysis; however, this

would also result in the elimination of the trachea voxels, where the SNR is reduced due to diffusive signal attenuation and partial volume effects (the diameter of the trachea is considerably smaller than the slice thickness).

Using MC simulations, the accuracy of this measurement method was tested. An inverse proportionality between the error of r and the pixel SNR was demonstrated. A similar dependence has been observed in oxygen-sensitive ^{3}He MRI (17). The MC simulations also showed that for typical SNR values (20–65), the relative accuracy ($\Delta r/r$) of the measurement is better than 5% for ventilation values $r > 0.3$. We therefore conclude that the accuracy in the present study is 2–6%. While nonventilated areas ($r \approx 0$) are not accessible by ^{3}He MRI at all, this result implies that it is possible to accurately measure lung ventilation on a regional scale in the trachea, the tracheobronchial tree as well as in alveolar space. This conclusion is endorsed by the animal experiments, where the results of the four animals were in close agreement: neither the mean values nor the standard deviations of the ventilation distributions differed considerably, indicating good reproducibility of the measurements.

The present ventilation model assumes that no transport of gas takes place between the helium inspiration and the acquisition of image data, i.e., no diffusive mixing of gas between well-ventilated and poorly ventilated regions occurs. This assumption calls for short imaging times and fast imaging sequences. The issue is particularly relevant with respect to 3D studies. We are currently investigating a 3D sequence capable of imaging 16 slices within a single breathhold (acquisition time <2 sec), with a voxel size similar to that of the present experiments. Preliminary results indicate that the SNR levels obtained in the present study can be preserved.

A future extension of the proposed method to human studies is conceivable, but several alterations have to be made. The decrease in arterial oxygen saturation after several hypoxic ^{3}He breaths presents a safety concern, as documented by Durand et al. (29). To circumvent this problem, a subject could be ventilated with a ^{3}He/O_2 mixture (e.g., 80% helium, 20% oxygen) instead of pure ^{3}He. A mixture of helium and oxygen is well tolerated by the human body and has long been used in deep-sea diving (30). Concessions would have to be made regarding the SNR: the dilution of ^{3}He in the inspiratory gas leads to a reduction in SNR by 20%. In addition, oxygen-induced relaxation must be considered. An oxygen content of 20% in the inspiratory gas mixture corresponds to a $T_{1,O2}$ of 13 sec. A time interval of 3–4 sec from the mixing of helium with oxygen to the acquisition of central k-space data would therefore lead to a further reduction in SNR by ~25%. On the other hand, human studies would most likely be performed using larger voxel sizes than those of the present small animal study. Therefore, decreased imaging gradients would reduce the diffusion attenuation of the signal (31) and regain SNR.

In order to limit the consumption of polarized gas, the total number of helium breaths could be reduced: as shown by initial experiments (Fig. 6) and MC simulations (Fig. 8b), a reasonable accuracy of measurement is retained even with images acquired after {1, 2, 5} He breaths only, i.e., using a total number of 8 He breaths rather than 28 as in the complete experiment.

While a modification of the mathematical model accounting for a heterogeneous inspiratory gas admixture could readily be accomplished, the reproducibility of lung volumes is no longer given for nonmechanical ventilation. A highly reproducible ^{3}He-bolus delivery to pigs and humans has been demonstrated (16), but parameters such as the lung volume prior to a He/air inspiration or the tidal volume are difficult to duplicate during spontaneous breathing. Thus, the alveolar gas composition and, in particular, the position of an image pixel within the lung will differ between individual He/air test inspirations. This will limit the accuracy of the method in human studies. Further investigations and computer simulations will be needed to evaluate this effect.

CONCLUSION

A quantitative measurement of regional pulmonary ventilation with high spatial and temporal resolution was realized utilizing MRI and hyperpolarized ^{3}He as contrast agent. In contrast to clinical routine ventilation measurement techniques, the method avoids any health risks due to ionizing radiation. The method complements dynamic ^{3}He imaging of lung ventilation, which provides subsecond temporal resolution but as yet limited quantitative information.

The accuracy of measurement was investigated using computer simulations, which proved that the analysis works reliably over a wide range of ventilation values, even at a pixel SNR as low as 10. Given the experimental conditions in the present small animal study, we estimate the relative uncertainty of the measured ventilation values to be 5% or better. Thus, observed regional changes in the ventilation parameter reflect true physiological differences and not measurement artifacts. The robustness of the method permits a "pixel by pixel" evaluation, i.e., a quantification of ventilation on a submillimeter scale.

In these initial experiments, images of a single slice of the lungs were acquired, yet an extension to multislice or 3D images can be envisaged. In animal studies, such imaging sequences will allow a comparison of anterior and posterior lung partitions, which will be especially useful for investigations of lung disease models.

ACKNOWLEDGMENTS

We thank Birgit Persson and Kerstin Thyberg for animal preparation.

REFERENCES

1. Ball WC, Stewart PB, Newsham LGS, Bates DV. Regional pulmonary function studied with xenon 133. J Clin Invest 1962;41:519–631.
2. Fazio F, Jones T. Assessment of regional ventilation by continuous inhalation of radioactive Krypton-81m. Br Med J 1975;3:673–676.
3. Valind SO, Rhodes CG, Brudin LH, Jones T. Measurements of regional ventilation and pulmonary gas volume: theory and error analysis with special reference to positron emission tomography. J Nucl Med 1991; 32:1937–1944.
4. Fazio F, Wollmer P, Lavender JP, Barr MM. Clinical ventilation imaging with In-113m aerosol: a comparison with Kr-81m. J Nucl Med 1982;23: 306–314.

5. Gur D, Drayer BP, Borovetz HS, Griffith BP, Hardesty RL, Wolfson SK. Dynamic computed tomography of the lung: regional ventilation measurements. J Comput Assist Tomogr 1979;3:749–753.
6. Herbert DL, Gur D, Shabason L, Good WF, Rinaldo JE, Snyder JV, Borovitz HS, Mancini MC. Mapping of human local pulmonary ventilation by xenon enhanced computed tomography. J Comput Assist Tomogr 1982;6:1088–1093.
7. Murphy DM, Nicewicz JT, Zabbatino SM, Moore RA. Local pulmonary ventilation using nonradioactive xenon-enhanced ultrafast computed tomography. Chest 1989;96:799–804.
8. Kauczor H-U, Hofmann D, Kreitner K-F, Nilgens H, Surkau R, Heil W, Potthast A, Knopp M, Otten EW, Thelen M. Normal and abnormal pulmonary ventilation: visualization at hyperpolarized He-3 MR imaging. Radiology 1996;201:564–568.
9. Kauczor H-U, Ebert M, Kreitner K-F, Nilgens H, Surkau R, Heil W, Hofmann D, Otten EW, Thelen M. Imaging of the lungs using 3He MRI: preliminary clinical experience in 18 patients with and without lung disease. J Magn Res Imag 1997;7:538–543.
10. De Lange EE, Mugler JP III, Brookeman JR, Knight-Scott J, Truwit JD, Teates CD, Daniel TM, Bogorad PL, Cates GC. Lung air spaces: MR imaging evaluation with hyperpolarized ^{3}He gas. Radiology 1999;210: 851–857.
11. Altes T, Froh DK, Salerno M, Cook CD, Mata J, Mugler JP III, de Lange EE, Brookeman JR. Hyperpolarized helium-3 MR imaging of lung ventilation changes following airway mucus clearance treatment in cystic fibrosis. Proc 9th Annual Meeting ISMRM, Glasgow, 2001. 9:2003.
12. Schreiber WG, Weiler N, Kauczor H-U, Markstaller K, Eberle B, Hast J, Surkau R, Großmann T, Deninger A, Hanisch G, Otten EW, Thelen M. Ultrafast MR-imaging of lung ventilation using hyperpolarized helium-3. Fortschr Röntgenstr 2000;172:129–133.
13. Saam B, Yablonskiy DA, Gierada DS, Conradi MS. Rapid imaging of hyperpolarized gas using EPI. Magn Reson Med 1999;42:507–514.
14. Salerno M, Altes TA, Brookeman JR, de Lange EE, Mugler JP III. Dynamic spiral MRI of pulmonary gas flow using hyperpolarized 3He: Preliminary studies in healthy and diseased lungs. Magn Reson Med 2001;46:667–677.
15. Eberle B, Weiler N, Markstaller K, Kauczor H-U, Deninger A, Ebert M, Großmann T, Heil W, Lauer LO, Roberts TPL, Schreiber WG, Surkau R, Dick WF, Otten EW, Thelen M. Analysis of intrapulmonary O_2 concentration by MR imaging of inhaled hyperpolarized helium-3. J Appl Physiol 1999;87:2043–2052.
16. Deninger AJ, Eberle B, Ebert M, Großmann T, Heil W, Kauczor H-U, Lauer L, Markstaller K, Otten E, Schmiedeskamp J, Schreiber W, Surkau R, Thelen M, Weiler N. Quantification of regional intrapulmonary oxygen partial pressure evolution during apnea by ^{3}He MRI. J Magn Reson 1999;141:207–216.
17. Deninger AJ, Eberle B, Bermuth J, Escat B, Markstaller K, Schmiedeskamp J, Schreiber W, Surkau R, Otten E, Kauczor H-U. Assessment of oxygen-sensitive 3He MRI using a single acquisition imaging sequence. Magn Reson Med 2002;47:105–114.
18. Möller HE, Hedlund LW, Chen XJ, Carey MR, Chawla MS, Wheeler CT, Johnson GA. Measurements of hyperpolarized gas quantities in the lung. Part III. 3He T1. Magn Reson Med 2001;45:421–430.
19. Fitzsimmons WA, Tankersley LL, Walters GK. Nature of surface-induced nuclear-spin relaxation of gaseous 3He. Phys Rev 1969;179:156–165.
20. Ganière JG. Relaxation nucléaire de He3 gazeux par des surfaces. Helv Phys Acta 1973;46:147–159.
21. Schearer LD, Walters GK. Nuclear spin-lattice relaxation in the presence of magnetic-field gradients. Phys Rev 1965;139:A1398–1402.
22. Cates GD, Schaefer SR, Happer W. Relaxation of spins due to field inhomogeneities in gaseous samples at low magnetic fields and low pressures. Phys Rev A 1988;37:2877–2885.
23. Newbury NR, Barton AS, Cates GD, Happer W, Middleton H. Gaseous 3He-3He magnetic dipolar spin relaxation. Phys Rev A 1993;48:4411–4420.
24. Saam B, Happer W, Middleton H. Nuclear relaxation of ^{3}He in the presence of O_2. Phys Rev A 1995;52:862–865.
25. Bouchiat MA, Carver TR, Varnum CM. Nuclear polarization in 3He gas induced by optical pumping and dipolar exchange. Phys Rev Lett 1960;5:373–375.
26. Walker TG, Happer W. Spin-exchange optical pumping of noble-gas nuclei. Rev Mod Phys 1997;69:629–642.
27. Gudbjartsson H, Patz S. The Rician distribution of noisy MRI data. Magn Reson Med 1995;34:910–914.
28. Henkelman RM. Measurement of signal intensities in the presence of noise in MR images. [erratum published in Med Phys 1986;13:544]. Med Phys 1985;12:232–233
29. Durand E, Guillot G, Vattolo D, Darrasse L, Bittoun J, Nacher PJ, Tastevin G. Blood oxygen desaturation while breathing pure helium. Eur Radiol 1999;9:B26.
30. Brauer R, Hogan P, Hugon M, Macdonald A, Miller K. Patterns of interaction of effect of light metabolically inert gases with those of hydrostatic pressure as such: a review. Undersea Biomed Res 1982;9: 353–396.
31. Saam B, Yablonskiy DA, Gierada DS, Conradi MS. Rapid imaging of hyperpolarized gas using EPI. Magn Reson Med 1999;42:507–514.

Paper IV

^{3}He MRI-based measurement of positional dependence of regional pulmonary ventilation in rats

Sven Månsson[1*], Anselm J. Deninger[2], Peter Magnusson[2],
Göran Pettersson[2], Lars E. Olsson[2], Per Wollmer[3], Klaes Golman[2]

[1] Dept. of Experimental Research, Malmö University Hospital, Sweden
[2] Amersham Health R&D AB, Medeon, Malmö, Sweden
[3] Dept. of Clinical Physiology, Malmö University Hospital, Sweden

[*]Correspondence to:

Sven Månsson
Department of Experimental Research
Malmö University Hospital
SE–205 02 Malmö, Sweden
Telephone: +46 (0)40 33 66 36, Telefax: +46 (0)40 33 62 07
E-mail: sven.mansson@rontgen.mas.lu.se

Abstract

A recently developed method for quantitative measurement of regional lung ventilation was employed for the study of position-dependent ventilation differences in rats. The measurement strategy used hyperpolarized ^{3}He MRI to detect the buildup of the signal intensity after a increasing number of ^{3}He breaths. A sample of six rats was studied in both supine and prone positions. Three-dimensional ventilation maps were obtained with high spatial resolution (voxel volume ~1 mm^{3}). The linear correlation between the ventilation index, defined as regional ventilation normalized by the average ventilation over the whole lung, and vertical position, was investigated. Variations in the regional distribution of ventilation, as well as of the ventilation index, could be detected depending on the position of the rats. In the supine position, the ventilation was increased at the lowest parts of the lungs, with a linear gradient of the ventilation index of -0.11 ± 0.03 cm^{-1}. In the prone position, the ventilation was more uniformly distributed, with a significantly smaller gradient of ventilation index of -0.01 ± 0.02 cm^{-1}.

Keywords: hyperpolarized gas MRI; Helium-3; lung function; regional ventilation; ventilation index.

Introduction

It is well known that the distribution of regional pulmonary ventilation depends on the posture of an air-breathing animal or human (1). This has classically been attributed to effects of gravity on pleural pressure and alveolar expansion (2). Regional ventilation values change dramatically between prone and supine body postures, with predominantly dorsal ventilation in supine position and a more uniform ventilation distribution in prone position (3-8). Oxygenation and gas exchange improve in prone position, but the exact mechanism remains unclear (1). This is not fully explained by effects of gravity, and other important factors have been suggested, e.g. dorsoventral differences in lung structure balancing out the gravitational forces in the prone position (9). Various studies have been conducted on humans and large animals like dogs, sheep and pigs (10), but no data has been available for small species like the rat.

In the past, quantitative measurements of regional lung ventilation have been obtained with invasive techniques or with radioisotope imaging (11-13), but these methods have been limited in their spatial and temporal resolution. Improved spatial resolution has been realized with xenon-enhanced computed tomography, where the ventilation is determined from the wash-in and wash-out rates of stable Xe (14,15). Using a MRI-based method, regional ventilation has been evaluated qualitatively from the variations in lung parenchyma signal when a volunteer was breathing air and pure oxygen, respectively (16).

The possibility to use hyperpolarized ^{3}He gas for magnetic resonance imaging (17-19) has opened new possibilities for the examination of lung ventilation. Mata *et al.* (20,21) qualitatively investigated the positional dependence of ventilation by imaging healthy humans in prone and supine position. In the most inferior (dependent) parts of the lung, they found local ventilation defects when a subject was imaged in supine position. These defects, which resolved when the subject was imaged in prone position, were attributed to position-dependent atalectasis (closure of small airways). Similar findings were observed in a study of healthy and asthmatic subjects by Altes *et al.* (22).

Recently, Deninger *et al.* demonstrated a quantitative method to access regional ventilation in guinea pigs with high spatial resolution (23). The method employed a mathematical model to describe the buildup of the MR signal after administering a certain number of ^{3}He breaths. Thus, the local

ventilation, defined as the relative exchange of gas per breath, could be determined with an accuracy of 2–5% and a spatial resolution better than one mm. However, the previous study (23) was limited to 2D imaging of a single slice of the lungs.

In the present study, the ^{3}He-MRI based method was used to quantify, within the entire lung volume, the regional ventilation in rats in both prone and supine position. The objective was to investigate whether position-dependent gradients of ventilation could be detected in the rat lung.

Methods

Polarization and administration of ^{3}He

^{3}He was polarized using spin-exchange optical pumping (IGI 9600 Helium Polarizer, Amersham Health, Durham, NC). A quantity of 1.1 liter was polarized to 35% within 15 hours. The hyperpolarized ^{3}He was collected in a plastic bag (volume 300 ml, Tedlar®, Jensen Inert, Coral Springs, FL) at 1 bar pressure. The bag was connected to an inhouse-built respirator, described in detail elsewhere (23).

Animal preparation

Six Sprague-Dawley rats (male, 350–400 g; breeder: M&B, Ry, Denmark) were anesthetized subcutaneously with a mixture of fluanisone/fentanyl (Hypnorm™, Janssen Animal Health, Saunderton, UK) and midazolam (Dormicum®, Hoffman-La Roche AG, Basel, Switzerland). The left jugular vein was catheterized for intravenous administration of anesthesia and a neuromuscular blocking agent (pancuronium, Pavulon®, Organon Teknika, Boxtel, the Netherlands). After tracheal intubation, the animals were placed in the MR scanner and ventilated by the respirator mentioned above. Two animals were imaged in supine position first, followed by imaging in prone position. The other four animals were imaged in prone position first. Body temperature and blood pressure were monitored continuously, and were within normal range during the experiment. The breathing rate was set to 30 breaths/minute. The peak inspiratory pressure was set to 20 mbar, resulting in tidal volumes in the range of 9–12 ml. Inspiration and expiration times were 0.5 s and 1.0 s, respectively. All experiments were approved by the local ethical committee (Malmö/Lunds djurförsöksetiska nämnd; appl. no. M4–01).

^{3}He imaging

All experiments were performed on a 2.35 T scanner (Biospec 24/30, Bruker Biospin, Ettlingen, Germany) using a birdcage RF coil (Bruker Biospin) with 72 mm diameter and 110 mm length, tunable to the Larmor frequencies of ^{1}H (100.1 MHz) and ^{3}He (76.6 MHz). Coronal, sagittal and axial proton scout images were acquired for proper localization of the ^{3}He images of the ventilation measurement.

The breathing pattern used for the experiment is shown in Figure 1. An experiment consisted of four ventilator cycles, each cycle comprising 15 air breaths followed by an increasing number of 1, 2, 3, 4 helium breaths. After the last helium inspiration, the ^{3}He image was recorded during a 3.5 s breathhold. A 3D fast low-angle shot (FLASH) sequence was employed (TR/TE/flip angle = 2.1 ms / 0.9 ms / 2.5°, FOV = $6 \times 5 \times 4.5$ cm^3, acquisition matrix = $48 \times 48 \times 24$). The images were zero-filled to a final size of $96 \times 96 \times 48$. The 3D image set was positioned to cover all parts of the lungs and the trachea. Before and after the air/^{3}He cycles sketched in Figure 1, ^{3}He reference images were obtained in order to monitor the T_1 relaxation of the hyperpolarized gas in the plastic bag. The experiment was repeated twice on each animal, in prone and supine positions, respectively.

Calculation of regional ventilation

Data analysis was carried out using software implemented in MATLAB (Math-Works, Natick, MA). First, the external relaxation time $T_{1,\mathrm{ext}}$ in the ^{3}He reservoir was computed from the decay of the average image intensity of the reference images. The regional pulmonary ventilation was then calculated from the build-up of signal intensity in the images acquired after 1, 2, 3 and 4 ^{3}He breaths, according to a method described in detail elsewhere (23). The signal intensity of images acquired after n ^{3}He breaths has been shown to vary according to

$$S(n) \propto E^{(n-1)(N+n/2)}(1-q)\sum_{k=0}^{n-1}\left(E^{n-k-1}q^k \exp\left(-\frac{p_0\tau}{\xi}\frac{q^{n-k}(1-q^k)}{1-q}\right)\right) \quad [1]$$

where τ is the duration between two breaths and $E \equiv \exp(-\tau/T_{1,ext})$. The variable q denotes the fraction of gas remaining in a given volume element (voxel) of the lungs after one breath, N the number of air breaths in each ventilator cycle, p_0 the oxygen partial pressure present within the lung prior to the first ^{3}He breath of a cycle, and ξ is a proportionality factor with a

value of approximately 2.6 bar·s at body temperature (24). The regional ventilation r, defined as the fraction of gas replaced per breath, is given by $r = 1-q$. Values of $\tau = 2$ s and $N = 15$ were used in the experiments. In the calculation, a value of $p_0 = 135$ mbar served as approximation of the intrapulmonary oxygen partial pressure (23,25,26).

A least squares fit of Eq. [1] to the signal intensities measured after the $n = \{1, \ldots, 4\}$ ventilation cycles was performed to calculate the regional ventilation parameter r in each voxel. Background pixels were excluded by selecting a threshold signal-to-noise ratio (SNR) of 20 in the last ($n = 4$) image.

Calculation of position-dependent ventilation gradients

In order to compare inter-individual results independent of absolute ventilation values, maps of the ventilation index (VI) were generated for each animal. The VI was calculated by dividing the ventilation value of each voxel by the average ventilation value of all voxels, excluding the trachea and the bronchi. The latter regions were omitted from the VI calculation by excluding all voxels with ventilation values above 0.8. Next, gradients of the VI were calculated within the entire lung by least-squares fits along the vertical direction. In other words, gradients were calculated for each column of voxels in the direction of gravity, perpendicular to the coronal plane. Depending on the position of the column (central or peripheral lung), the column contained ≤ 30 (apical region) or ≤ 40 (mid-base region) voxels, corresponding to a distance of 2.8–3.8 cm. The regional ventilation is known to decrease with increasing distance from the lung hilus (23,27), which may cause a non-linear variation of the VI as function of vertical position. For this reason, both a linear and a non-linear, quadratic fit function were evaluated:

$$\begin{aligned} &\text{a)} \quad f_1(x) = a_1 + b_1 x && \text{(linear)} \\ &\text{b)} \quad f_2(x) = a_2 + b_2(x - x_{mid}) + c_2(x - x_{mid})^2 && \text{(quadratic)} \\ &\qquad\quad x_{mid} = (x_{top} + x_{bottom})/2 \end{aligned} \qquad [2]$$

where x is the vertical position. The coordinate axis was chosen such that negative x-coordinates denote lower (inferior) parts of the lung. x_{top}, x_{bottom} and x_{mid} are the coordinates of the uppermost, lowermost and middle voxel of each column. The parameter x_{mid} was introduced to make the analysis independent of translations along the vertical coordinate axis. The linear

coefficients b_1 and b_2, respectively, were used as measures of the ventilation gradient. The linear correlation (R^2) between VI and vertical position was calculated using the original VI data points, as well as with the original VI values after subtraction of the quadratic term $c_2(x - x_{mid})^2$ (Eq. [2b]).

To increase the accuracy of the fits, all coronal planes of the VI map were smoothed by averaging a region of 5×5 voxels, and fits were only performed where ≥ 5 data points were available in the ventral-dorsal direction.

For each animal, the median values were calculated in the apical regions (covering the apex and the mid lung), in the mid-base region (mid lung to top of the diaphragm), and globally (including all voxel columns where the VI was calculated). The corresponding analysis was performed for the R^2 values, with and without subtraction of the quadratic term, as described above.

To evaluate statistically significant differences between the prone and supine positions, *p*-values were calculated using Student's paired *t*-test.

Results

Images were obtained with SNR values ranging from 35 (one ^{3}He breath) to 75 (four ^{3}He breaths). Regional ventilation values ranged from 0.2 in the peripheral regions to nearly 1 in the trachea and the major bronchi, indicating a near-complete per breath renewal of gas in the latter regions (Figure 2). In the supine position, there existed a clear tendency towards increased ventilation values in the dependent (most inferior) parts of the lung (direction indicated by arrows in Figure 2), as was discernible in the sagittal and axial ventilation maps. In the 3D ventilation maps, considerably lower values (decrease by up to ~40%) were found in the non-dependent (most superior) parts. By contrast, the sagittal and axial ventilation maps computed from images taken in prone position appear more homogeneous and depict a more uniform distribution of ventilation.

Figure 3 shows plots of the VI measured in the apical and mid-base regions of the lungs of a representative animal (#4), as a function of vertical position in both prone and supine postures. In the apical region, the variation of the VI was clearly non-linear, and the linear function (f_1) resulted in a poor fit to the data (Figure 3a and c). However, the non-linear function (f_2) resulted in a good fit. In the mid-base region, the VI data points exhibited a less curved shape, as compared with the apical regions, and both functions resulted in good fits to the data (Figure 3b and d). The coeffi-

cients b_1 for the linear fit and b_2 for the non-linear fit, respectively, were calculated to virtually identical values in all parts of the lungs, demonstrating that both types of fits yielded the same linear gradient values. The parameter b_2 was chosen to represent the ventilation gradient.

The gradient of the VI [cm^{-1}] was determined in each animal. Color-coded maps of these gradients are shown in Figure 4a. Figure 4b presents histograms of the VI gradients. For animals imaged in prone position, the VI gradients were close to zero in both apical and mid-base regions, with exception of small areas near the edges of the gradient maps, where non-zero gradients were calculated. The absence of vertical ventilation gradients is also seen in the corresponding histograms, where the distributions are centered at about 0 cm^{-1} (mean ± SD of all animals = -0.02 ± 0.01 cm^{-1}).

In supine position, more pronounced vertical VI gradients were found. In the histogram representation (Figure 4b), the distribution of ventilation gradients were centered at about -0.14 cm^{-1}. The gradients were particularly prominent in the mid-base region of the lungs (mean ± SD of all animals = -0.18 ± 0.03 cm^{-1}). The negative values of the gradients (represented by blue colors in Figure 4a) indicate the decrease of the VI towards non-dependent lung regions. In the apical regions, the magnitudes of the VI gradients were smaller (mean ± SD of all animals = -0.07 ± 0.03 cm^{-1}), but still larger than the prone-position gradients.

These observations are summarized in Table 1, which lists the calculated VI gradients in prone and supine positions, measured both globally and regionally within regions near the apex and the lung base, respectively. Significant differences of the median ventilation gradients were found in all regions of the lung ($p < 0.01$), depending on whether the animal was placed in prone or supine position.

Figure 5 shows maps of the correlation (squared correlation coefficient R^2) between VI and vertical location for prone and supine image sets. The R^2 values were calculated both using the original VI data (a), and after subtraction of the quadratic term (b). With respect to the correlation of the original data, the correlation was small ($R^2 < 0.2$) in all parts of the lungs when the animals were placed in prone position. In supine posture, a high correlation ($R^2 > 0.6$) between VI and vertical location was observed in the base and mid-base regions. In apical regions, correlation values were considerably lower ($R^2 \sim 0.3$).

Using VI data after subtraction of the quadratic term, the correlation was still low in prone position, except for some regions near the edges of the R^2-maps. In supine position, the correlation was substantially increased in the apical region (~0.3 → ~0.6). In other regions, the correlation also increased, albeit to a lesser extent. (See Table 2 and 3).

Discussion

The ventilation maps (Figure 2) show that in supine position, regional ventilation increases towards dependent parts of the lungs, whereas the maps acquired in prone position yield a more homogenous distribution of the ventilation. In other words, in supine positions, dorsal regions are better ventilated. This finding is in general agreement with results obtained in large animals (8,9) and humans (28), yet to our knowledge, the present study is the first to describe the phenomenon in an animal as small as the rat.

A previous proof-of-principle study (23) has shown that hyperpolarized ^{3}He MRI offers the possibility to assess regional lung ventilation in small animals quantitatively and with high accuracy. However, the experiments described in ref. (23) were restricted to imaging of a single coronal slice of guinea pig lungs. In the present study, the technique was employed to acquire high-resolution 3D images of rat lungs in both prone and supine postures, in order to investigate position-dependent differences in lung ventilation. An advantage of the 3D acquisition and analysis is that data from all parts of the lung are utilized. Based on the analysis made during an earlier ventilation study (23), we estimate the relative uncertainty of the calculated ventilation to be ~10% in each voxel. To reduce the effect of fluctuating ventilation data caused by the inherent measurement uncertainty, each data point was averaged over a 5×5 pixel region in the coronal plane before the ventilation gradient was calculated.

As the ratio of tidal volume and total lung volume varied in different animals, the absolute values of the ventilation differed substantially (relative scatter of mean value 20%). Therefore, the VI was computed for each animal to enable an inter-individual comparison of the results. VI is a measure of regional lung ventilation relative to global lung ventilation, excluding regions such as the trachea and the bronchi, which do not take part in the alveolocapillary gas exchange. In an automated analysis, these major gas ducts were easily omitted by excluding voxels with a ventilation parameter $r > 0.8$ (cf. Figure 2).

In several investigations, vertical pressure gradients in the lung have been expressed as linear gradients (29,30). In the present investigation, it was therefore of interest to study the linear correlation between ventilation and vertical position. Although somewhat of an oversimplification, a linear slope is an easily understood method to describe a general trend in the data. Plots of the VI as function of vertical distance (c.f. Figure 3a and c) show, however, that the data points are arranged roughly along a parabola in the apical regions. This is caused by the central parts of the lung having a higher gas exchange rate than more peripheral parts (23,27). In the mid-base region, where the voxels are located farther away from the mediastinum, this effect was less pronounced (Figure 3b and Figure 3d).

The linear component of the ventilation variation was evaluated in this study, using both 1st and 2nd order polynomial fit functions. Both polynomials yielded nearly identical values of the linear fit terms. However, the 2nd order polynomial fit opens for the possibility to separate the parabolic, gas-replacement induced variation of the VI, from purely linear variations, which may have different physiological interpretations (1). This was done by subtracting the quadratic term, $c_2(x - x_{mid})^2$, from the measured VI data points.

Different general trends were observed in prone and supine position of the subject. In the prone posture, the VI gradient is very small, with mean values scattered about zero (Figure 4b). In the supine posture, the median vertical gradients were approx. –0.10 to –0.15 cm^{-1}. Lung regions between the mid-base and the diaphragm show relatively steep gradients (~ -0.18 cm^{-1}), with a high correlation between the VI and the vertical distance. Apical regions show a much less pronounced gradients and lower correlation values. In the correlation maps (Figure 5b) some locations of high R^2 values near the edges of the lungs were found. Such spots are attributed to fitting artifacts due to accidental alignment of the limited number of data points.

After subtraction of the non-linear component of the VI, the correlation in supine position increased 2–3-fold in the apical regions, thus indicating a highly non-linear variation of the ventilation. However, in prone position the correlation was low in all parts of the lung ($R^2 < 0.4$), even after subtraction of the non-linear component. This is explained by weak or non-existent vertical ventilation gradients in prone position.

To investigate whether the calculated correlation value in a specific part of the lung was dependent on the thickness of the lung in that location, i.e., on the number of data points available for the linear/non-linear fit, all correlation values > 0.6 were inserted into a histogram, as function of the lung thickness in the location where the correlation value was determined (Figure 6). In prone posture, high correlations were primarily found in regions where the lungs were thin, suggesting that these correlations result from accidental alignment of a small number of data points. In supine posture, high correlations were found virtually independent of lung thickness. We therefore presume that gradients of ventilation can be detected in all parts of the lung.

The measured vertical ventilation gradients in this study (Table 1) were within similar range with results obtained using other modalities. Gradients of regional ventilation in animals have previously been quantified, e.g. by Robertson *et al.* (27) and Marcucci *et al*. (8). In the latter study, gradients of the VI were investigated in dogs, using xenon-enhanced CT. In their study, a vertical gradient of the VI was measured to be $-0.07\ cm^{-1}$, globally, in supine position, and to be $-0.008\ cm^{-1}$ in prone position. The corresponding values obtained in the present small animal study were $-0.11\ cm^{-1}$ and $-0.01\ cm^{-1}$, respectively. Both studies thus indicated that ventilation gradients were present in supine position, but virtually absent in prone position.

Conclusions

Hyperpolarized ^{3}He was used for quantification of regional lung ventilation in rats, employing 3D imaging with high spatial resolution. Regional ventilation gradients along the vertical direction could be measured in the rat lung, when the animal was placed in the supine position, whereas these gradients were significantly smaller, and close to zero, in prone position. These results are similar to findings reported in larger animals, but have not previously been observed in animals as small as the rat. The method could provide a novel alternative to other techniques, such as xenon-enhanced CT, for ventilation investigations with high spatial resolution.

Acknowledgements

The authors thank Kerstin Thyberg and Birgit Persson for their technical assistance.

References

1. Mure M, Domino KB, Lindahl SG, Hlastala MP, Altemeier WA, Glenny RW. Regional ventilation-perfusion distribution is more uniform in the prone position. *J Appl Physiol* 2000;88:1076–1083.
2. Milic-Emili J. Ventilation. In: West JB, editor. Regional differences in the lung. New York: Academic Press; 1977. p 167–199.
3. Hoffman EA. Effect of body orientation on regional lung expansion: a computed tomographic approach. *J Appl Physiol* 1985;59:468–480.
4. Hoffman EA, Ritman EL. Effect of body orientation on regional lung expansion in dog and sloth. *J Appl Physiol* 1985;59:481–491.
5. Yang QH, Kaplowitz MR, Lai-Fook SJ. Regional variations in lung expansion in rabbits: prone vs. supine positions. *J Appl Physiol* 1989;67:1371–1376.
6. Wilson TA, Beck KC. Contributions of ventilation and perfusion inhomogeneities to the VA/Q distribution. *J Appl Physiol* 1992;72:2298–2304.
7. Pelosi P, D'Andrea L, Vitale G, Pesenti A, Gattinoni L. Vertical gradient of regional lung inflation in adult respiratory distress syndrome. *Am J Respir Crit Care Med* 1994;149:8–13.
8. Marcucci C, Nyhan D, Simon BA. Distribution of pulmonary ventilation using Xe-enhanced computed tomography in prone and supine dogs. *J Appl Physiol* 2001;90:421–430.
9. Treppo S, Mijailovich SM, Venegas JG. Contributions of pulmonary perfusion and ventilation to heterogeneity in V(A)/Q measured by PET. *J Appl Physiol* 1997;82:1163–1176.
10. Mure M, Lindahl SG. Prone position improves gas exchange--but how? *Acta Anaesthesiol Scand* 2001;45:150–159.
11. Ball WC, Stewart PB, Newsham LGS, Bates DV. Regional pulmonary function studied with Xenon-133. *J Clin Invest* 1962;41:519–531.
12. Bunow B, Line BR, Horton MR, Weiss GH. Regional ventilatory clearance by xenon scintigraphy: a critical evaluation of two estimation procedures. *J Nucl Med* 1979;20:703–710.
13. Berdine GG, Lehr JL, McKinley DS, Drazen JM. Nonuniformity of canine lung washout by high-frequency ventilation. *J Appl Physiol* 1986;61:1388–1394.

14. Gur D, Drayer BP, Borovetz HS, Griffith BP, Hardesty RL, Wolfson SK. Dynamic computed tomography of the lung: regional ventilation measurements. *J Comput Assist Tomogr* 1979;3:749–753.

15. Gur D, Shabason L, Borovetz HS, Herbert DL, Reece GJ, Kennedy WH, Serago C. Regional pulmonary ventilation measurements by xenon enhanced dynamic computed tomography: an update. *J Comput Assist Tomogr* 1981;5:678–683.

16. Edelman RR, Hatabu H, Tadamura E, Li W, Prasad PV. Noninvasive assessment of regional ventilation in the human lung using oxygen-enhanced magnetic resonance imaging. *Nat Med* 1996;2:1236–1239.

17. Ebert M, Grossmann T, Heil W, Otten WE, Surkau R, Leduc M, Bachert P, Knopp MV, Schad LR, Thelen M. Nuclear magnetic resonance imaging with hyperpolarised ^{3}He. *Lancet* 1996;347:1297–1299.

18. MacFall JR, Charles HC, Black RD, Middleton H, Swartz JC, Saam B, Driehuys B, Erickson C, Happer W, Cates GD, Johnson GA, Ravin CE. Human lung air spaces: potential for MR imaging with hyperpolarized ^{3}He. *Radiology* 1996;200:553–558.

19. Middleton H, Black RD, Saam B, Cates GD, Cofer GP, Guenther R, Happer W, Hedlund LW, Johnson GA, Juvan K, et al. MR imaging with hyperpolarized ^{3}He gas. *Magn Reson Med* 1995;33:271–275.

20. Mata JF, Altes TA, Christopher JM, Mugler JP, 3rd, Brookeman JR, de Lange EE. Positional dependence of small inferior ventilation defects seen on hyperpolarized helium-3 MR of the lung. In: Proc ISMRM, Glasgow, 2001. p 949.

21. Mata JF, Altes TA, Christopher JM, Mugler JP, 3rd, Brookeman JR, de Lange EE. Transient, position dependent ventilation defects of the lung in healthy volunteers: demonstration with hyperpolarized helium-3 MR imaging. In: Proc ISMRM, Honolulu, 2002. p 2027.

22. Altes TA, Powers PL, Knight-Scott J, Rakes G, Platts-Mills TA, de Lange EE, Alford BA, Mugler JP, 3rd, Brookeman JR. Hyperpolarized 3He MR lung ventilation imaging in asthmatics: preliminary findings. *J Magn Reson Imaging* 2001;13:378–384.

23. Deninger AJ, Månsson S, Petersson JS, Pettersson G, Magnusson P, Svensson J, Fridlund B, Hansson G, Erjefeldt I, Wollmer P, Golman K. Quantitative measurement of regional lung ventilation using ^{3}He MRI. *Magn Reson Med* 2002;48:223–232.

24. Saam B, Happer W, Middleton H. Nuclear relaxation of ^{3}He in the presence of O_2. *Phys Rev A* 1995;52:862–865.

25. Möller HE, Hedlund LW, Chen XJ, Carey MR, Chawla MS, Wheeler CT, Johnson GA. Measurements of hyperpolarized gas properties in the lung. Part III: (3)He T(1). *Magn Reson Med* 2001;45:421–430.

26. Olsson LE, Magnusson P, Deninger AJ, Pettersson G, Åkesson P, Petersson JS, Golman K. Intrapulmonary pO_2 measured by low field MR imaging of hyperpolarized ^{3}He. In: Proc ISMRM, Honolulu, 2002. p 2021.

27. Robertson HT, Glenny RW, Stanford D, McInnes LM, Luchtel DL, Covert D. High-resolution maps of regional ventilation utilizing inhaled fluorescent microspheres. *J Appl Physiol* 1997;82:943–953.

28. Pelosi P, Caironi P, Taccone P, Brazzi L. Pathophysiology of prone positioning in the healthy lung and in ALI/ARDS. *Minerva Anestesiol* 2001;67:238–247.

29. Milic-Emili J, Henderson JA, Dolovich MB, Trop D, Kaneko K. Regional distribution of inspired gas in the lung. *J Appl Physiol* 1966;21:749–759.

30. West JB, Matthews FL. Stresses, strains, and surface pressures in the lung caused by its weight. *J Appl Physiol* 1972;32:332–345.

Table 1. Gradient of VI [cm^{-1}] for animals #1 – #6, measured globally and within regions near the apex and the lung base, respectively. All values are presented as median values. p*-values were calculated with Student's paired* t*-test. (***:* p < *0.001, **:* p < *0.01).*

	Global		Apex ➢ mid lung		Mid-base ➢ diaphragm	
animal	prone	supine	prone	supine	prone	supine
#1	–0.01	–0.11	0.01	–0.09	0.03	–0.17
#2	–0.03	–0.10	–0.04	–0.05	0.03	–0.20
#3	0.00	–0.12	0.02	–0.08	0.02	–0.18
#4	–0.03	–0.15	–0.03	–0.11	0.02	–0.20
#5	0.01	–0.05	–0.02	–0.04	0.04	–0.11
#6	–0.02	–0.14	–0.04	–0.07	0.03	–0.21
Mean	**–0.01**	**–0.11**	**–0.01**	**–0.08**	**0.03**	**–0.18**
±SD.	**±0.02**	**±0.03**	**±0.02**	**±0.03**	**±0.01**	**±0.04**
p-value		*******		******		*******

Table 2. Correlation coefficient (R^2) between VI and vertical position for animals #1 – #6, measured globally and within regions near the apex and the lung base, respectively. All values are presented as median values. p*-values were calculated with Student's paired* t*-test. (***:* p < *0.001, **:* p < *0.01).*

	Global		Apex ➢ mid lung		Mid-base ➢ diaphragm	
animal	prone	supine	prone	supine	prone	supine
#1	0.21	0.48	0.16	0.31	0.16	0.70
#2	0.19	0.46	0.08	0.21	0.14	0.70
#3	0.20	0.43	0.18	0.28	0.18	0.70
#4	0.22	0.58	0.10	0.48	0.16	0.74
#5	0.16	0.50	0.20	0.24	0.13	0.72
#6	0.23	0.52	0.16	0.30	0.17	0.71
Mean	**0.20**	**0.50**	**0.15**	**0.30**	**0.16**	**0.71**
±SD.	**±0.03**	**±0.05**	**±0.05**	**±0.09**	**±0.02**	**±0.02**
p-value		*******		******		*******

Table 3. Correlation coefficient (R^2) between VI after subtraction of the quadratic term (Eq. [2]b) and vertical position for animals #1 – #6, measured globally and within regions near the apex and the lung base, respectively. All values are presented as median values. p*-values were calculated with Student's paired* t*-test. (***:* p < *0.001, **:* p < *0.01).*

	Global		Apex ➢ mid lung		Mid-base ➢ diaphragm	
animal	prone	supine	prone	supine	prone	supine
#1	0.38	0.70	0.31	0.61	0.27	0.86
#2	0.34	0.70	0.24	0.50	0.23	0.83
#3	0.35	0.68	0.44	0.60	0.24	0.82
#4	0.37	0.78	0.30	0.78	0.26	0.87
#5	0.33	0.67	0.42	0.48	0.25	0.87
#6	0.45	0.72	0.44	0.53	0.33	0.87
Mean	**0.37**	**0.71**	**0.36**	**0.58**	**0.26**	**0.85**
±SD.	**±0.04**	**±0.04**	**±0.09**	**±0.11**	**±0.04**	**±0.02**
p-value		*******		******		*******

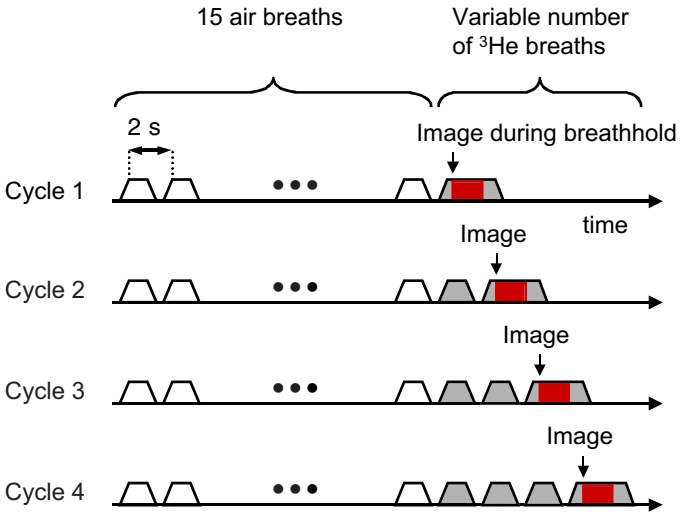

Figure 1. Illustration of breathing pattern and image acquisition. Each ventilator cycle consisted of 15 air breaths followed by an increasing number of 1, 2, 3 or 4 ^{3}He breaths. Imaging was performed during inspiratory apnea after the last ^{3}He breath of a cycle.

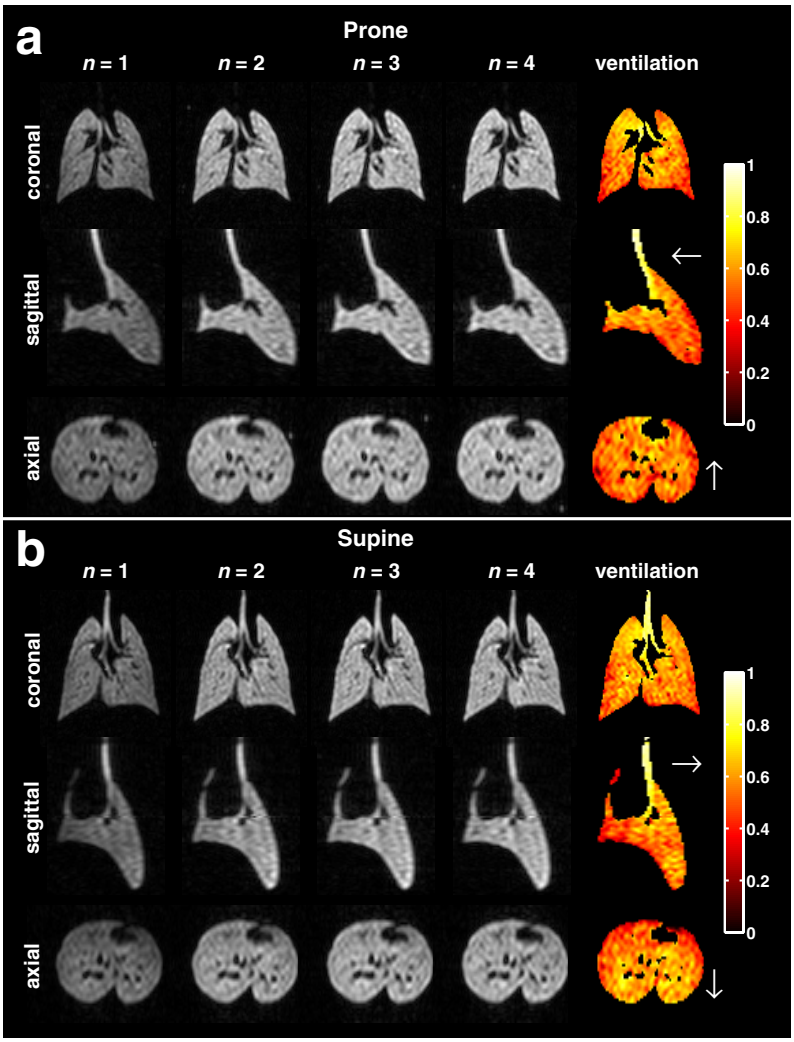

Figure 2. Coronal, sagittal and axial slices from 3D acquisitions after *n* helium breaths in prone (a) and supine (b) postures (animal #4). The rightmost column shows the regional ventilation map calculated from the four columns on the left. The arrows indicate the dependent direction. In supine position, higher ventilation in the dependent parts can be seen in the sagittal and axial ventilation maps.

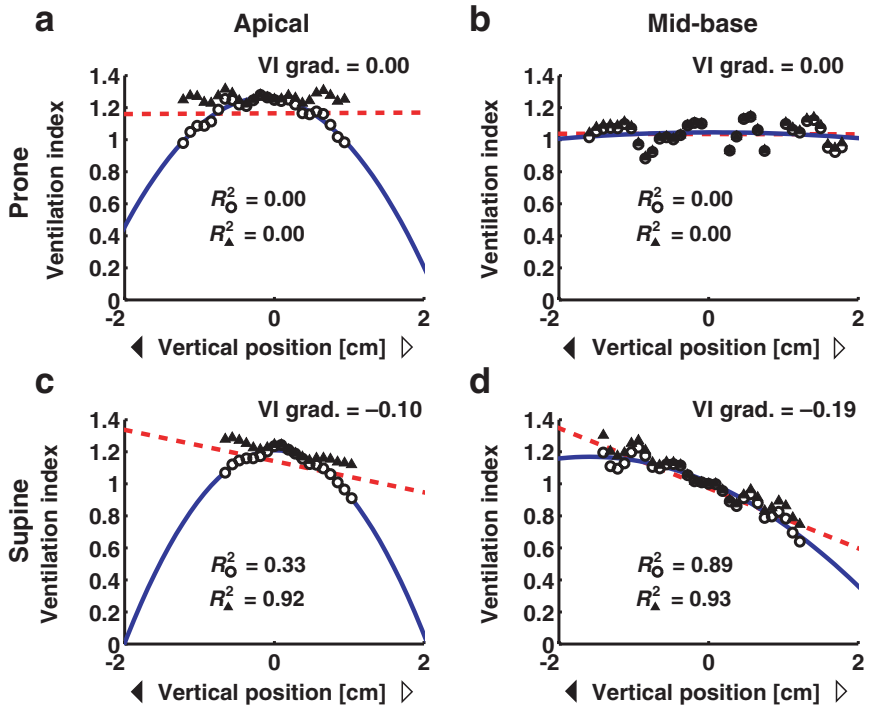

Figure 3. Representative plots of VI as function of vertical position in prone position (a–b) and in supine position (c–d). (◀ = dependent, ▷ = non-dependent). The solid lines show the non-linear fit, f_2, to the VI data (O). The dashed lines show the linear fit, f_1. The triangles (▲) show the VI data points after subtraction of the quadratic term. The linear correlation is expressed by the parameter R^2 for both sets of points (O and ▲), respectively.

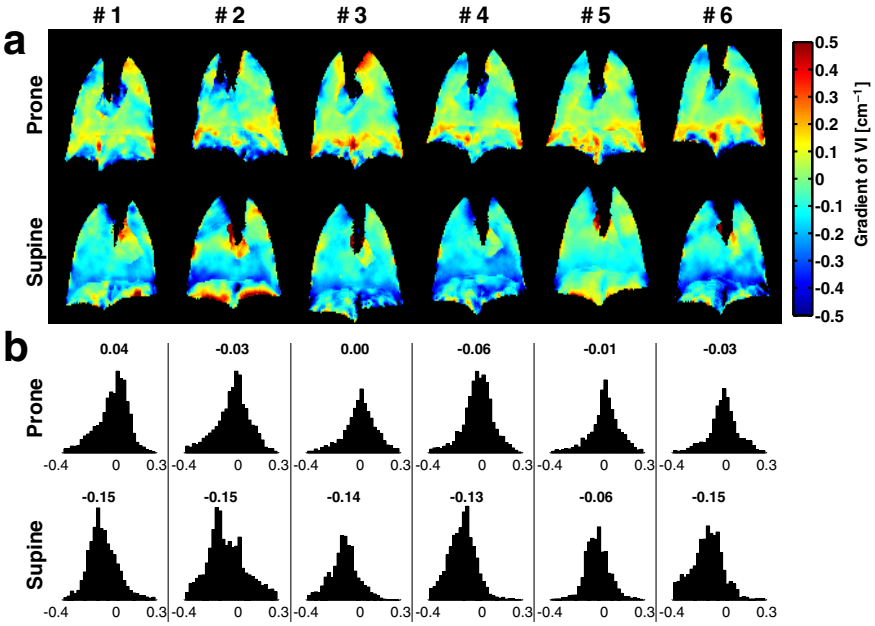

Figure 4. Color coded representations of the vertical gradient [cm^{-1}] of the VI for animals #1 to #6 (a). Histograms of the gradients are shown in (b). Blue areas and negative values on the histogram horizontal axis, respectively, correspond to regions where the ventilation is increased in the dependent parts of the lung. The numbers above each histogram indicate the position of the maximum amplitude.

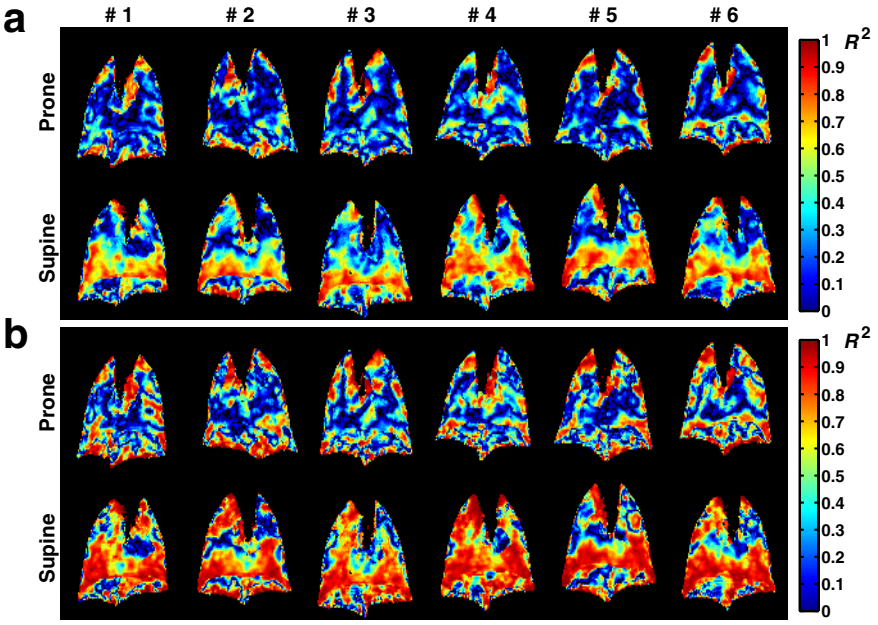

Figure 5. Maps of linear correlation (R^2-maps) between VI and vertical position in animals #1 to #6. (a) shows the R^2 value for the original VI data points, (b) shows the R^2-value after subtraction of the quadratic term.

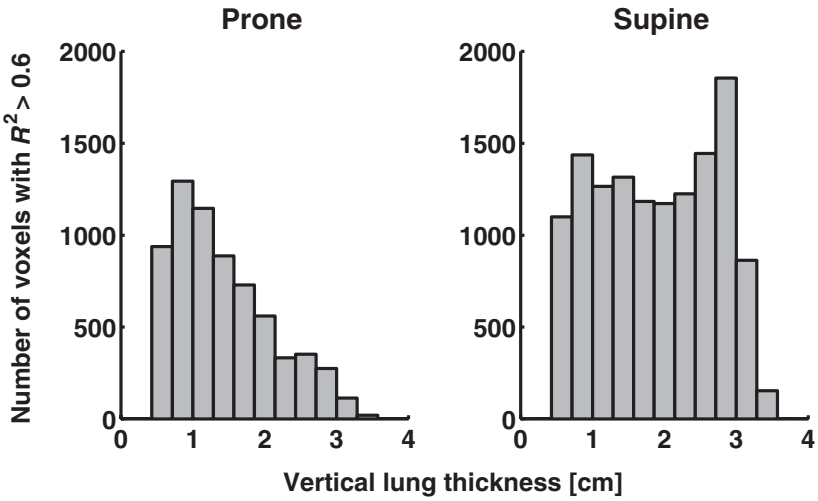

Figure 6. Distribution of significant VI gradients as a function of lung thickness. The histograms show the number of voxel columns (data from all animals) with a large correlation of the linear fit ($R^2 > 0.6$), as a function of vertical lung extension. Left: In prone position, high correlations are only found for fits including a limited number of data points, i.e. correlations tend to be accidental. Right: In supine position, significant correlations are found in all lung regions, independent of lung thickness, indicating the presence of VI gradients.

Paper V

Characterization of diffusing capacity and perfusion of the rat lung in a lipopolysaccaride disease model using hyperpolarized ^{129}Xe

Sven Månsson[1*], Jan Wolber[2], Bastiaan Driehuys[3],
Per Wollmer[4], Klaes Golman[2]

[1] Dept. of Experimental Research, Malmö University Hospital, Sweden
[2] Amersham Health R&D AB, Medeon, Malmö, Sweden
[3] Amersham Health, Durham, NC, USA
[4] Dept. of Clinical Physiology, Malmö University Hospital, Sweden

[*]Correspondence to:

Sven Månsson
Department of Experimental Research
Malmö University Hospital
SE–205 02 Malmö, Sweden
Telephone: +46 (0)40 33 66 36, Telefax: +46 (0)40 33 62 07
E-mail: sven.mansson@rontgen.mas.lu.se

Abstract

The ability to quantify pulmonary diffusing capacity and perfusion using dynamic hyperpolarized ^{129}Xe NMR spectroscopy is demonstrated. A model of alveolar gas exchange was developed, which, in conjunction with ^{129}Xe NMR, enables quantification of average alveolar wall thickness, pulmonary perfusion, capillary diffusion length and mean transit time. The technique was employed to compare a group of naïve rats ($n = 10$) with a group of rats with acute inflammatory lung injury ($n = 10$), caused by instillation of lipopolysaccaride (LPS). The measured structural and perfusion-related parameters were in agreement with reported values from studies using non-NMR methods. Significant differences between the groups were found in total diffusion length (control $8.6 \pm 0.5\ \mu$m, LPS $10.0 \pm 0.8\ \mu$m, $p < 0.001$) and in average alveolar wall thickness (control $4.9 \pm 0.9\ \mu$m, LPS $6.4 \pm 1.2\ \mu$m, $p < 0.01$), whereas no differences were observed in the perfusion-related parameters. These results demonstrate the ability of the method to distinguish two main aspects of lung function, namely diffusing capacity and pulmonary perfusion.

Keywords: hyperpolarized gas NMR; Xenon-129, lung function, diffusing capacity, pulmonary perfusion

Introduction

Gas transfer from ambient air to the blood involves different transport mechanisms. Alveolar ventilation is accomplished by convective transport. Gas transfer within the alveolus and from the alveolus into the blood stream occurs by diffusion along concentration gradients. The blood is then transported from the lungs to peripheral tissues by convective transport. These transport processes are affected by a number of lung diseases. Convective transport in the airways is thus impaired in obstructive lung diseases (1). Diffusion impairment occurs in interstitial lung diseases as well as in pulmonary edema (2). The pulmonary vasculature is affected by both primary lung disease and by left heart failure, causing abnormalities in blood flow (3).

The most common method of assessment of diffusion in the alveolar-capillary unit is measurement of the diffusing capacity for carbon monoxide, $D_{L_{CO}}$ (4). The tracer gas carbon monoxide diffuses across the alveolar-capillary barrier and is tightly bound to hemoglobin in the erythrocytes. In addition to factors determining diffusion, e.g., the available surface area and the diffusion path length, $D_{L_{CO}}$ therefore depends also on the availability of binding sites, i.e. on hemoglobin concentration and on perfusion. $D_{L_{CO}}$ provides information about diffusion properties of the lung as a whole, but no regional information about function is obtained. By measurement at different partial pressures for oxygen, $D_{L_{CO}}$ can be subdivided into the membrane conductance and a term reflecting the availability of binding sites. This is, however, not generally done in clinical routine practice. Ideally, a tracer gas for the study of lung function should enable the direct measurement of both membrane conductance and of pulmonary perfusion.

The use of hyperpolarized gases, notably ^{3}He, has made it possible to generate high-resolution gas-phase MR images in animal and human lungs. In addition to merely imaging the gas distribution in the lungs, it has been demonstrated that information about the alveolar microstructure can be obtained by diffusion-weighted ^{3}He MRI (5), and that carefully designed imaging protocols allow quantitative measurement of partial oxygen pressure in the alveoli (6) and of lung ventilation (7). The poor solubility of helium in blood and tissues precludes its use to measure perfusion ($\dot{Q}$) and therefore either contrast agent-enhanced methods or the so-called arterial spin tagging method must be employed to assess $\dot{Q}$ by ^{1}H MRI (8,9). This measurement complements the ^{3}He ventilation study, and it is possible to combine venti-

lation and perfusion information by co-registering the respective MR images.

Hyperpolarized ^{129}Xe (HpXe) provides an opportunity to quantify the amounts of xenon in pulmonary membrane and blood by means of *in vivo* NMR spectroscopy. Xenon is soluble in blood and tissues, and binds to hemoglobin in the erythrocytes (10). The alveolar gas, and the xenon in tissue and in the blood cells can be easily distinguished in *in vivo* NMR spectra due to the large chemical shift range of ^{129}Xe (11). Ruppert *et al.* have shown that the xenon uptake dynamics can be studied by NMR spectroscopy (12), and that parametric maps of the alveolar-dissolved phase exchange efficiency can be obtained by employing the so-called Xenon Transfer Contrast (XTC) technique (13). These properties make HpXe a potentially unique probe for the non-invasive and rapid assessment of pulmonary diffusion capacity.

In the present work, a diffusion model is presented which enables the quantification of a wealth of lung physiological parameters from the uptake dynamics of HpXe. In order to investigate alterations of the calculated physiological parameters under normal versus abnormal lung status, the uptake of HpXe was measured using NMR spectroscopy in healthy rats and in rats with acute inflammatory lung injury after instillation of lipopolysaccaride (LPS) (14).

Theory

The uptake of HpXe from the alveolar gas space to the blood was modeled with a three-compartment model with spherical symmetry (Fig. 1). In this single-alveolar model, xenon diffuses from the alveolus through a tissue compartment with thickness L_t. After passing the tissue compartment, the xenon diffuses an average distance L_c within a capillary compartment, consisting of plasma and red blood cells. Finally, the xenon is transported away from the capillary compartment with a flow F.

Since the alveolar radius, r_a, is an order of magnitude larger than the thickness of the tissue and capillary layers, the 1-dimensional diffusion equation (Fick's law) applies, also used in other models of alveolar diffusion (15):

$$D\frac{\partial^2 C(r,t)}{\partial r^2} - \frac{\partial C(r,t)}{\partial t} = 0 \qquad [1]$$

The diffusion coefficient, D, of xenon is assumed equal in the tissue and the capillary, with a value of approx. $1 \cdot 10^{-9}$ m^2 s^{-1} (16). The boundary conditions to Eq. [1] are given by the mass-transport laws across the compartment surfaces and the respective solubility for xenon:

$$\left.\begin{aligned} C_t(r_a,t) &= \lambda_T C_a(t) \\ A_a D \frac{\partial C_t(r_a,t)}{\partial r} &= V_a \frac{\partial C_a(t)}{\partial t} \end{aligned}\right\} \quad \text{(alveol - tissue boundary)}$$

$$\left.\begin{aligned} \lambda_P C_c(r_1,t) &= C_t(r_1,t) \\ \frac{\partial C_c(r_1,t)}{\partial r} &= \frac{\partial C_t(r_1,t)}{\partial r} \end{aligned}\right\} \quad \text{(tissue - capillary boundary)}$$

$$A_a D \frac{\partial C_c(r_2,t)}{\partial r} = -F C_c(r_2,t) \quad \text{(outer capillary boundary)} \qquad [2]$$

$$r_1 = r_a + L_t, \qquad r_2 = r_1 + L_c, \qquad A_a = 4\pi r_a^2, \qquad V_a = \tfrac{4}{3}\pi r_a^3$$

where C_a, C_t and C_c denote the concentrations in the alveolar, tissue and blood compartments, respectively. λ_T is the Ostwald solubility coefficient in tissue, and λ_P is the tissue-blood partition coefficient. Based on reported measurements of xenon solubility in various tissues (17,18), we have used $\lambda_T = 0.10$ and $\lambda_P = 0.75$. A numerical solution of Eq. [1] with the boundary conditions given by Eq. [2] is shown in Fig. 2.

When λ_P is near unity, the calculations can be simplified by ignoring the boundary conditions at the tissue-capillary surface and treating the tissue and capillary compartments as a single compartment with concentration $C(r,t)$ and thickness $L = L_t + L_c$. The condition at the outer boundary is replaced with

$$\lambda_P A_a D \frac{\partial C(r_2,t)}{\partial r} = -F C(r_2,t). \qquad [3]$$

This simplification will still yield the exact solution if $\lambda_P = 1$, and the error is small if λ_P is close to 1. It is convenient to make a transformation of variables according to $\tilde{r} = \frac{\pi}{L}(r - r_a)$, $0 \le \tilde{r} \le \pi$ and $\tilde{t} = D(\frac{\pi}{L})^2 t$, $\tilde{t} \ge 0$. After the transformation of variables, Eq. [1] has the general solution

$$C(\tilde{r},\tilde{t}) = \exp(-\chi^2 \tilde{t})\left(A \sin(\chi \tilde{r}) + B \cos(\chi \tilde{r})\right). \qquad [4]$$

Applying the conditions at the inner and outer boundaries ($\tilde{r} = 0$ and $\tilde{r} = \pi$) to Eq. [4] yields that χ must satisfy the equation

$$Lr_a(12\pi r_a D\lambda_P\lambda_T + F)\pi\chi\tan(\pi\chi) + 4\pi D r_a^3\lambda_P(\pi\chi)^2 - 3FL^2\lambda_T = 0. \quad [5]$$

Since Eq. [5] has an infinite number of roots χ_0, χ_1, χ_2, …, the full solution to Eq. [1] can be expressed as the linear combination

$$C(\tilde{r},\tilde{t}) = \sum_{n=0}^{\infty}\varphi_n\exp(-\chi_n^2\tilde{t})\left(A\sin(\chi_n\tilde{r}) + B\cos(\chi_n\tilde{r})\right) \quad [6]$$
$$\chi_0 < \chi_1 < \chi_2 < \ldots$$

where the coefficients φ_n are chosen such that the initial condition at $\tilde{t} = 0$ is fulfilled. The longest time constant ($1/\chi_0^2$) depends mainly on the alveolar radius, r_a, and the blood flow, F, and can be shown to be of the order of minutes, i.e. about two magnitudes longer than the time-scale of the measurement. The remaining roots χ_1, χ_2, … represent the transients occurring before equilibration of the concentration. Without flow (i.e. if $F = 0$), Eq. [5] simplifies to

$$\frac{r_a}{L}\pi\chi + 3\lambda_T\tan(\pi\chi) = 0. \quad [7]$$

If $r_a/L >> 1$, the roots are approximately $\chi_1 \approx 1/2$, $\chi_2 \approx 3/2$, $\chi_3 \approx 5/2$, … . The exponential terms $\exp(-\chi_n^2\tilde{t})$ will thus, after transformation to the original variables r and t, correspond to exponential terms $\exp(-t/\tau_n)$, with $\tau_n^{-1} = \chi_n^2 D(\frac{\pi}{L})^2$. Because the time constant τ_1 easily can be determined experimentally, it follows that the total thickness of the tissue and capillary compartments can be estimated according to:

$$L \approx \frac{\pi}{2}\sqrt{D\tau_1}. \quad [8]$$

By comparing with a direct, numerical solution of Eq. [1], the error in the L value estimated from Eq. [8] is <10% for a wide range of pulmonary blood flows (Fig. 3).

The xenon in the capillary compartment can be divided in a fraction H inside the red blood cells, and a fraction ($1 - H$) dissolved in the plasma, where H denotes the hematocrit. After the transient buildup, the concentra-

tions in tissue, plasma and red blood cells can be considered independent of the *r*- and *t*-coordinates and proportional to the respective Ostwald solubility: $C_t = \alpha\lambda_T$, $C_{pl} = \alpha\lambda_{pl}$, $C_{RBC} = \alpha\lambda_{RBC}$. The NMR signals coming from tissue, plasma and red blood cells can then be expressed as

$$\begin{aligned} S_{tissue}(t) &= \alpha\lambda_T A_a L_t \\ S_{plasma}(t) &= \alpha\lambda_{pl} A_a L_c (1-H) + \int_0^t (1-H) F\alpha\lambda_{pl}\, d\tau \\ S_{RBC}(t) &= \alpha\lambda_{RBC} A_a L_c H + \int_0^t HF\alpha\lambda_{RBC}\, d\tau. \end{aligned} \qquad [9]$$

The integral terms in Eq. [9] represent xenon having left the capillary compartment surrounding the alveolus, but still generate signal downstream of the alveolus.

The signal S_{RBC} give rise to a separate spectral peak, whereas the positions of S_{tissue} and S_{plasma} coincide (10,19). Therefore, we assume that the observed "tissue" signal, S_t, in the present investigation is the sum of S_{tissue} and S_{plasma}:

$$\begin{aligned} &\text{"tissue" signal} && S_t(t) = S_{tissue}(t) + S_{plasma}(t) \equiv S_{t0} + S_{t1}t \\ &\text{"blood" signal} && S_b(t) = S_{RBC}(t) \equiv S_{b0} + S_{b1}t \end{aligned}$$

$$\begin{aligned} S_{t0} &= \alpha\lambda_T A_a L_t + \alpha\lambda_{pl} A_a L_c (1-H) \\ S_{t1} &= (1-H) F\alpha\lambda_{pl} \\ S_{b0} &= \alpha\lambda_{RBC} A_a L_c H \\ S_{b1} &= HF\alpha\lambda_{RBC}. \end{aligned} \qquad [10]$$

The parameters S_{t0}, S_{t1}, S_{b0} and S_{b1}, representing the intercept and slope of the asymptotes of the tissue and blood signals (see Fig. 4), are used for calculation of the tissue thickness L_t and the capillary thickness L_c:

$$L_t = \frac{S_{t0}H\lambda_{RBC} - S_{b0}\left(1-H\right)\lambda_{pl}}{S_{t0}H\lambda_{RBC} + S_{b0}\left(\lambda_T - \left(1-H\right)\lambda_{pl}\right)}L$$
$$L_c = \frac{S_{b0}\lambda_T}{S_{t0}H\lambda_{RBC} + S_{b0}\left(\lambda_T - \left(1-H\right)\lambda_{pl}\right)}L \qquad [11]$$

where L is obtained from Eq. [8].

Several important physiological quantities can be calculated from Eq. [10] — the hematocrit, H, the lung perfusion, $\dot{Q}$, given by $F/(V_t + V_c)$ and the mean transit time, M_{TT}, given by V_c/F:

$$H = \frac{S_{b1}\lambda_{pl}}{S_{t1}\lambda_{RBC} + S_{b1}\lambda_{pl}}$$
$$\dot{Q} = \frac{S_{b1}\lambda_T}{S_{b0}\left(\lambda_T - \left(1-H\right)\lambda_{pl}\right) + S_{t0}\lambda_{RBC}H} \qquad [12]$$
$$M_{TT} = \frac{S_{b0}}{S_{b1}}.$$

The relative blood volume, *rBV*, given by $M_{TT}\cdot\dot{Q}$, can therefore be expressed as L_c/L. Additionally, with the simplification that the tissue-blood partition coefficient is close to 1, we observe that the ratio between alveolar volume, V_a, and the effective total volume, $V_a + \lambda_T(V_t + V_c)$, equals the ratio $S_{a0}/S_a(0)$, where $S_a(0)$ is the gas signal at time $t = 0$ and S_{a0} is the intercept of the asymptote to the gas signal. Hence, the alveolar volume can be calculated:

$$V_a = \frac{\lambda_T S_{a0}\left(V_t + V_c\right)}{S_a\left(0\right) - S_{a0}}. \qquad [13]$$

Using the relations $V_a = \frac{4}{3}\pi r_a^3$, $A_a = 4\pi r_a^2$ and $(V_t + V_c) = A_a L$, it is then possible to calculate the alveolar radius:

$$r_a = \frac{3\lambda_T S_{a0}}{S_a\left(0\right) - S_{a0}}L \qquad [14]$$

where L is known from Eq. [8].

Methods

Polarization and administration of ^{129}Xe

^{129}Xe was polarized using a prototype commercial polarizer (IGI. 9800, Amersham Health, Durham, NC). A gas mixture of 1% natural abundance ^{129}Xe, 10% N_2 and 89% ^4He flowed at a rate of 0.9 l/min through an optical cell where the ^{129}Xe spins were polarized via spin exchange with optically pumped Rb vapor (20). HpXe was accumulated for 30 min and frozen at liquid nitrogen temperature. After thawing, the HpXe was collected in a plastic bag (volume 300 ml, Tedlar®, Jensen Inert, Coral Springs, FL) at 1 atm pressure. The polarization level in the bag was measured using a stand-alone calibration station (Amersham Health, Durham, NC) before and after each experiment in order to calculate the T_1 relaxation time within the bag during the experiment. The initial polarization level in the bag was 8%–12%.

The plastic bag containing Xe was connected to an in-house-built, computer-controlled respirator. Via a switch valve, the respirator was capable of administering either air or HpXe to the animal. The bag was placed within a rigid cylinder and positioned 0.5 m outside the magnet. To expel the polarized gas, the cylinder was pressurized with nitrogen. The computer control also served to trigger the MR sequence, i.e. to synchronize gas delivery and data acquisition. The reproducibility of administered gas volumes was tested in separate experiments and was better than 2% (data not shown).

Animal preparation

All experiments were approved by the local ethical committee (Malmö/Lunds djurförsöksetiska nämnd; appl. no. M4-01). Ten Wistar rats (male, 250–360 g; breeder: M&B, Ry, Denmark) were instilled intratracheally with 1.0 mg LPS (Sigma Chemical, St. Louis, MO) per animal, dissolved in 0.1 ml 0.9% saline. The instillation was performed 48 hours prior to the NMR examination. A group of ten untreated Wistar rats (male, 270–340 g) served as controls. The animals were anesthetized subcutaneously with a mixture of fluanisone/fentanyl (Hypnorm™, Janssen Animal Health, Saunderton, England) and midazolam (Dormicum®, Hoffman-La Roche AG, Basel, Switzerland). The left jugular vein and the right carotid artery were catheterized for intravenous administration of anesthesia and a neuromuscular blocking agent (pancuronium, Pavulon®, Organon Teknika, Boxtel, the Netherlands), and for measurement of arterial blood pressure.

After tracheal intubation, the animals were placed in the MR scanner in supine position and ventilated by the respirator mentioned above. During the experiment, body temperature, blood pressure, inspiratory pressure and tidal volume were monitored continuously. The breathing rate was set to 40 breaths/minute and the tidal volume to 1.0 ml per 100 g body weight. Inspiration and expiration times were 0.5 s.

Xenon spectroscopy

All experiments were performed on a 2.35 T scanner (BioSpec 24/30, Bruker Biospin, Ettlingen, Germany) using a double-tuned birdcage RF coil (Bruker Biospin) with 72 mm diameter and 110 mm length, operating at the Larmor frequencies of ^{1}H (100.1 MHz) and ^{129}Xe (27.7 MHz). The acquisition scheme is shown in Fig. 5. A ventilator cycle consisted of 18 air breaths followed by three xenon breaths. The breathing was interrupted after the third xenon inspiration for a 7 s breathhold and a trigger pulse was sent from the ventilator to the NMR scanner in order to initiate data accumulation. A 90° RF excitation with center frequency between the tissue and blood xenon resonances was applied in order to remove all signal arising from xenon in tissue and blood, while preserving the hyperpolarization in the alveolar gas. After a delay $\Delta(n)$, a second 90° RF excitation followed, generating a FID signal from xenon having diffused from the alveoli to tissue and blood during the delay $\Delta(n)$. During the breathhold period, the RF pulses and data accumulation were repeated 12 times in an averaging loop, before continuing with the next ventilator cycle. The ventilator cycle was repeated 12 times ($n = 1\ldots12$) with increasing values of the delay $\Delta(n)$ (15, 20, 30, 40, 60, 90, 120, 150, 200, 300, 400 and 500 ms, respectively), resulting in a total experiment duration of 8 minutes.

Before each experiment, the flip angle of the RF pulses was carefully adjusted to 90° by applying a train of 4 RF pulses with center frequency at the gas resonance. The adjustment was repeated and the amplitude of the RF pulses fine-tuned until no FID signal could be detected after pulses 2–4. With the center frequency between the tissue and blood resonances, the duration of the rectangular RF pulses was adjusted to give minimum excitation of the alveolar gas, i.e. the first zero crossing of the sinc-shaped frequency response of the RF pulse was adjusted to correspond to the gas resonance. The excitation of the gas signal was measured in a separate experiment and was found to be approximately 7° (data not shown).

Parametric analysis

The data analysis was made with software implemented in MATLAB (MathWorks, Natick, MA). After zero and first order phase corrections, Lorentzian shape functions were fitted to the gas, tissue and blood peaks of each spectrum. The peak amplitudes of the fitted functions were corrected for the T_1 relaxation decay of the HpXe in the reservoir during the course of the experiment. Because the repetition time within the averaging loop increased with increasing delay $\Delta(n)$, the peak amplitudes were additionally corrected for the T_1 relaxation in the lung during the data accumulation, using a fixed T_1 relaxation of 30 s in the gas phase (21). The functions

$$\begin{aligned} S_g(\Delta) &= S_{0,g}\exp(-\Delta/\tau_g) + S_{1,g} \qquad \text{(gas peak)} \\ S(\Delta) &= S_0\left(1-\exp(-\Delta/\tau_1)\right) + S_1\Delta \qquad \text{(tissue and blood peaks)} \end{aligned} \quad [15]$$

were fitted to the amplitudes of the gas, tissue and blood peaks, as function of the delay Δ. The resulting time constant τ_1 from the tissue peak was used for calculation of the total diffusion length (L, Eq. [8]). The intercept, S_0, and slope, S_1, from the tissue and blood peaks were used to calculate L_t, L_c, $\dot{Q}$ and M_{TT}, according to Eqs. [11] and [12]. These calculations were performed using Ostwald solubility coefficients $\lambda_T = 0.1$, $\lambda_{pl} = 0.09$, $\lambda_{RBC} = 0.2$ (18) and a fixed hematocrit $H = 0.45$ (22,23). Additionally, the alveolar radius was estimated using Eq. [14] and the relative blood volume was calculated as $rBV = L_c/L$. p-values, comparing the LPS-treated group with the controls, were calculated using the Student's t-test (double-sided, unequal variance).

Results

Xe spectroscopy

In all spectra, gas, tissue, and blood signals were clearly visible with tissue signal SNR ranging from 20 (shortest delay Δ) to 80 (longest delay Δ). The tissue and blood signals were well separated at 198 ppm and 212 ppm respectively, with amplitudes approximately half of the gas signal amplitude. The T_1 relaxation of xenon in the reservoir was in the range 60–80 min, corresponding to a maximum signal decay of about 0.9 during the experiment. A representative set of spectra is shown in a stacked plot (Fig. 6).

Parametric analysis

The fit of the functions given by Eq. [15] to the tissue, blood, and gas amplitudes yielded R^2 values of 0.98 ± 0.02 (tissue), 0.99 ± 0.02 (blood) and 0.95 ± 0.04 (gas) in the control group (mean ± SD). In the LPS-treated group, the corresponding values were 0.99 ± 0.02, 0.97 ± 0.09 and 0.90 ± 0.09, respectively. A representative example of the fit is presented in Fig. 7.

In the control group, the time constant τ_1 was determined to 30 ± 3 ms using the tissue signal and to 26 ± 5 ms using the blood signal. The ratio of the tissue and blood time constants was 1.17 ± 0.23. In the LPS-treated group, the corresponding time constants were 41 ± 6 ms (tissue) and 33 ± 10 ms (blood) with ratio 1.28 ± 0.22. Due to its lower standard deviation, the tissue time constant was selected for calculation of the total diffusion length, L. The time constant of the gas signal, τ_g, was 257 ± 137 ms in the control group and 195 ± 104 ms in the LPS-treated group.

Significant differences in total diffusion length (L) and tissue thickness (L_t) were found between the control group and the LPS-treated group, whereas no significant difference in capillary diffusion length (L_c), perfusion ($\dot{Q}$), mean transit time (M_{TT}), relative blood volume (rBV) or alveolar radius (r_a) could be detected (see Table 1).

Discussion

The pulmonary tissue compartment in the model is composed of the alveolar liquid lining, the epithelium, a very thin interstitial space, and the endothelium. The thickness of the blood-gas barrier is known to vary around the capillaries (24). However, as the ^{129}Xe NMR measurement was not spatially resolved in the present investigation, the tissue thickness calculated from the xenon uptake time-constant should be regarded as an average value for the alveolar-capillary membrane thickness, including tissue separating neighboring capillaries and perivascular interstitial space. Our measurement of the average membrane thickness agrees well with the actual dimensions of the membrane, which has been measured to 5–6 μm in the rat using microscopic methods (25) as well as with NMR techniques (26). The membrane thickness is an important indicator of the diffusing capacity of the lung, since the diffusing capacity is inversely proportional to this thickness (4). A reduced diffusing capacity caused by loss of alveolar surface area will however not be revealed by the uptake time constant. The uptake time constant

is inversely proportional to the gas diffusion coefficient. Since the diffusion coefficients are similar for xenon ($1 \cdot 10^{-9}$ m^2 s^{-1} (16)) and for oxygen ($1.7 \cdot 10^{-9}$ m^2 s^{-1} (27)), one can expect that the dynamics of the xenon uptake is not much different from that of oxygen.

Although the model is a simplification of the actual lung morphology, the experimental results agree in several respects with the predictions from the theoretical analysis. The model uses equal time constants for the initial signal buildup in both tissue and blood, which agrees with the measured "tissue" and "blood" time constants having a ratio close to unity. We have established a statistically significant difference in the Xe uptake time constant – and hence in the membrane thickness – between the control animals and the LPS-treated group of animals. The difference in length was related to the "tissue" thickness only, whereas the "capillary" thickness was equal in both groups. This finding is logical, since the acute inflammatory lung injury caused by the LPS is expected to increase the alveolar wall thickness, but not to alter the capillary blood volume within the lung.

In addition, we have shown that it is possible to measure perfusion using the xenon uptake method. The slopes and intercepts of the dissolved-phase ^{129}Xe signals after the initial exponential buildup are used for calculation of the quantities mean transit time, perfusion, and relative blood volume. Other studies on rats using non-NMR methods have reported a total pulmonary blood flow of approx. 2 ml/s (28), a total capillary volume of approx. 1 ml (29), and a total alveolar wall volume of 1 ml (29). From these data, the perfusion can be calculated to 1 $ml \cdot s^{-1}$/ml, the mean transit time to 0.5 s and the relative blood volume to 0.5, which are in fair agreement with the corresponding values obtained in the present study.

The mean transit time did not differ between the control group and the LPS group. This observation further supports the assumption that the total blood volume, and thus the "blood thickness", remained unaffected by the LPS treatment. We note that the mean transit time is one order of magnitude larger than the observed uptake time constant (30 ms in the control group, 41 ms in the LPS group). Consequently, the xenon concentrations in blood and tissue are well equilibrated before the blood leaves the alveolar capillary. The ratio between the uptake time constant and the mean transit time would thus indicate whether the gas exchange is perfusion or diffusion limited. The calculated lung perfusion and relative blood volume differed between the groups, although not significantly ($p = 0.13$ and $p = 0.19$, respectively). The tendency for reduced perfusion and relative blood volume

in the LPS-treated group is consistent with an increased total volume (tissue plus blood) in the treated group, at unaltered blood flow.

Among the calculated model parameters, the total diffusing thickness, L, is obtained directly from the uptake time constant, τ_1, in contrast to the other parameters, which rely on the slope and intercept of the uptake curves. The present study was limited by the need for several averaged accumulations in order to obtain spectra with sufficient SNR, resulting in accumulation times of several seconds for the longest delays Δ. This is undesirable, since the alveolar gas signal decreases after inspiration due to the T_1 relaxation in the lung and the transport of xenon to the capillary. The T_1 relaxation was compensated for, whereas a compensation for the signal drop caused by removal of xenon from the alveolus could not be done. Therefore, we believe that the slope and intercept values were more difficult to determine accurately than the uptake time constant, and thus that the parameter L is the most reliable measure of pathological condition. The inverse of the uptake time constant, τ_1^{-1}, is moreover expected to be a very sensitive indicator of alveolar membrane thickening, as it is a quadratic function in L. We further note that the measurement of the alveolar radius in this study (~8 μm) resulted in an underestimation compared to the expected value of about 35 μm (29). Of the measured signals during the experiment, the gas signal was the most difficult to quantify, with a more fluctuating amplitude than the tissue and blood peaks. The fluctuating signal amplitude caused difficulties to obtain reproducible results from the gas peak. We therefore believe that the current implementation of the method needs improvements before reliable measurements of the alveolar radius can be made.

In principle, the HpXe uptake study provides the same information as the CO transfer test, as both methods assess the membrane-related and the vascular aspects of lung function. The quantity obtained from the CO function test, $D_{L_{CO}}$, is a function of lung surface area, membrane thickness, and blood volume. However, the latter physiological quantities are not easily obtained from the CO transfer test. In contrast, the ^{129}Xe method enables direct quantification of the most important physiological parameters from the initial uptake dynamics of the gas. With some increase in ^{129}Xe polarization and a greater total volume of hyperpolarized gas available for the study, it may also be possible to differentiate Xe uptake in several regions of interest within the lungs by means of localized NMR spectroscopy. Another extension of the present study would be a complementary quantitative method for measuring lung ventilation using HpXe, which would open the exciting

prospect of more comprehensive characterization of lung function with a single diagnostic modality.

Conclusions

A mathematical diffusion model was derived, allowing the quantification of lung physiological parameters from the uptake dynamics of hyperpolarized ^{129}Xe, as measured by a NMR spectroscopy method. We demonstrate a simple relationship between the uptake time constant and the effective diffusion length across the respiratory membrane. Furthermore, quantitative information about pulmonary perfusion can be extracted. Thus, a major advantage of the method is that the two main components of lung function — membrane diffusing capacity and pulmonary perfusion — are obtained in a single study.

The method was employed for comparison of a control group of rats versus a group of LPS-treated rats. A statistically significant increase in the diffusion length, related to a thickening of the alveolar wall was measured in the latter group, whereas no significant differences in perfusion related parameters were observed. We therefore conclude that the proposed method is able to distinguish alterations related to diffusive capacity from alterations of pulmonary perfusion. The method may be complemented with ventilation imaging using hyperpolarized xenon, for improved diagnosis of the lung function.

Acknowledgements

The authors thank Edvin Johansson, Jonas Erjefält, PhD and Göran Pettersson, PhD for valuable suggestions, and Kerstin Thyberg and Birgit Persson for assistance during the experiments.

References

1. Alderson PO, Line BR. Scintigraphic evaluation of regional pulmonary ventilation. *Semin Nucl Med* 1980;10:218–242.
2. Puri S, Baker BL, Dutka DP, Oakley CM, Hughes JM, Cleland JG. Reduced alveolar-capillary membrane diffusing capacity in chronic heart failure. Its pathophysiological relevance and relationship to exercise performance. *Circulation* 1995;91:2769–2774.

3. Worsley DF, Palevsky HI, Alavi A. Ventilation-perfusion lung scanning in the evaluation of pulmonary hypertension. *J Nucl Med* 1994;35:793–796.

4. Roughton FJW, Forster RE. Relative importance of diffusion and chemical reaction rates in determining rate of exchange of gases in the human lung, with special reference to true diffusing capacity of pulmonary membrane and volume of blood in the lung capillaries. *J Appl Physiol* 1957;11:290–302.

5. Yablonskiy DA, Sukstanskii AL, Leawoods JC, Gierada DS, Bretthorst GL, Lefrak SS, Cooper JD, Conradi MS. Quantitative in vivo assessment of lung microstructure at the alveolar level with hyperpolarized 3He diffusion MRI. *Proc Natl Acad Sci U S A* 2002;99:3111–3116.

6. Deninger AJ, Eberle B, Ebert M, Grossmann T, Heil W, Kauczor H, Lauer L, Markstaller K, Otten E, Schmiedeskamp J, Schreiber W, Surkau R, Thelen M, Weiler N. Quantification of regional intrapulmonary oxygen partial pressure evolution during apnea by (3)He MRI. *J Magn Reson* 1999;141:207–216.

7. Deninger AJ, Månsson S, Petersson JS, Pettersson G, Magnusson P, Svensson J, Fridlund B, Hansson G, Erjefeldt I, Wollmer P, Golman K. Quantitative measurement of regional lung ventilation using ^{3}He MRI. *Magn Reson Med* 2002;48:223–232.

8. Hatabu H, Gaa J, Kim D, Li W, Prasad PV, Edelman RR. Pulmonary perfusion: qualitative assessment with dynamic contrast- enhanced MRI using ultra-short TE and inversion recovery turbo FLASH. *Magn Reson Med* 1996;36:503–508.

9. Roberts DA, Gefter WB, Hirsch JA, Rizi RR, Dougherty L, Lenkinski RE, Leigh JS, Jr., Schnall MD. Pulmonary perfusion: respiratory-triggered three-dimensional MR imaging with arterial spin tagging--preliminary results in healthy volunteers. *Radiology* 1999;212:890–895.

10. Wolber J, Cherubini A, Leach MO, Bifone A. Hyperpolarized 129Xe NMR as a probe for blood oxygenation. *Magn Reson Med* 2000;43:491–496.

11. Sakai K, Bilek AM, Oteiza E, Walsworth RL, Balamore D, Jolesz FA, Albert MS. Temporal dynamics of hyperpolarized 129Xe resonances in living rats. *J Magn Reson B* 1996;111:300–304.

12. Ruppert K, Brookeman JR, Hagspiel KD, Driehuys B, Mugler JP, 3rd. NMR of hyperpolarized (129)Xe in the canine chest: spectral dynamics during a breath-hold. *NMR Biomed* 2000;13:220–228.

13. Ruppert K, Brookeman JR, Hagspiel KD, Mugler JP, 3rd. Probing lung physiology with xenon polarization transfer contrast (XTC). *Magn Reson Med* 2000;44:349–357.

14. Beckmann N, Tigani B, Sugar R, Jackson AD, Jones G, Mazzoni L, Fozard JR. Noninvasive detection of endotoxin-induced mucus hypersecretion in rat lung by MRI. *Am J Physiol Lung Cell Mol Physiol* 2002;283:L22–30.

15. Dowse HB, Norton S, Sidell BD. The estimation of the diffusion constant and solubility of O(2)in tissue using kinetics. *J Theor Biol* 2000;207:531–541.

16. Wolber J, Santoro D, Leach MO, Bifone A. Diffusion of hyperpolarized 129Xe in biological systems: effect of chemical exchange. In: Proc 8th Annual Meeting ISMRM, Denver, 2000. p 754.

17. Andersen AM, Ladefoged J. Partition coefficient of 133-xenon between various tissues and blood in vivo. *Scand J Clin Lab Invest* 1967;19:72–78.

18. Ladefoged J, Andersen AM. Solubility of xenon-133 at 37°C in water, saline, olive oil, liquid paraffin, solutions of albumin, and blood. *Phys Med Biol* 1967;12:353–358.

19. Albert MS, Schepkin VD, Budinger TF. Measurement of 129Xe T1 in blood to explore the feasibility of hyperpolarized 129Xe MRI. *J Comput Assist Tomogr* 1995;19:975–978.

20. Driehuys B, Cates GD, Miron E, Sauer K, Walter DK, Happer W. High-volume production of laser-polarized 129Xe. *Applied Physics Letters* 1996;69:1668–1670.

21. Albert MS, Cates GD, Driehuys B, Happer W, Saam B, Springer CS, Jr., Wishnia A. Biological magnetic resonance imaging using laser-polarized 129Xe. *Nature* 1994;370:199–201.

22. Hellberg PO, Bayati A, Kallskog O, Wolgast M. Red cell trapping after ischemia and long-term kidney damage. Influence of hematocrit. *Kidney Int* 1990;37:1240–1247.

23. Penney DG, Davidson SB, Gargulinski RB, Caldwell-Ayre TM. Heart and lung hypertrophy, changes in blood volume, hematocrit and plasma

renin activity in rats chronically exposed to increasing carbon monoxide concentrations. *J Appl Toxicol* 1988;8:171–178.

24. Guazzi M. Alveolar-capillary membrane dysfunction in chronic heart failure: pathophysiology and therapeutic implications. *Clin Sci (Lond)* 2000;98:633–641.

25. Tanaka R, Al-Jamal R, Ludwig MS. Maturational changes in extracellular matrix and lung tissue mechanics. *J Appl Physiol* 2001;91:2314–2321.

26. Albertine KH. Structural organization and quantitative morphology of the lung, 1 ed. In: Cutillo AG, editor. Application of magnetic resonance to the study of the lung. New York: Futura; 1996. p 73–114.

27. Sharan M, Singh B, Singh MP, Kumar P. Finite-element analysis of oxygen transport in the systemic capillaries. *IMA J Math Appl Med Biol* 1991;8:107–123.

28. Muller B, Mannesmann G. Measurement of cardiac output by the thermodilution method in rats. II. Simultaneous measurement of cardiac output and blood pressure in conscious rats. *J Pharmacol Methods* 1981;5:29–34.

29. Altman PL, Dittmer DS. Respiration and circulation. Bethesda: Federation of american societies for experimental biology; 1971. 930 p.

Table 1. Summary of the calculated parameters using the diffusion model as described in the theory section. Values are given as mean ± SD.

Parameter	Control group	LPS group	*p*-value Control vs. LPS
Total diffusion length ($L = L_t+L_c$), μm	8.6 ± 0.5	10.0 ± 0.8	0.00013
Tissue thickness (L_t), μm	4.9 ± 0.9	6.4 ± 1.2	0.0080
Blood thickness (L_c), μm	3.6 ± 0.8	3.6 ± 1.3	0.95
Perfusion ($\dot{Q}$), ml s^{-1}/ml	1.5 ± 0.3	1.3 ± 0.2	0.13
Mean transit time (M_{TT}), s	0.30 ± 0.11	0.29 ± 0.10	0.68
Relative blood volume (rBV)	0.43 ± 0.10	0.36 ± 0.12	0.19
Alveolar radius (r_a), μm	8.7 ± 3.2	8.5 ± 2.1	0.89

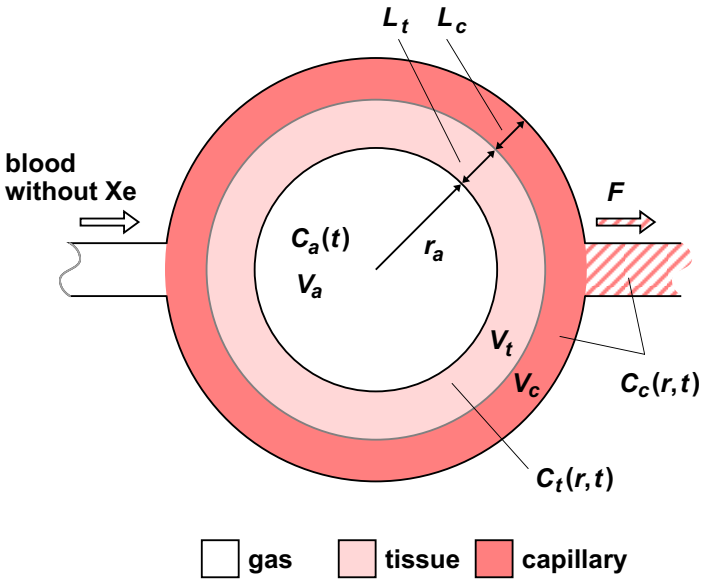

Figure 1. The single-alveolar diffusion model. F = pulmonary blood flow around the alveolus, C_a = alveolar ^{129}Xe concentration, C_t = tissue ^{129}Xe concentration, C_c = capillary ^{129}Xe concentration, L_t = tissue thickness, L_c = average diffusion length through capillary, V_a = alveolar volume, V_t = tissue volume, V_c = capillary volume around a single alveolus.

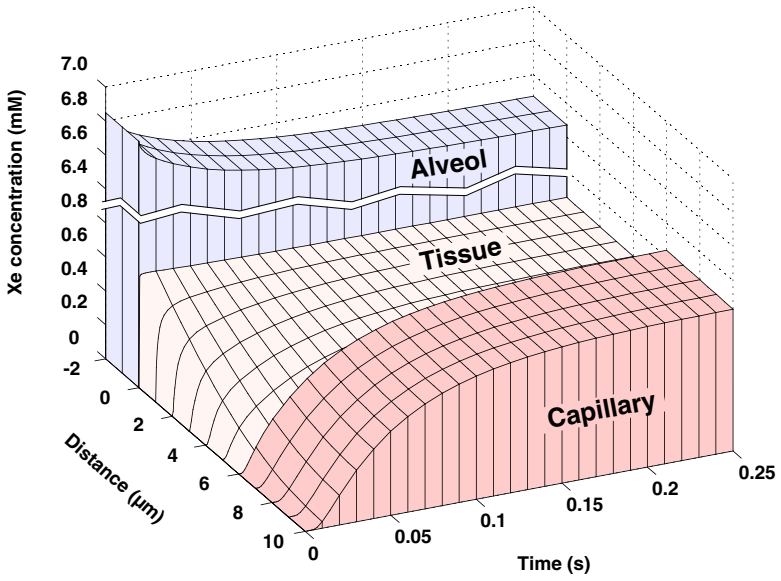

Figure 2. Numerical solution of the partial differential equation (Eq. [1]) describing the xenon concentration in the alveoli, tissue and capillary compartments.

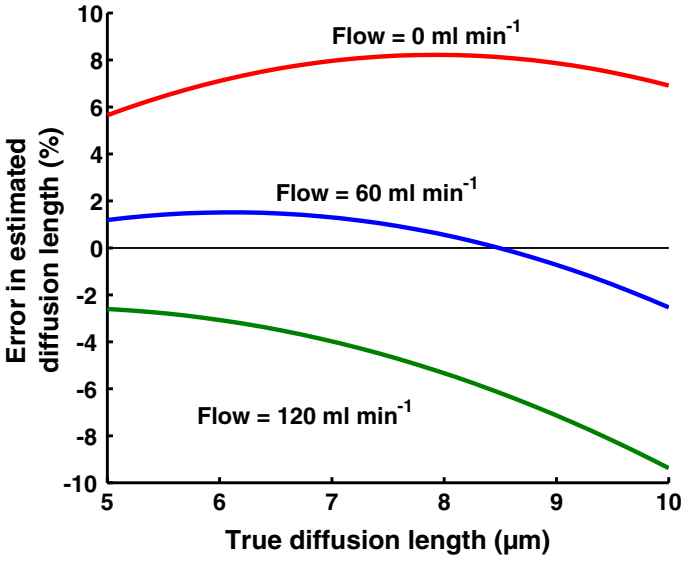

Figure 3. Error in the estimated diffusion length when using the approximate expression (Eq. [8]). For varying diffusion lengths and pulmonary blood flows, the estimated diffusion length L was calculated according to Eq. [8], using the true time constant τ_1 obtained from a numerical solution of Eq. [1]. The total pulmonary blood flow was equally distributed across a total of $1 \cdot 10^6$ alveoli.

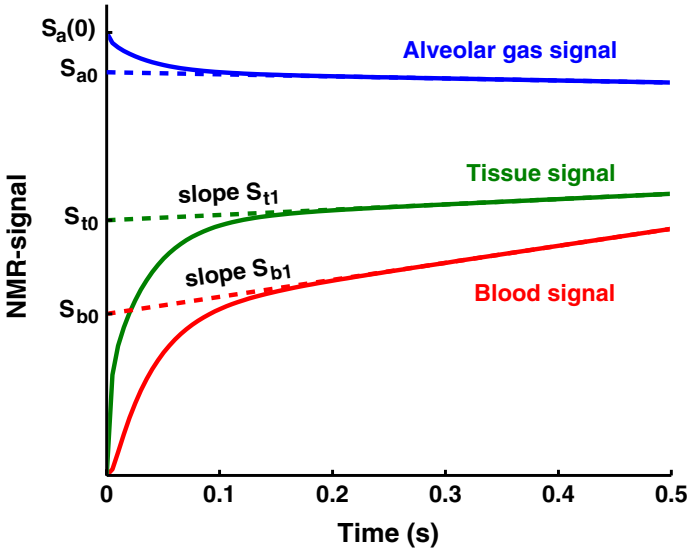

Figure 4. Illustration of the acquired NMR signals and the parameters needed for calculation of tissue thickness, capillary thickness, perfusion, mean transit time and alveolar radius.

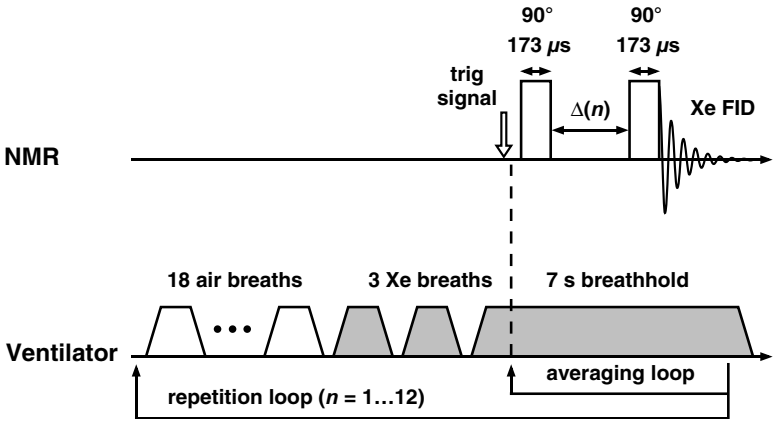

Figure 5. Schematics of the ventilator operation and NMR data acquisition. A repetition cycle consisted of 18 air breaths followed by 3 xenon breaths. After the last xenon inspiration, a 90° RF pulse was applied to destroy the signal in tissue and blood, followed by a second 90° RF pulse generating a FID from the xenon in tissue and blood. The interpulse delay $\Delta(n)$ was increased between successive repetitions.

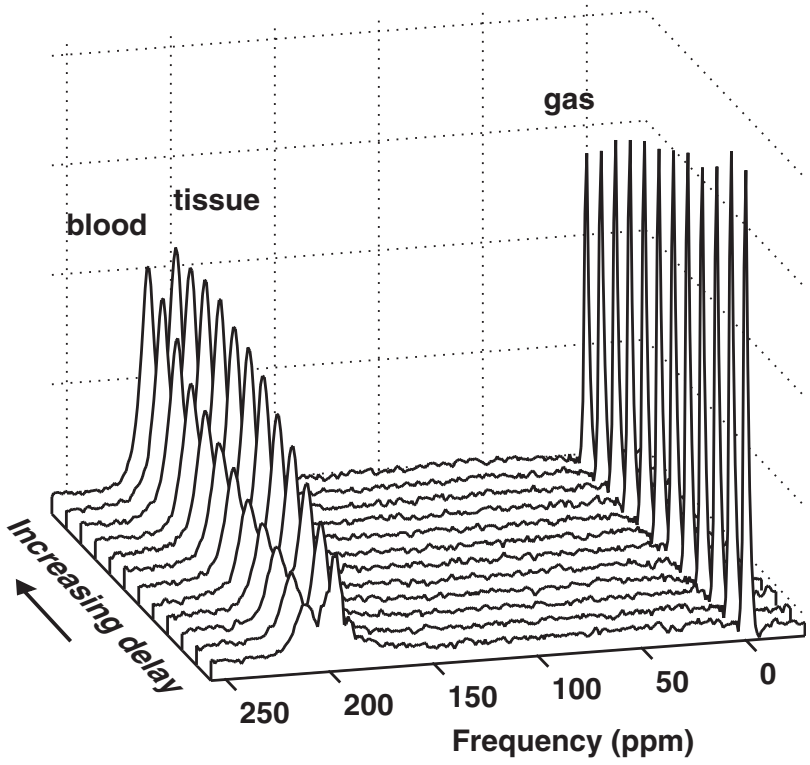

Figure 6. A representative set of spectra obtained from a naïve rat. The 12 spectra correspond to increasing delays Δ, during which the xenon diffuses from the alveoli to the capillaries. The decreasing amplitude of the alveolar gas signal due to the uptake of xenon is readily observable.

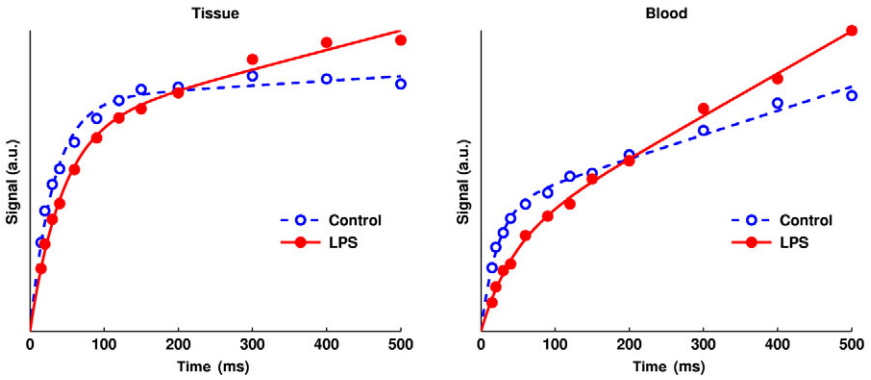

Figure 7. The peak amplitudes (circles) of tissue and blood xenon signals in a representative control animal and a LPS-treated animal, as function of the delay time Δ. The solid and dashed lines show the fit of Eq. [15] to the data. In the figure, the amplitude of the LPS-treated animal has been scaled to give equal amplitude as the control at 200 ms delay time.

LUND UNIVERSITY

ISBN 91-628-5434-8
Report 1/02
ISSN 0346-6221
ISRN LUTEDX/TEEM--1074--SE